JCB Journal of Cell Biology

ARTICLE

PISD acts as a switch between lipophagy and fatty acid transfer to mitochondria

Hanbing Xue[1*], Xingwen Hu[1*], Zhenni Yang[2,3*], Yiqing Cao[1], Qi Zhu[1], Hongyu Zhao[4], Xiaoli Ma[4], Tianxin Lei[1], Dian Zhuang[1], Jing Zheng[5,6,7], Siqi Guo[1], Xiaochuan Fu[8], Ka Kit Chung[9], Pingsheng Liu[8], Xiaohong Zhuang[9], Zhengyu Liang[1], Sicong He[1], Hui Jiang[5,6,7], and Yan G. Zhao[1]

Fatty acids (FAs) are transported from lipid droplets (LDs) to mitochondria for β-oxidation during cell starvation. Starvation also triggers engulfment of LDs by autophagosomes and their subsequent degradation by lysosomes (lipophagy). The mechanisms coordinating these pathways remain unclear. Here, we demonstrate that PISD-LD, an LD-localized isoform of phosphatidylserine decarboxylase, facilitates FA transfer while inhibiting lipophagy. PISD-LD mediates LD–mitochondrion (LD-mito) contacts via interaction with mitochondrial PISD. In *PISD-LD* KD cells, LDs are larger, and FA trafficking and mitochondrial FA β-oxidation are suppressed. The lipid transfer proteins ATG2A/B are recruited by PISDs to mediate FA transfer from LDs to mitochondria. Disruption of PISD-LD–mediated LD-mito contacts activates lipophagy, aiding LD degradation. PISD-LD binds the lipophagy receptor Spartin and inhibits lipophagy by impeding Spartin-LC3 interaction. PISD-LD also regulates LD-mito contacts and lipid metabolism in mouse liver. Thus, PISD-LD serves as a switch between LD-to-mitochondrion FA transfer and lipophagy, ensuring efficient energy production.

Introduction

Lipids are a diverse group of biomolecules that play essential roles in cellular structure, energy storage, and signaling. Intracellular lipid metabolism, which affects the synthesis, storage, mobilization, and utilization of lipids, plays a fundamental role in maintaining cellular homeostasis, providing energy substrates, and regulating various physiological processes. Dysregulation of lipid metabolism is associated with a variety of metabolic disorders, including obesity, diabetes, and cardiovascular diseases (Dakal et al., 2025; Yoon et al., 2021).

Lipid droplets (LDs) and mitochondria are essential organelles involved in the proper regulation of cellular lipid metabolism for maintenance of cellular energy homeostasis and health. LDs are evolutionarily conserved intracellular lipid storage compartments, consisting of a hydrophobic neutral lipid core surrounded by a phospholipid monolayer embedded with proteins (Farese and Walther, 2023; Gao et al., 2019; Olzmann and Carvalho, 2019; Yang et al., 2012; Zadoorian et al., 2023). Mitochondria are the primary sites for conversion of fatty acids (FAs) into energy via β-oxidation (Cui and Liu, 2020). LDs and mitochondria communicate with each other through formation of direct membrane contact sites (MCSs), i.e., LD–mitochondrion contacts (Cui and Liu, 2020). In response to a crisis such as starvation, cells shift their metabolism from glycolysis to FA oxidation. Triacylglycerol (TAG) in LDs is broken down, and FAs are transported to mitochondria for energy generation (Nguyen et al., 2017; Rambold et al., 2015; Wang et al., 2021). Although several proteins, including PLIN5 (Wang et al., 2011), MFN2 (Boutant et al., 2017), MIGA2 (Freyre et al., 2019), and VPS13D (Wang et al., 2021), were recently reported to participate in the formation of LD–mitochondrion (LD-mito) contacts, many fundamental questions remain as to how LD-mito interfaces are generated and how they conduct their particular functions.

Lipophagy serves as a critical mechanism for mobilizing stored lipids and generating energy substrates during periods of starvation or metabolic stress (Singh and Cuervo, 2012; Singh et al., 2009; Zechner et al., 2017). During lipophagy, LDs are

[1]School of Life Sciences, Southern University of Science and Technology, Shenzhen, P.R. China; [2]State Key Laboratory of Conservation and Utilization of Bio-resources in Yunnan and Center for Life Sciences, School of Life Sciences, Yunnan University, Kunming, P.R. China; [3]Southwest United Graduate School, Kunming, P.R. China; [4]National Laboratory of Biomacromolecules, CAS Center for Excellence in Biomacromolecules, Institute of Biophysics, Chinese Academy of Sciences, Beijing, P.R. China; [5]Tsinghua Institute of Multidisciplinary Biomedical Research, Tsinghua University, Beijing, P.R. China; [6]National Institute of Biological Sciences, Beijing, P.R. China; [7]Beijing Key Laboratory of Cell Biology for Animal Aging, Beijing, P.R. China; [8]Institute of Biophysics, Chinese Academy of Sciences, Beijing, P.R. China; [9]Centre for Plant Vacuole Biology and Biotechnology, Centre for Cell & Developmental Biology and State Key Laboratory of Agrobiotechnology, School of Life Sciences, The Chinese University of Hong Kong, Hong Kong, P.R. China.

*H. Xue, X. Hu, and Z. Yang contributed equally to this paper. Correspondence to Yan G. Zhao: zhaoyan@sustech.edu.cn

Y.G. Zhao is a lead contact.

https://doi.org/10.1083/jcb.202605090

specifically engulfed by double-membraned autophagosomes, forming autophagic vesicles that subsequently fuse with lysosomes, leading to the degradation of LD components by lysosomal hydrolases. The Troyer syndrome protein Spartin was recently identified as a lipophagy adaptor. Spartin, which localizes on the surface of LDs, interacts with the key autophagy proteins LC3A/C to deliver LDs to lysosomes for triglyceride mobilization (Chung et al., 2023). The interplay between LD-to-mitochondrion FA transfer and lipophagy must be tightly regulated to ensure the efficient utilization of stored lipids and energy homeostasis. However, the underlying mechanisms governing the coordination of these two pathways remain elusive.

Phosphatidylserine decarboxylase (PISD) is a mitochondrion-localized essential enzyme (termed PISD-M), which generates phosphatidylethanolamine (PE) through the decarboxylation of phosphatidylserine (PS) (Vance, 2008). In humans, *PISD* mutations cause Liberfarb syndrome, a severe multisystem disorder affecting the brain, eyes, ears, bones, and connective tissue (Peter et al., 2019; Zhao et al., 2019). Besides the mitochondrion-localized PISD, a second isoform of PISD, generated by alternative splicing of *PISD* mRNA, was recently identified to target on the surface of LDs (termed PISD-LD); however, its function is unknown (Kumar et al., 2021). Here, we demonstrate the decarboxylase-independent function of PISD-LD in building LD contacts with mitochondria by forming a complex with PISD-M. LD-mito contacts mediated by PISDs facilitate transfer of FAs from LDs to mitochondria. PISDs further recruit the lipid transport proteins ATG2A and ATG2B to channel FAs from LDs to mitochondria. Meanwhile, PISD-LD suppresses lipophagy by competing with the key autophagy protein LC3 for interaction with the lipophagy receptor Spartin. In the absence of PISD-LD, LDs are enlarged and lipophagy is triggered to remove excessive lipids. PISD-LD also regulates LD-mito contacts and lipid metabolism in mouse liver. This study highlights a pivotal role of PISD-LD in regulating lipid metabolism by facilitating FA transfer to mitochondria and suppressing lipophagy.

Results

PISD-LD and PISD-M promote contacts between LDs and mitochondria

PISD-LD and PISD-M are encoded by alternative splice variants of *PISD* mRNA. They share 302 common amino acids (aa) encoded by exons 6–10 and possess unique N-terminal fragments of 73 aa for PISD-LD (encoded by exons 4–5) and 107 aa for PISD-M (encoded by exons 1–3) (Fig. 1 A) (Kumar et al., 2021). To study the function of PISD-LD, we generated C-terminal GFP-tagged PISD-LD (PISD-LD-GFP) and PISD-M (PISD-M-GFP) as previously described (Kumar et al., 2021), and transfected them into COS7 cells (Fig. 1 B). As reported earlier (Kumar et al., 2021), PISD-LD-GFP translocated from mitochondria to LDs upon exposure to the LD inducer oleic acid (OA), while PISD-M-GFP stayed on mitochondria (Fig. S1 A). We further generated Flag-knock-in (KI)-PISD-LD cells by KI of Flag at the 5′ end of the endogenous *PISD-LD* locus (Fig. S1, B and C). We confirmed the LD localization of endogenous PISD-LD in these cells using the LD flotation assay (Fig. S1 D). However, we failed to construct Flag-KI-PISD-M cells. Instead, we generated a stable cell line expressing low levels of PISD-LD-HA and PISD-M-Flag using piggyBac-mediated genomic integration at low copy numbers. This method has been widely used to generate reporters for studying membrane contact (Choi et al., 2026; Grimm et al., 2016). The cell line is hereafter referred to as "PISD-HA/Flag stable cells." The expression levels of PISD-LD and PISD-M were comparable with their endogenous levels, and they were targeted to LDs and mitochondria, respectively (Fig. S1, E–G). Interestingly, we observed an increased association (quantified as contact surface area) between mitochondria and LDs in OA-treated cells overexpressing either PISD-LD-GFP or PISD-M-GFP (Fig. 1, C and D; and Fig. S1, H and I). In control cells expressing the GFP vector, mitochondria exhibited a typical tubulated morphology and the LD-mito contact surface area was significantly lower (Fig. 1, C and D; and Fig. S1, H and I). To precisely evaluate LD-mito contacts throughout our study, we conducted 3D imaging of cells under various conditions and performed comprehensive 3D organelle interaction analysis. In the figures, we present images from a single focal plane, along with 3D projections covering the entire cells and contact surfaces between LDs and mitochondria. To validate these findings, we employed transmission electron microscopy (TEM), a widely acknowledged method considered the "gold-standard" method for directly visualizing organelle contacts, as it offers high-resolution insights into cellular structures and membrane interactions (Hacker et al., 2023; Lam et al., 2021). Compared with GFP-expressing cells, LD-mito contacts were significantly increased in cells expressing PISD-LD-GFP or PISD-M-GFP (Fig. 1, E and F). We further used focused ion beam scanning electron microscope (FIB-SEM) imaging of GFP- or PISD-LD-GFP–overexpressing cells. Focusing on the distribution of LDs and mitochondria in the FIB-SEM datasets, we found that compared with GFP-transfected cells, mitochondria were often in close proximity to LDs in PISD-LD-GFP–overexpressing cells (Fig. 1 G; and Videos 1 and 2). We further quantified the number and proportion of the LD-mito contacts in close proximity to the ER, and we found no significant difference between control cells and cells overexpressing PISD-LD or PISD-M. These observations suggest that PISD-LD and PISD-M do not mediate three-way ER-mito-LD contacts (Fig. S1 J).

Next, we employed RNA interference (RNAi) to selectively knock down either *PISD-LD* or *PISD-M*, and then, we examined the association between LDs and mitochondria. To enhance the visualization of LDs, we performed ferrocyanide-reduced osmium tetroxide postfixation, thiocarbohydrazide-osmium liganding (OTO) staining in the subsequent TEM experiments. The ultrastructural images confirmed that LD-mito contacts were detected in control cells, while *siPISD-LD* or *siPISD-M* significantly reduced the number and extent of LD-mito interactions (Fig. 1, H and I). The effectiveness and selectivity of siRNAs targeting each transcript variant were validated through quantitative real-time (RT)-PCR analysis (Fig. S1 K). Together, these observations suggest that PISD-LD and PISD-M are critical for mitochondrial association with LDs.

As PISD is responsible for converting PS to PE by its decarboxylase activity (Vance, 2008), we next examined whether the

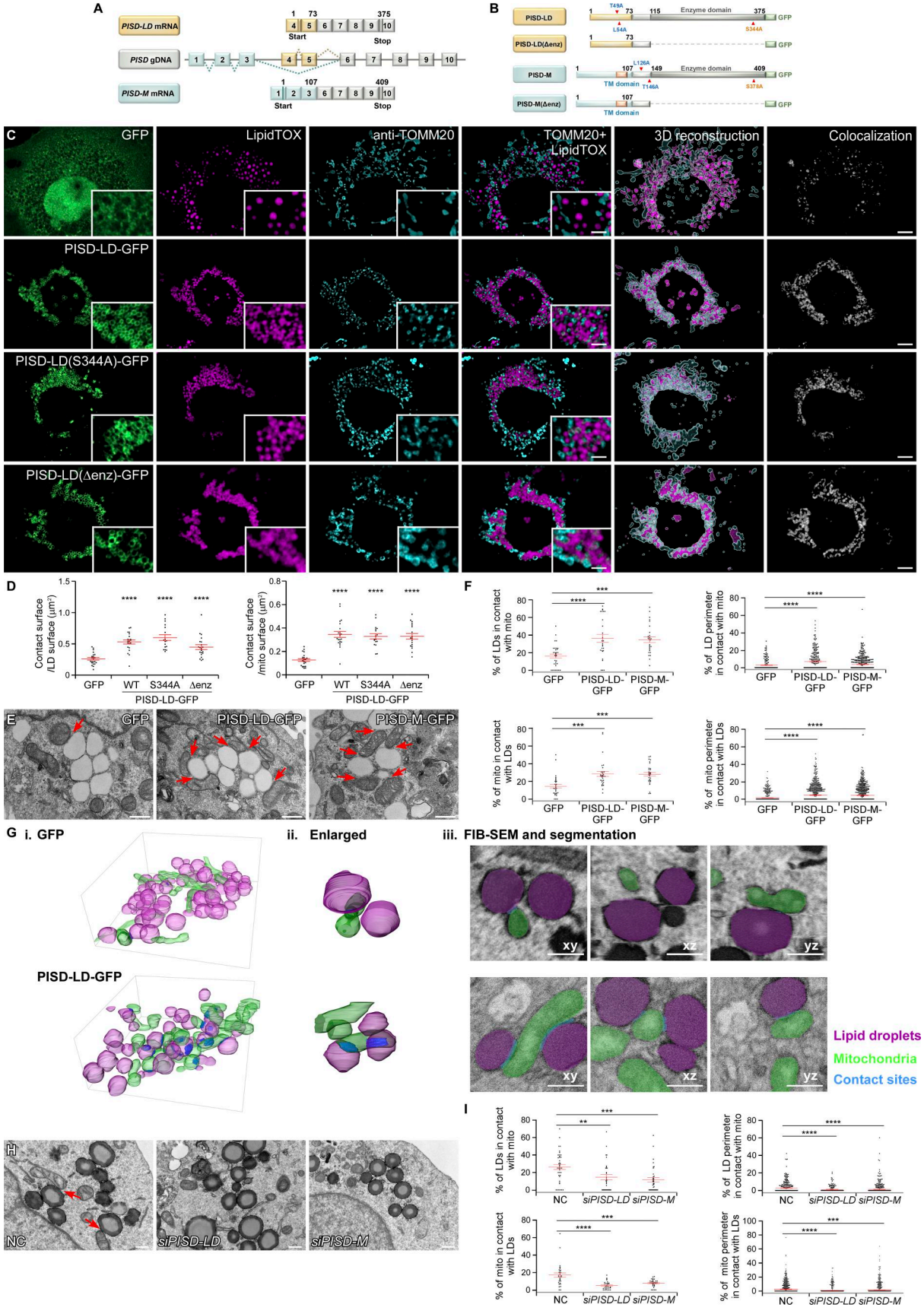

Figure 1. **PISD-LD and PISD-M facilitate contacts between LDs and mitochondria. (A)** Schematic shows the exon organization of the *PISD* gene (gDNA) and the *PISD-LD* and *PISD-M* splice variants. Both *PISD-LD* and *PISD-M* contain exons 6–10 (gray), while exons 4–5 (yellow) are specific to *PISD-LD* and exons 1–3

(blue) are specific to *PISD-M*. The numbers above the exons indicate the lengths (in aa) of the specific domains and the common domains in each isoform. **(B)** Schematic illustrates the generation of PISD-LD and PISD-M plasmids with mutations at the key serine residue in the LGST motif (yellow), mutations at the potential binding sites (blue), and deletion of the entire enzyme domain (Δenz). **(C and D)** Single focal plane images of OA-treated COS7 cells overexpressing GFP, PISD-LD-GFP, PISD-LD(S344A)-GFP, or PISD-LD(Δenz)-GFP (green) and stained with LipidTOX (LDs; magenta) and anti-TOMM20 antibody (mitochondria; cyan) (C). Additionally, 3D reconstructions and contact surfaces of the LipidTOX and TOMM20 channels (white) are shown (C). The left graph shows contact surface areas, normalized by LD surface areas. Each point represents an individual cell. Data are shown as the mean ± SEM (GFP, *n* = 22; PISD-LD-GFP, *n* = 21; PISD-LD(S344A)-GFP, *n* = 17; PISD-LD(Δenz)-GFP, *n* = 21). The right graph shows contact surface areas, normalized by mitochondrial surface areas. Each point represents an individual cell. Data are shown as the mean ± SEM (GFP, *n* = 22; PISD-LD-GFP, *n* = 21; PISD-LD(S344A)-GFP, *n* = 17; PISD-LD(Δenz)-GFP, *n* = 18) (D). Compared with GFP-expressing cells: ****P < 0.0001. Bars: 5 µm; insets, 2 µm. **(E and F)** TEM images of LD-mito contacts (red arrows) in COS7 cells overexpressing GFP, PISD-LD-GFP, or PISD-M-GFP under OA treatment (E). Top graphs: percentage of LDs in contact with mitochondria per cell (left) and percentage of LD perimeter in contact with mitochondria per LD (right). Data are shown as the mean ± SEM (GFP, *n* = 490 LDs from 34 cells; PISD-LD-GFP, *n* = 245 LDs from 27 cells; PISD-M-GFP, *n* = 466 LDs from 28 cells). Bottom graphs: percentage of mitochondria in contact with LDs per cell (left) and percentage of mitochondrial perimeter in contact with LDs per mitochondrion (right). Data are shown as the mean ± SEM (GFP, *n* = 678 mitochondria from 30 cells; PISD-LD-GFP, *n* = 978 mitochondria from 30 cells; PISD-M-GFP, *n* = 925 mitochondria from 30 cells) (F). ***P < 0.001; ****P < 0.0001. Bars: 500 nm. **(G)** (i) 3D rendering of segmented LDs (magenta), mitochondria (green), and contact sites (blue) from a FIB-SEM volume in GFP- and PISD-LD-GFP–overexpressing COS7 cells. Volume size, 6 × 6 × 2.5 µm. (ii) 3D rendering of segmented LDs (magenta), mitochondria (green), and contact sites (blue) from a FIB-SEM volume in GFP- and PISD-LD-GFP-overexpressing COS7 cells. Volume size, 1.5 × 1.5 × 1.5 µm. (iii) FIB-SEM images and segmentation of LDs (magenta), mitochondria (green), and contact sites (blue) of (ii). The left panel shows the XY section, the middle panel shows the XZ section, and the right panel shows the YZ section. Scale bar: 500 nm. **(H and I)** TEM images with OTO staining of LD-mito contacts (red arrows) in OA-treated COS7 cells with KD of *PISD-LD* or *PISD-M* (H). Top graphs: percentage of LDs in contact with mitochondria per cell (left) and percentage of LD perimeter in contact with mitochondria per LD (right). Data are shown as the mean ± SEM (NC, *n* = 347 LDs from 39 cells; *siPISD-LD*, *n* = 286 LDs from 33 cells; *siPISD-M*, *n* = 619 LDs from 36 cells). Bottom graphs: percentage of mitochondria in contact with LDs per cell (left) and percentage of mitochondrial perimeter in contact with LDs per mitochondrion (right). Data are shown as the mean ± SEM (NC, *n* = 894 mitochondria from 30 cells; *siPISD-LD*, *n* = 1085 mitochondria from 30 cells; *siPISD-M*, *n* = 1115 mitochondria from 30 cells) (I). NC, negative control siRNA. **P < 0.01; ***P < 0.001; ****P < 0.0001. Bars: 500 nm.

enzymatic activity of PISD-M and/or PISD-LD plays a role in regulating LD-mito contacts. The enzyme activity of PISD is dependent on autocatalytic cleavage at a conserved LGST motif (Horvath et al., 2012; Onguka et al., 2015). We generated PISD-LD and PISD-M with mutations at the key serine residue in the LGST motif (PISD-LD(S344A) and PISD-M(S378A), respectively) or with deletion of the entire enzyme domain (Δenz) (Fig. 1 B). After transfecting cells with wild-type (WT) or mutant PISD-LD or PISD-M, we observed that all of them induced similar levels of LD-mito contacts (Fig. 1, C and D; and Fig. S1, H and I). Notably, the enhanced contacts induced by the overexpression of PISD-LD or PISD-M were not attributed to increased PE production by PISDs, as treatment of cells with the PE precursor lyso-PE, which elevates cellular PE levels, did not lead to more LD-mito interactions (Fig. S1 L). Our data suggest that facilitation of LD-mito contacts by PISD-LD and PISD-M might operate independently of their decarboxylase activity.

Heterotypic interaction between PISD-LD and PISD-M is responsible for tethering LDs with mitochondria

The respective targeting of PISD-LD and PISD-M to LDs and mitochondria prompted us to speculate whether these two proteins act directly as tethers to mediate the contacts between the two organelles. GFP-Trap assays showed that Myc-PISD-M was efficiently pulled down by PISD-LD-GFP (Fig. 2 A), and Myc-PISD-LD was pulled down by PISD-M-GFP (Fig. S1 M). Furthermore, upon LD induction by OA treatment, the interaction between PISD-LD and PISD-M was greatly elevated (Fig. 2 A and Fig. S1 M), and further increased after starvation (Fig. 2 A). Similar results were found using PISD-HA/Flag stable cells (Fig. 2 B). LD-mito contacts induced by PISD-LD overexpression were reduced in *siPISD-M* cells (Fig. 2, C and D), while knockdown (KD) of *PISD-LD* also suppressed LD-mito interactions induced by overexpressed PISD-M (Fig. S1, N and O). This evidence suggests that heterotypic PISD-M and PISD-LD interaction tethers LDs and mitochondria.

Using AlphaFold 2.0 prediction, we identified two potential binding sites between PISD-LD and PISD-M, i.e., L54 in PISD-LD with T146 in PISD-M and T49 in PISD-LD with L126 in PISD-M (Fig. 2 E). We generated single or double mutations in PISD-LD and PISD-M to examine the contribution of these sites to the interactions of the two proteins (Fig. 1 B). The results demonstrated that disrupting either interaction site reduced the binding of PISD-LD and PISD-M, while mutating both sites greatly reduced their interaction, compared with WT PISD-LD and PISD-M (Fig. 2 F and Fig. S1 P). We then transfected cells with double-mutant PISD-LD and double-mutant PISD-M and found that LD-mito contacts were significantly reduced compared to cells transfected with WT PISD-LD and PISD-M (Fig. 2, G and H). The mutations did not disrupt the localization of PISD-LD or PISD-M (Fig. 2 G).

To verify the role of PISD-LD and PISD-M as tethers, we used the split-Fluorescence-Activating and Absorption-Shifting Tag (FAST) assay, which enables observation of protein interactions (Tebo and Gautier, 2019). In this assay, the two halves of the FAST, NFAST and CFAST, are fused to proteins of interest. If the proteins interact in cells, the FAST is reconstituted, and it binds and enhances the fluorescence of 4-hydroxy-3-methylbenzylidene rhodanine (HMBR) in a reversible manner. We fused NFAST and CFAST to PISD-LD and PISD-M, respectively. After transfection into cells, HMBR fluorescence, generated by interaction between PISD-LD-NFAST and PISD-M-CFAST, was present at LD-mito contact sites, while no signals were detected in control cells expressing PISD-LD-NFAST with empty CFAST or PISD-M-CFAST with empty NFAST (Fig. S1 Q). Next, we specifically investigated the role of aa 115–148 of PISD-M, which contain the PISD-LD–interacting residues (L126 and T146). We designated this region of PISD-M as the PISD-LD–binding

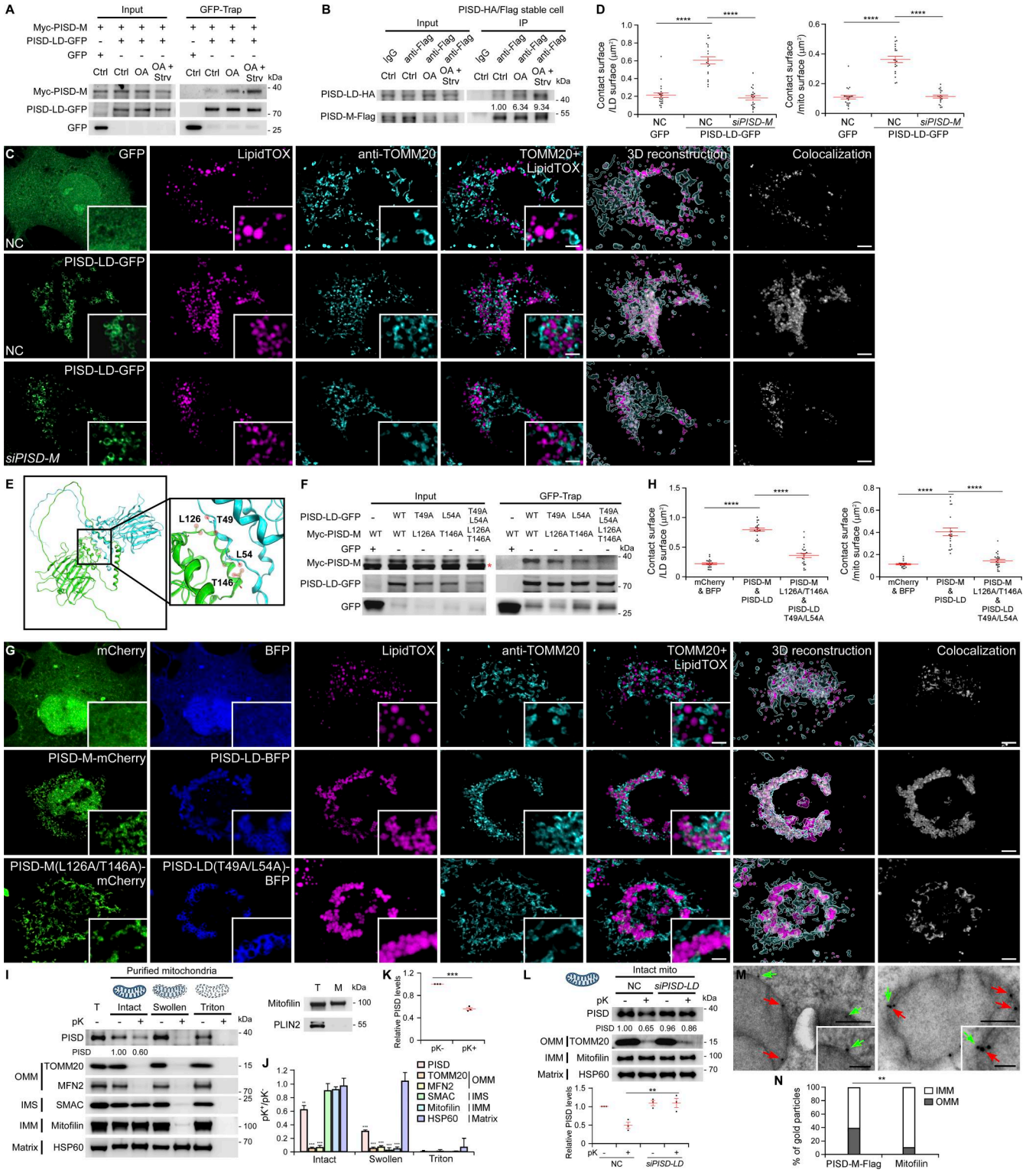

Figure 2. **Interaction between PISD-LD and PISD-M mediates LD-mito contacts. (A)** In a GFP-Trap assay, Myc-PISD-M is immunoprecipitated by PISD-LD-GFP. The amount of the immunoprecipitated protein is increased upon OA treatment and is further enhanced under starvation conditions. **(B)** Co-IP analysis of the interaction between PISD-LD-HA and PISD-M-Flag in PISD-HA/Flag stable cells. Immunoprecipitation was performed using a specific antibody against HA or a control IgG. The amount of immunoprecipitated protein is increased upon OA treatment and is further enhanced under starvation conditions. Quantifications of PISD-LD-HA levels (normalized by PISD-Mito-Flag levels) are shown. **(C and D)** Single focal plane images of OA-stimulated NC or *siPISD-M* COS7 cells overexpressing PISD-LD-GFP (green) and stained with LipidTOX (LDs; magenta) and anti-TOMM20 antibody (mitochondria; cyan) (C). Additionally, 3D reconstructions and contact surfaces of the LipidTOX and TOMM20 channels (white) are shown (C). The left graph shows contact surface areas, normalized by LD surface areas. Each point represents an individual cell. Data are shown as the mean ± SEM (NC & GFP, $n = 24$; NC & PISD-LD-GFP, $n = 20$; *siPISD-M* & PISD-LD-GFP, $n = 20$). The right graph shows contact surface areas, normalized by mitochondrial surface areas. Each point represents an individual cell. Data are shown

as the mean ± SEM (NC & GFP, *n* = 23; NC & PISD-LD-GFP, *n* = 20; *siPISD-M* & PISD-LD-GFP, *n* = 20) (D). NC, negative control siRNA. ****P < 0.0001. Bars: 5 µm; insets, 2 µm. **(E)** AlphaFold prediction on full-length PISD-LD (cyan) and PISD-M (green) shows that T49 in PISD-LD interacts with L126 in PISD-M, while L54 in PISD-LD interacts with T146 in PISD-M. **(F)** In a GFP-Trap assay, the interaction between PISD-LD and PISD-M is reduced by single mutations and is dramatically inhibited by double mutations of the residues in E. The asterisk indicates nonspecific bands. WT, wild type. **(G and H)** Single focal plane images of OA-treated COS7 cells transfected with mCherry (green) & BFP, WT PISD-M-mCherry (green) & PISD-LD-BFP, or PISD-M(L126A/T146A)-mCherry (green) & PISD-LD(T49A/L54A)-BFP (blue) and stained with LipidTOX (LDs; magenta) and anti-TOMM20 antibody (mitochondria; cyan) (G). Additionally, 3D reconstructions and colocalization surfaces of the LipidTOX and TOMM20 channels (white) are shown (G). Graphs show contact surface areas, normalized by LD and mitochondrial surface areas. Each point represents an individual cell. Data are shown as the mean ± SEM (mCherry & BFP, *n* = 22; PISD-M-mCherry & PISD-LD-BFP, *n* = 20; PISD-M [L126A/T146A]-mCherry & PISD-LD [T49A/L54A]-BFP, *n* = 23) (H). ****P < 0.0001. Bars: 5 µm; insets, 2 µm. **(I–K)** Determination of the submitochondrial localization of PISD-M. Purified mitochondria from COS7 cells were either left intact, treated with hypotonic swelling buffer, or lysed with Triton buffer. All samples were then digested with pK to analyze the localization of PISD-M. TOMM20 and MFN2 represent OMM proteins; SMAC is an IMS protein; Mitofilin is an IMM protein, facing the IMS side; and HSP60 is a matrix protein (I). Immunoblotting shows the levels of Mitofilin and PLIN2 in total lysates and isolated mitochondria. T, total lysate; M, isolated mitochondria. Blots were probed with anti-Mitofilin and anti-PLIN2 antibodies (I). Quantification of the ratios of protein levels with and without pK treatment is shown as the mean ± SEM (*n* = 3) (J). Relative PISD levels, normalized to Mitofilin levels, are shown from intact mitochondria with or without pK treatment (K). Compared with pK (−) samples: **P < 0.01; ***P < 0.001. **(L)** Determination of the submitochondrial localization of PISD-M in NC or *siPISD-LD* COS7 cells. Purified intact mitochondria were digested with pK to analyze the localization of PISD-M. TOMM20 is an OMM protein; Mitofilin is an IMM protein, facing the IMS side; and HSP60 is a matrix protein. Relative PISD levels, normalized to Mitofilin levels, are shown from intact mitochondria with or without pK treatment. **P < 0.01. **(M and N)** Immuno-EM images show that PISD-M-Flag signals are detected on both OMM and IMM. PISD-HA/Flag stable cells were subjected to HPF fixation. Sections were immunolabeled with anti-Flag and anti-Mitofilin antibodies, followed by gold particle labeling. Green arrows indicate Flag signals (6 nm), while red arrows indicate Mitofilin signals (15 nm) (M). The percentage of OMM-localized Flag signals is significantly higher than the percentage of OMM-localized Mitofilin signals (PISD-M-Flag, *n* = 180 gold particles; Mitofilin, *n* = 277 gold particles) (N). **P < 0.01. Bars: 200 nm; insets: 50 nm. Immuno-EM, immuno-electron microscopy; HPF, high-pressure freezing. Source data are available for this figure: SourceData F2.

domain (PBD). To further validate the direct involvement of this region in mediating LD-mito contacts, we engineered a fusion protein in which the PBD of PISD-M was joined with the peroxisome transmembrane (TM) protein PEX3 (PEX3-PBD-GFP), thus positioning it on the peroxisome surface. BFP-SKL was used as a marker for peroxisomes (Kim et al., 2006; Valm et al., 2017). Compared with PEX3-GFP, the overexpression of PEX3-PBD-GFP promoted peroxisome–LD interactions, and the interactions were disrupted by *siPISD-LD* (Fig. S1 R). These findings provide further evidence that the interaction between PISD-LD and PISD-M is important for mediating LD-mito contacts.

Partial localization of PISD-M on outer mitochondrial membranes

As mentioned above, in order to form MCSs, protein tethers should be located on the outer surface of the opposing organelles. However, previous studies demonstrated that the PS decarboxylase activity was detected on the biochemically isolated inner mitochondrial membrane (IMM) (Percy et al., 1983; Zborowski et al., 1983), suggesting an internal localization of PISD-M. To directly investigate the distribution of PISD-M on mitochondria, we used multimodality structured illumination microscopy (multi-SIM) to perform super-resolution imaging of cells co-expressing PISD-M-GFP and the outer mitochondrial membrane (OMM) marker TOMM20-mCherry, with the intermembrane space (IMS) marker LACTB(1–68)-mCherry (Brown et al., 2011; Polianskyte et al., 2009), the IMM marker CYC1-mCherry, or the matrix protein marker HSP60-mCherry. We observed clear separation of OMM markers from IMM, IMS, or matrix markers, as well as obvious colocalization of PISD-M with the OMM marker TOMM20 (Fig. S2 A). This suggests that a subpopulation of PISD-M is localized on the OMM.

To study the topology of PISD-M on mitochondrial membranes, we utilized a fluorescent protease protection (FPP) assay. Cells were subjected to plasma membrane permeabilization by digitonin, followed by proteinase K (pK) treatment, which specifically cleaves the cytoplasmic fragments of proteins on organelle membranes, leaving the luminal fragments/proteins intact (Fig. S2 B). The PISD-LD-GFP signal immediately disappeared when the digitonin-permeabilized cells were treated with pK (Fig. S2, C and D), due to the location of PISD-LD on the LD surface. We then performed the assay with cells simultaneously transfected with C-terminal-tagged PISD-M-GFP and TOMM20-mCherry, LACTB(1–68)-mCherry, CYC1-mCherry, or HSP60-mCherry as markers for OMM, IMS, IMM, or matrix, respectively. Upon pK treatment, the fluorescence intensity of PISD-M and TOMM20 quickly decreased, while the signals of LACTB (1–68), CYC1, and HSP60 were stable (Fig. S2, E-L). Interestingly, we did observe that residual PISD-M signal remained undigested while TOMM20 was fully digested (Fig. S2, E and F). This indicates that a portion of PISD-M is inside mitochondria, consistent with the previously reported decarboxylase activity of PISD on the IMM (Percy et al., 1983; Zborowski et al., 1983). Altogether, these data verify the cytosol-facing localization of a portion of PISD-M. When GFP was added to the N terminus of PISD-M, it disrupted the mitochondrial targeting of PISD-M (Fig. S2 M). As an alternative, we inserted GFP immediately ahead of the TM domain of PISD-M (GFP-TM-PISD-M). This protein showed mitochondrial localization and induced LD-mito contacts similar to PISD-M-GFP (Fig. S2, N and O). FPP assays demonstrated that the fluorescence of GFP-TM-PISD-M persisted with pK treatment (Fig. S2, P and Q).

To further investigate the submitochondrial localization of PISD-M, we performed pK digestion on purified mitochondria and detected endogenous mitochondrial proteins with antibodies. As OA treatment causes the translocation of PISD-LD to LDs, we utilized OA-treated cells for purification of mitochondria to eliminate mitochondrial PISD-LD (Fig. 2 I). When intact mitochondria are exposed to pK, only outer membrane proteins, such as TOMM20, are degraded. Mitochondrial swelling with a

hypotonic buffer disrupts the outer membrane while keeping the inner membrane intact, allowing the protease to cleave TOMM20 (OMM), SMAC (IMS), and Mitofilin (IMM). Lysis of mitochondria with Triton buffer disrupts both the outer and inner membranes, enabling the protease to cleave proteins in all mitochondrial compartments, including the matrix protein HSP60 (Fig. 2 I) (Cao et al., 2023). We found that around 40% of endogenous PISD detected with antibody was cleaved after pK treatment of intact mitochondria, and most of the PISD was digested in pK-treated swollen mitochondria (Fig. 2, I and J; and Fig. S2, R and S). The level of pK-sensitive mitochondrial PISD was reduced in *siPISD-LD* cells (Fig. 2 L), suggesting that PISD-LD may help to sequester PISD-M on the OMM. Immuno-electron microscopy demonstrated that in PISD-HA/Flag stable cells, PISD-M-Flag signals were detected on both OMM and IMM, and the percentage of PISD-M-Flag signals on the OMM was significantly higher than the percentage of Mitofilin signals on the OMM (Fig. 2, M and N; and Fig. S2 T). These data collectively indicate that a portion of PISD is localized on the OMM, and therefore, it can potentially function as a tether (Fig. S2 U).

PISD-LD regulates LD size independent of its enzymatic activity

LD-mito contacts were reported to have two opposing functions in lipid homeostasis: facilitating lipolysis through mitochondrial fatty acid oxidation (FAO), and promoting LD expansion by increasing ATP synthesis (Veliova et al., 2020). To explore the function of LD-mito contacts mediated by PISD-LD and PISD-M in lipid metabolism, we examined LD formation in cells with overexpression or depletion of PISD-LD or PISD-M. Compared with GFP-transfected cells, the overexpression of PISD-LD-GFP or PISD-M-GFP significantly suppressed the size and total volume of LDs, without affecting the ability of cells to take up FAs (Fig. 3, A and B; and Fig. S3 A). We performed 3D imaging of cells under different conditions to evaluate all the LDs. Images with 3D projections are presented to provide a comprehensive visualization of the LDs across the entire cells. Depleting *PISD-LD* resulted in significantly enlarged LDs and an increase in total LD volume (Fig. 3, C and D). To rule out the possibility that the enzyme activity of PISD-LD may play a role in regulating LD size, we first performed lipid profiling of LDs and mitochondria from NC and *siPISD-LD* cells. No obvious difference in lipid composition was detected between them (Fig. S3, B–D), suggesting that PISD enzyme activity may not be activated on LDs. Furthermore, we reintroduced RNAi-resistant WT PISD-LD (PISD-LD^{r}-GFP), enzyme-dead mutant PISD-LD (PISD-LD(S344A)^{r}-GFP), or decarboxylase domain-deleted PISD-LD (PISD-LD(Δenz)^{r}-GFP) into *PISD-LD* KD cells. All of these manipulations reversed the increased LD size so that the LDs were similar in size to those in GFP-transfected NC cells (Fig. 3, E and F; and Fig. S3, E-G). To confirm the function of PISD-LD–mediated LD-mito contacts in regulating LD size, we expressed the PISD-M binding–defective PISD-LD mutant (PISD-LD(T49A/L54A)^{r}-GFP) (Fig. 1 B). It failed to suppress the enlarged LDs in *siPISD-LD* cells (Fig. 3, E and F). Thus, PISD-LD is important for restraining LD size, and this property depends on its LD-mito–tethering function but not its decarboxylase activity.

In contrast to *siPISD-LD*, smaller LDs were formed in *siPISD-M* cells (Fig. 3, C and D). This discrepancy may be caused by decreased global PE levels as a result of PISD-M deficiency (St Germain et al., 2022). Cone-shaped PE molecules reduce the LD membrane surface tension and drive the formation of larger LDs (Ben M'barek et al., 2017). To avoid the global effects caused by the absence of PISD-M, we mainly focused on PISD-LD in the rest of the study.

PISD-LD is critical for FA trafficking from LDs to mitochondria and mitochondrial FA β-oxidation

Given that the disruption of PISD-mediated LD-mito contacts causes larger LDs, we inferred that the function of the contacts is for FA transfer from LDs to mitochondria. To test this hypothesis, we performed a FA tracking assay (Wang et al., 2021). Cells were preloaded with a fluorescence-labeled FA analog BODIPY-C12 (Red-C12), which initially accumulated in LDs. After 5-h starvation, Red-C12 signals in control cells showed colocalization with mitochondria, suggesting transfer of Red-C12 from LDs to mitochondria (Fig, 4, A-C; and Fig. S3 H). In *PISD-LD* KD cells, a large amount of Red-C12 remained in LDs instead of transferring to mitochondria, and this defect was rescued by re-expressing PISD-LD^{r}-BFP or PISD-LD(Δenz)^{r}-BFP (Fig. 4, B and C). The uptake of Red-C12 was comparable between NC and *siPISD-LD* cells (Fig. S3, I and J). The defect in LD-to-mitochondrion FA transfer in *PISD-LD*–deficient cells was not due to enhanced FA esterification or decreased TAG hydrolysis (Fig. S3, K and L). Similarly, *siPISD-LD* also dampened starvation-induced transfer of preloaded BODIPY-palmitate (C14) from LDs to mitochondria (Fig. S3, M and N). These data suggest that PISD-LD plays a critical role in efficient FA transfer from LDs to mitochondria, independent of its enzymatic function.

Impairment of LD-to-mitochondrion transfer of FAs may lead to inefficient mitochondrial FA β-oxidation (Chen et al., 2025; Talari et al., 2023; Wang et al., 2011). Seahorse FAO assays were applied to assess the role of PISD-LD in mitochondrial oxidation of endogenous FAs. After LD induction with OA treatment, *PISD-LD* KD cells in substrate-limited medium displayed obvious reductions of mitochondrial basal, ATP-linked, and maximal respiration, which were rescued by re-expressing PISD-LD^{r}-GFP or PISD-LD(Δenz)^{r}-GFP (Fig. 4 D). This suggests that PISD-LD regulates FA transfer, independent of its enzymatic function. Taken together, these data suggest that PISD-LD mediates FA transportation from LDs to mitochondria to fuel mitochondrial FAO.

To rule out the possibility that depletion of PISD-LD directly damages mitochondria, we investigated the morphology and dynamics of mitochondria in *siPISD-LD* cells. Immunostaining with TOMM20 antibody and imaging by TEM revealed no obvious fragmented or swollen mitochondria in *PISD-LD* KD cells (Fig. S3, O and P). Furthermore, we used mitochondrial matrix–targeted photoactivatable GFP (mtPA-GFP) to detect mitochondrial dynamics. In this assay, mitochondrial fusion is reflected by the rate of spread of the GFP signal following photoactivation of PA-GFP in a subset of mitochondria (Molina and Shirihai, 2009). Time-lapse confocal imaging showed that the limited

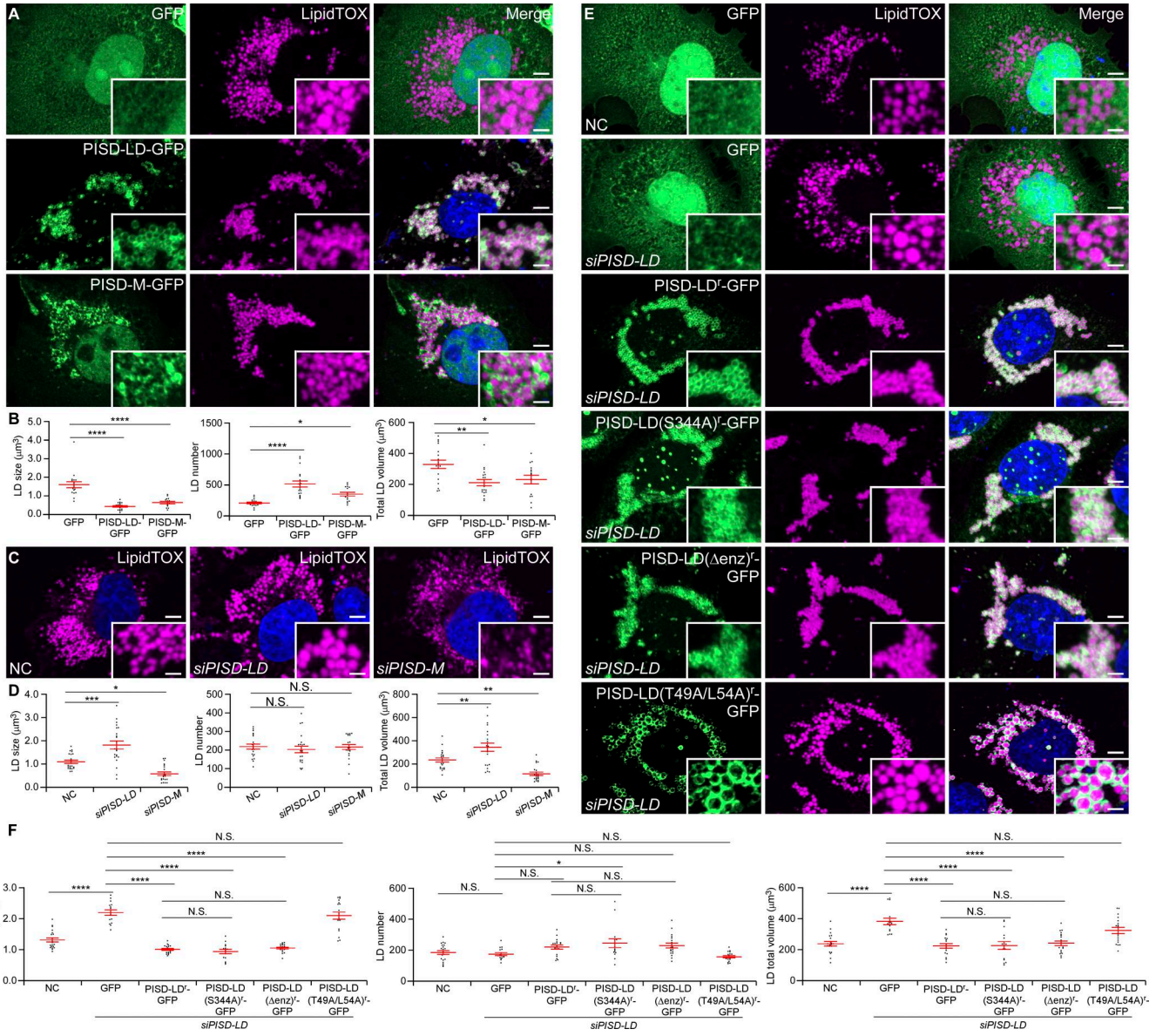

Figure 3. **Tether, but not enzyme, function of PISD-LD controls LD size. (A and B)** 3D projection images of OA-treated COS7 cells overexpressing GFP, PISD-LD-GFP, or PISD-M-GFP (green). LDs were stained with LipidTOX (magenta) (A). LD sizes, numbers, and total volumes per cell are shown as the mean ± SEM (GFP, *n* = 18; PISD-LD-GFP, *n* = 19; PISD-M-GFP, *n* = 15) (B). *P < 0.05; **P < 0.01; ****P < 0.0001. Bars: 5 µm; insets, 2 µm. **(C and D)** 3D projection images of NC, *siPISD-LD*, or *siPISD-M* COS7 cells stimulated with OA. LDs were stained with LipidTOX (magenta) (C). LD sizes, numbers, and total volumes per cell are shown as the mean ± SEM (NC, *n* = 21; *siPISD-LD*, *n* = 22; *siPISD-M*, *n* = 20) (D). NC, negative control siRNA. *P < 0.05; **P < 0.01; ***P < 0.001; N.S., not significant. Bars: 5 µm; insets, 2 µm. **(E and F)** 3D projection images of NC or *siPISD-LD* COS7 cells overexpressing GFP, RNAi-resistant PISD-LD-GFP, PISD-LD(S344A)-GFP, PISD-LD(Δenz)-GFP, or PISD-LD(T49A/L54A)-GFP (green) under OA treatment. LDs were stained with LipidTOX (magenta) (E). LD sizes, number, and total volumes are shown as the mean ± SEM (NC & GFP, *n* = 20 cells; *siPISD-LD* & GFP, *n* = 15; *siPISD-LD* & PISD-LDʳ-GFP, *n* = 18; *siPISD-LD* & PISD-LD(S344A)ʳ-GFP, *n* = 15; *siPISD-LD* & PISD-LD(Δenz)ʳ-GFP, *n* = 19; *siPISD-LD* & PISD-LD(T49A/L54A)ʳ-GFP, *n* = 18) (F). NC, negative control siRNA. *P < 0.05; ****P < 0.0001; N.S., not significant. Bars: 5 µm; insets, 2 µm.

photoactivated mitochondrial signal expanded even faster in *PISD-LD* KD cells than in control cells (Fig. S3, Q and R), suggesting that mitochondrial dynamics were enhanced by *PISD-LD* KD. These findings imply that the defective mitochondrial FAO observed in *siPISD-LD* cells may not be due to structural or dynamic mitochondrial deficiencies.

Adipose triglyceride lipase (ATGL) was shown to liberate FA from LDs and facilitate the transfer of FA from LDs to mitochondria (Ouyang et al., 2023). We examined the physical and functional interactions between ATGL and PISDs. In GFP-Trap assays, we observed an interaction between ATGL and PISD-LD, but not PISD-M (Fig. S3, S and T). This aligns with the known LD localization of ATGL (Ouyang et al., 2023). We also treated cells with the ATGL inhibitor Atglistatin (ATGLi). ATGLi suppressed the smaller LDs induced by overexpression of PISD-LD (Fig. S3, U and V), which implies that ATGL may be recruited by PISD-LD to facilitate the release of FAs from LDs.

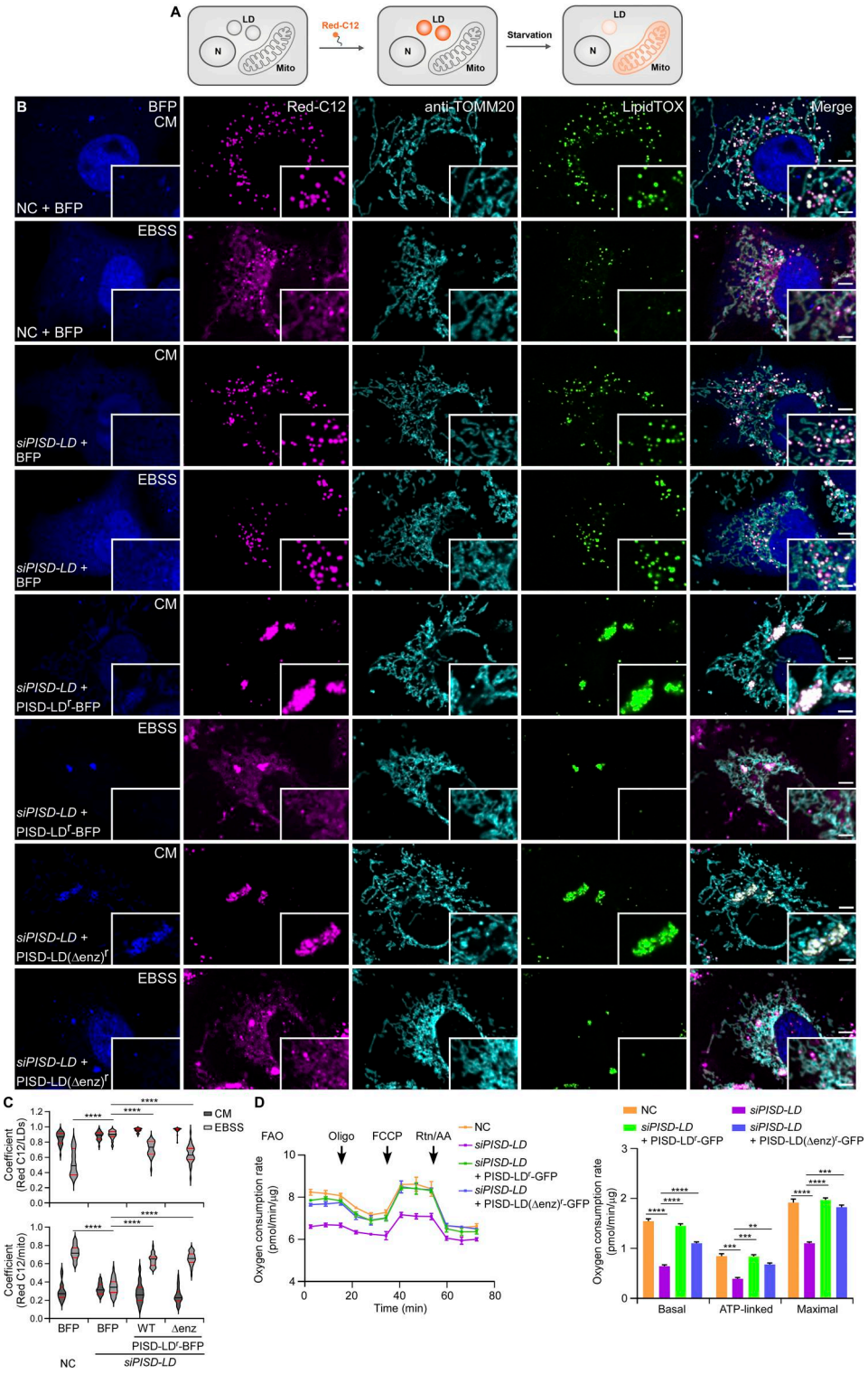

Figure 4. **PISD-LD is required for transfer of FA from LDs to mitochondria for FAO. (A)** Schematic illustration of the FA transfer assay. N, nucleus; LD, lipid droplet; Mito, mitochondrion. **(B and C)** Confocal images of NC and *siPISD-LD* COS7 cells overexpressing BFP, RNAi-resistant PISD-LD-BFP, or PISD-LD(Δenz)-BFP (blue) loaded with Red-C12 (magenta) and stained with LipidTOX (LDs; green) and anti-TOMM20 antibody (mitochondria; cyan) under fed (CM) or starvation (EBSS) conditions (B). Overlap coefficients of Red-C12 with LDs or mitochondria are shown as violin plots with the black line indicating the median and the red lines indicating the interquartile range (NC & BFP in CM, $n = 32$; NC & BFP in EBSS, $n = 27$; *siPISD-LD* & BFP in CM, $n = 31$; *siPISD-LD* & BFP in EBSS, $n = 32$; *siPISD-LD* & PISD-LD^r-BFP in CM, $n = 31$; *siPISD-LD* & PISD-LD^r-BFP in EBSS, $n = 31$; *siPISD-LD* & PISD-LD(Δenz)^r-BFP in CM, $n = 32$; *siPISD-LD* & PISD-LD(Δenz)^r-BFP in EBSS, $n = 33$) (C). NC, negative control siRNA; CM, complete medium. ****P < 0.0001. Bars: 5 µm; insets, 2 µm. **(D)** Seahorse FAO assays show oxidation of endogenous FAs in NC cells (orange), *siPISD-LD* cells (magenta), *siPISD-LD* cells with PISD-LD^r-GFP (green), and *siPISD-LD* cells with PISD-LD(Δenz)^r-GFP (blue). Quantitative data of basal OCR, ATP-linked OCR, and maximal OCR in mitochondria are shown as means ± SEM ($n = 3$). NC, negative control siRNA; Oligo, oligomycin; FCCP, carbonyl cyanide-p-trifluoromethoxyphenylhydrazone; Rtn, rotenone; AA, antimycin A. **P < 0.01; ***P < 0.001; ****P < 0.0001.

PISDs recruit ATG2A/B to facilitate FA transport

Since PISDs contain no lipid transfer domain (LTD), lipid transfer proteins (LTPs) would be required for PISD-mediated delivery of lipids from LDs to mitochondria. ATG2A and ATG2B contain an LTD and have been reported to transport lipids between membranes (Maeda et al., 2019; Osawa et al., 2019; Osawa et al., 2020; Valverde et al., 2019). ATG2A and ATG2B show redundant functions with each other, and depletion of both proteins causes enlarged LDs (Velikkakath et al., 2012), which is similar to the phenotype of *PISD-LD* KD cells. To investigate whether ATG2s are involved in PISD-mediated LD-mito contacts, we first examined the interactions between these proteins. In GFP-Trap assays, endogenous ATG2A and ATG2B were pulled down by PISD-LD-GFP and PISD-M-GFP (Fig. 5, A and B). Moreover, their interaction was enhanced with OA treatment (Fig. 5, A and B). Similarly, in PISD-HA/Flag stable cells, endogenous ATG2A was immunoprecipitated by PISD-LD-HA or PISD-M-Flag, and this interaction was enhanced by the addition of OA (Fig. 5, C and D). Endogenous PISD was also immunoprecipitated by GFP-ATG2A and ATG2B-GFP (Fig. S4 A). Other LD proteins, including PLIN2 and PLIN3, failed to pull down ATG2A and ATG2B (Fig. S4 B), indicating the specificity of the interaction between PISD-LD and ATG2s.

We then examined whether ATG2s are required for LD-to-mitochondrion FA trafficking. In cells with simultaneous KD of *ATG2A* and *ATG2B* (*ATG2A/B* KD), FA transfer assays showed that Red-C12 signals were trapped in LDs (Fig. 5, E and F; and Fig. S4 C), while LD-mito contacts were not affected (Fig. S4, D and E). These observations suggest that deficiency of ATG2s prevents FA transport from LDs to mitochondria. Accordingly, in Seahorse FAO assays, the basal, ATP-linked, and maximum respiration levels were dramatically reduced in *ATG2A/B* KD cells (Fig. 5 G). Furthermore, overexpressing ATG2A, but not the LTD-deficient ATG2A (ATG2A(ΔLTD)) (Valverde et al., 2019), led to smaller LDs, which suggests a role of ATG2 in controlling LD size through its LTD domain (Fig. S4, F and G). To further explore the role of ATG2s in PISD-mediated LD-mito contacts, we knocked down *ATG2A/B* in PISD-LD–overexpressing cells. The results demonstrated that PISD-LD overexpression failed to induce smaller LDs in *ATG2A/B*-deficient cells (Fig. 5, H and I). These results indicate that ATG2s are engaged to mediate FA transfer from LDs to mitochondria at PISD-induced LD-mito contact sites.

Blocking FA transfer through LD-mito contacts promotes lipophagy

While LD-mito contact–mediated FA transfer was blocked in *siPISD-LD* cells, the size of LDs was only modestly increased, which prompted us to consider that an alternative pathway was triggered to remove excess LDs. Lipophagy is an important pathway for LD degradation: LDs are selectively swallowed by autophagosomes for lysosomal degradation to maintain LD homeostasis (Zechner et al., 2017). We found that compared with control cells, levels of the LD surface proteins PLIN2 and PLIN3, but not the mitochondrial protein TOMM20, were significantly decreased in *PISD-LD* KD cells with OA treatment, and LC3-II/I ratios were elevated (Fig. 6, A and B). Meanwhile, proteomics analysis of LDs from NC and *siPISD-LD* cells revealed no obvious difference in protein composition (Fig. S4 H). These changes suggest that LD degradation by selective autophagy is promoted when PISD-LD is depleted. Moreover, the reduction of LD protein levels in *PISD-LD* KD cells was suppressed by chloroquine (CQ) treatment (Fig. 6, A and B), which blocks lysosomal degradation (Mauthe et al., 2018). Reintroduction of WT PISD-LD^{r}-GFP or PISD-LD(Δenz)^{r}-GFP suppressed the reduction of LD proteins in *PISD-LD* KD cells (Fig. 6, C and D). LD size in *siPISD-LD* cells was further increased when the key autophagy gene *ATG5* was knocked down (Fig. S4, I–K). These results suggest that PISD-LD negatively regulates lipophagy, in a manner independent of its enzyme domain.

To examine lipophagy flux, we constructed a dual-color reporter with mCherry and GFP fused in tandem to the LD protein PLIN2. The incidence of lipophagy is indicated by formation of red-only puncta as a result of quenching of the GFP signal in acidic lysosomes (Schulze et al., 2020). The results showed that more mCherry-only puncta were present in *PISD-LD* KD cells than in control cells (Fig. 6, E and F). Ultrastructural images also demonstrated that LDs were enclosed by double-membrane autophagosomes in *siPISD-LD* cells, but rarely in control cells (Fig. S4, L and M). After inhibition of lysosomal function by bafilomycin A1 (BafA1) treatment, more LDs were detected in autolysosomes/lysosomes in *PISD-LD* KD cells than in control cells (Fig. 6, G and H). These data suggest that depleting *PISD-LD* may promote LD degradation through the autophagy pathway.

To examine whether promoting lipophagy is a general compensatory mechanism when mitochondrial function is abnormal, we knocked down *CPT1A*, the rate-limiting enzyme in FAO, using *siRNA*. *siCPT1A* caused suppression of FA transfer from LDs to mitochondria, judged by FA transfer assays, and FAO was defective (Fig. S4, N–Q). Compared with control cells, reduced PLIN3 levels were detected in cells treated with *siCPT1A* in the presence of OA (Fig. S4, R and S). mCherry-GFP-PLIN2 assays also revealed that *siCPT1A* induced more mCherry-only puncta than control conditions (Fig. S4, T and U). These data suggest that blocking the FA β-oxidation pathway may activate autophagy to consume excess LDs.

PISD-LD negatively regulates lipophagy by inhibiting binding of LC3 to the lipophagy receptor Spartin

Spartin has recently been identified as a lipophagy receptor, which is localized on LD membranes and simultaneously binds to LC3A/C (Chung et al., 2023). In co-immunoprecipitation (co-IP) assays, both PISD-LD-mCherry and endogenous PISD were immunoprecipitated by GFP-Spartin (Fig. 6 I and Fig. S5 A). Furthermore, endogenous Spartin was pulled down by Flag-PISD-LD in Flag-KI-PISD-LD cells and by PISD-LD-HA in PISD-HA/Flag stable cells (Fig. 6 J and Fig. S5 B). Levels of PISD-LD-mCherry immunoprecipitated by GFP-Spartin were increased upon starvation (Fig. S5 C). Similar levels of Spartin were immunoprecipitated by WT PISD-LD-GFP and PISD-LD(Δenz)-GFP (Fig. S5 D), which suggests that the enzyme domain of PISD-LD is dispensable for its binding to Spartin. The overexpression of PISD-LD, but not PLIN2 or PLIN3, suppressed the binding between Spartin and LC3A/C (Fig. 6, K and L; and Fig. S5 E). When *PISD-LD* was knocked down, the binding of Spartin to LC3A/C

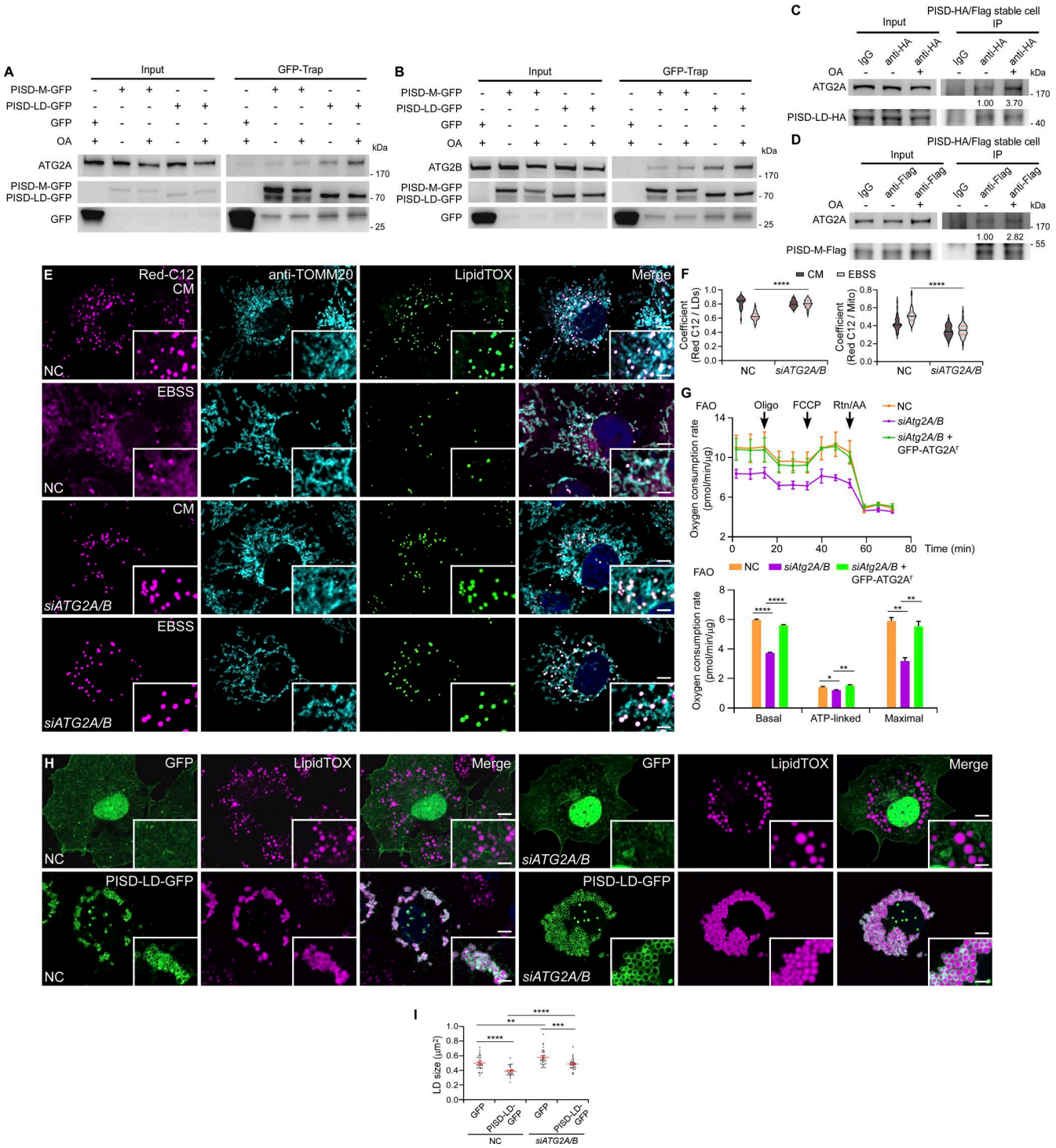

Figure 5. **LTPs ATG2A/B are recruited by PISDs to channel FAs. (A)** In a GFP-Trap assay, endogenous ATG2A is immunoprecipitated by PISD-M-GFP and PISD-LD-GFP. The level of immunoprecipitated ATG2A is dramatically increased upon OA treatment. **(B)** In a GFP-Trap assay, endogenous ATG2B is immunoprecipitated by PISD-M-GFP and PISD-LD-GFP. The level of immunoprecipitated ATG2B is dramatically increased upon OA treatment. **(C and D)** Co-IP analysis of the interaction between endogenous ATG2A and PISD-LD-HA (C) or PISD-M-Flag (D) in PISD-HA/Flag stable cells. Immunoprecipitation was performed using an HA-specific antibody (C), a Flag-specific antibody (D), or a control IgG. Quantifications of ATG2A levels (normalized by PISD-LD-HA levels in C or PISD-M-Flag levels in D) are shown. **(E and F)** Confocal images of NC and *siATG2A/B* COS7 cells loaded with Red-C12 and stained with LipidTOX (LDs; green) and anti-TOMM20 antibody (mitochondria; cyan) under fed (CM) or starved (EBSS) conditions (E). Overlap coefficients of Red-C12 with LDs or mitochondria are shown as violin plots with the solid black line indicating the median and the dotted red lines indicating the interquartile range (NC in CM, $n = 36$; NC in EBSS, $n = 26$; *siATG2A/B* in CM, $n = 54$; *siATG2A/B* in EBSS, $n = 51$) (F). NC, negative control siRNA; CM, complete medium. ****$P < 0.0001$. Bars: 5 µm; insets, 2 µm. **(G)** Seahorse FAO assays show oxidation of endogenous FAs in NC cells (orange), *siATG2A/B* cells (magenta), and *siATG2A/B* cells with GFP-ATG2A^r (green). Quantitative data of basal OCR, ATP-linked OCR, and maximal OCR in mitochondria are shown as means ± SD ($n = 3$). NC, negative control siRNA; Oligo, oligomycin; FCCP, carbonyl cyanide-p-trifluoromethoxyphenylhydrazone; Rtn, rotenone; AA, antimycin A. *$P < 0.05$; **$P < 0.01$; ****$P < 0.0001$. **(H and I)**

Confocal images of OA-stimulated NC or *siATG2A/B* COS7 cells overexpressing GFP or PISD-LD-GFP (green). LDs were stained with LipidTOX (magenta) (H). LD sizes are shown as the mean ± SEM (NC & GFP, *n* = 30; NC & PISD-LD-GFP, *n* = 26; *siATG2A/B* & GFP, *n* = 30; *siATG2A/B* & PISD-LD-GFP, *n* = 30) (I). NC, negative control siRNA. **P < 0.01; ***P < 0.001; ****P < 0.0001. Bars: 5 µm; insets, 2 µm. Source data are available for this figure: SourceData F5.

was greatly enhanced (Fig. 6, M and N). Spartin interacts with LC3 via its LC3-interacting region (LIR) motif (Chung et al., 2023). Compared with full-length Spartin, Spartin without the LIR motif (ΔLIR, deletion of residues 193–200) showed obviously reduced binding to PISD-LD (Fig. 6 I). Consistent with the increased LC3-II/I ratios in *siPISD-LD* cells (Fig. 6, A–D), more LC3A/C puncta were formed in these cells, with a notable increase in the colocalization between Spartin and LC3A/C puncta compared with control cells (Fig. 6, O and P; and Fig. S5, F and G). As previously reported (Lee et al., 2019; Pu et al., 2023; Singh et al., 2009), prolonged EBSS starvation (24 h) induced lipophagy, indicated by increased formation of mCherry-only puncta of mCherry-GFP-PLIN2, and this was suppressed by the overexpression of PISD-LD (Fig. S5, H and I). The enhanced expression of PISD-LD also suppressed the association of LC3A/C puncta with Spartin (Fig. S5, J–M). Taken together, these findings suggest that PISD-LD competes with LC3 for binding to Spartin at the same site.

We then examined the role of Spartin in lipophagy induced by disruption of LD-mito contacts. KD of *Spartin* suppressed the number of mCherry-only mCherry-GFP-PLIN2 puncta and the association of LC3A/C with LDs in *siPISD-LD* cells (Fig. 6, Q and R; and Fig. S5, N–R). Accordingly, the enlarged LDs in *siPISD-LD* cells were aggravated when *Spartin* was simultaneously knocked down (Fig. 6, S and T). A previous study reported that Spartin possesses lipid transfer activity and that depletion of its LTD impairs LD turnover through lipophagy (Wan et al., 2024). To investigate the potential involvement of Spartin in transporting FAs from LDs to mitochondria, we conducted Red-C12 FA tracking and Seahorse FAO assays in *siSpartin* cells. The results demonstrated that unlike ATG2s, depletion of *Spartin* did not influence trafficking of Red-C12 to mitochondria upon starvation or mitochondrial FAO (Fig. S5, S–U). These findings suggest that Spartin probably does not participate in FA transfer or mitochondrial FAO. Consistent with enhanced lipophagy, the LDs in *siCPT1A* cells were enlarged, and this enlargement was further enhanced by *siSpartin* (Fig. S5, V and W). The binding between PISD-LD and Spartin was not suppressed by *siCPT1A* (Fig. S5 X), which indicates that the PISD-LD–Spartin interaction may not be the primary regulatory target when FAO is blocked. Interestingly, we observed a reduction in endogenous Flag-PISD-LD levels in Flag-KI-PISD-LD cells following *siCPT1A*. This decrease was reversed by treatment with the proteasome inhibitor MG132 (Fig. S5, Y and Z). Similarly, when Flag-KI-PISD-LD cells were subjected to prolonged starvation to induce lipophagy, PISD-LD levels were reduced, and the reduction was reversed by MG132 treatment (Fig. S5, A′ and B′). These findings suggest that blocking LD-to-mitochondrion FA transfer or long-term starvation may lead to the degradation of PISD-LD via the proteasome pathway, releasing Spartin to induce lipophagy. All the above data suggest that PISD-LD suppresses Spartin-mediated lipophagy.

Mice with liver-specific knockout of *Pisd-ld* are more vulnerable to the effects of high-fat-diet feeding

To investigate the physiological function of PISD-LD, we generated mice with liver-specific knockout (KO) of *Pisd-ld*. A previous study showed that VPS4A, not Spartin, mediates lipophagy in mouse liver (Das et al., 2024). Therefore, liver-specific KO of *Pisd-ld* allows us to specifically study the role of PISD-LD in mediating LD-mito contacts and FA transfer while avoiding any confounding impact on lipophagy. To obtain the liver-specific KO mice, we first inserted LoxP sites on either side of exon 4 of *Pisd* (Fig. 7 A). Homozygous LoxP-modified mice (*Pisd-ld*$^{fl/fl}$) were then crossed with mice expressing Cre recombinase under the control of the liver-specific Alb promoter to delete exon 4 of the *Pisd* gene. The *Pisd-ld* KO efficiency in livers of KO mice was confirmed through sequencing and real-time PCR analysis (Fig. 7 B and Fig. S5 C′). There was no significant difference in *Pisd-m* transcription levels between control mice and *Pisd-ld* KO mice (Fig. S5 D′).

In order to examine the LD-mito contacts in vivo, we fed both control and KO mice with a high-fat diet to induce LDs in hepatocytes. The KO mice exhibited a greater weight gain compared with the control littermates (Fig. 7, C and D). Additionally, the liver weight of KO mice was significantly higher than that of the control mice (Fig. 7, E and F). Accordingly, we detected elevated serum and liver TAG levels and indications of increased liver damage, as shown by higher serum AST and ALT levels in the KO mice (Fig. 7, G and H). Hematoxylin and eosin (H&E) and Oil Red O staining of liver sections revealed more accumulation of LDs in the livers of KO mice compared with the controls (Fig. 7, I–K). TEM analysis revealed that LDs in KO livers were larger and had reduced contacts with mitochondria compared with controls (Fig. 7, L and M). Thus, these findings indicate an important role of PISD-LD in regulating LD-mito contacts and lipid metabolism in liver.

Discussion

Lipid metabolism is a precisely regulated process crucial for cellular energy balance and viability. Upon nutrient deprivation, neutral lipids stored within LDs are broken down into FAs and mobilized into mitochondria, where they undergo β-oxidation to produce ATP. Meanwhile, starvation triggers autophagic breakdown of LDs through lipophagy. These pathways do not function independently, but coordinate with each other to help cells survive in crisis situations. However, the underlying mechanism remains unelucidated. In this study, we identify that an LD-localized PISD isoform, PISD-LD, acts as a switch to control how cells adapt cellular FA flow in response to altered pathway availability and metabolic need. We propose the following model: (1) during starvation, contacts between LDs and mitochondria are established by formation of a tethering complex consisting of two PISD splice variants, PISD-LD and PISD-

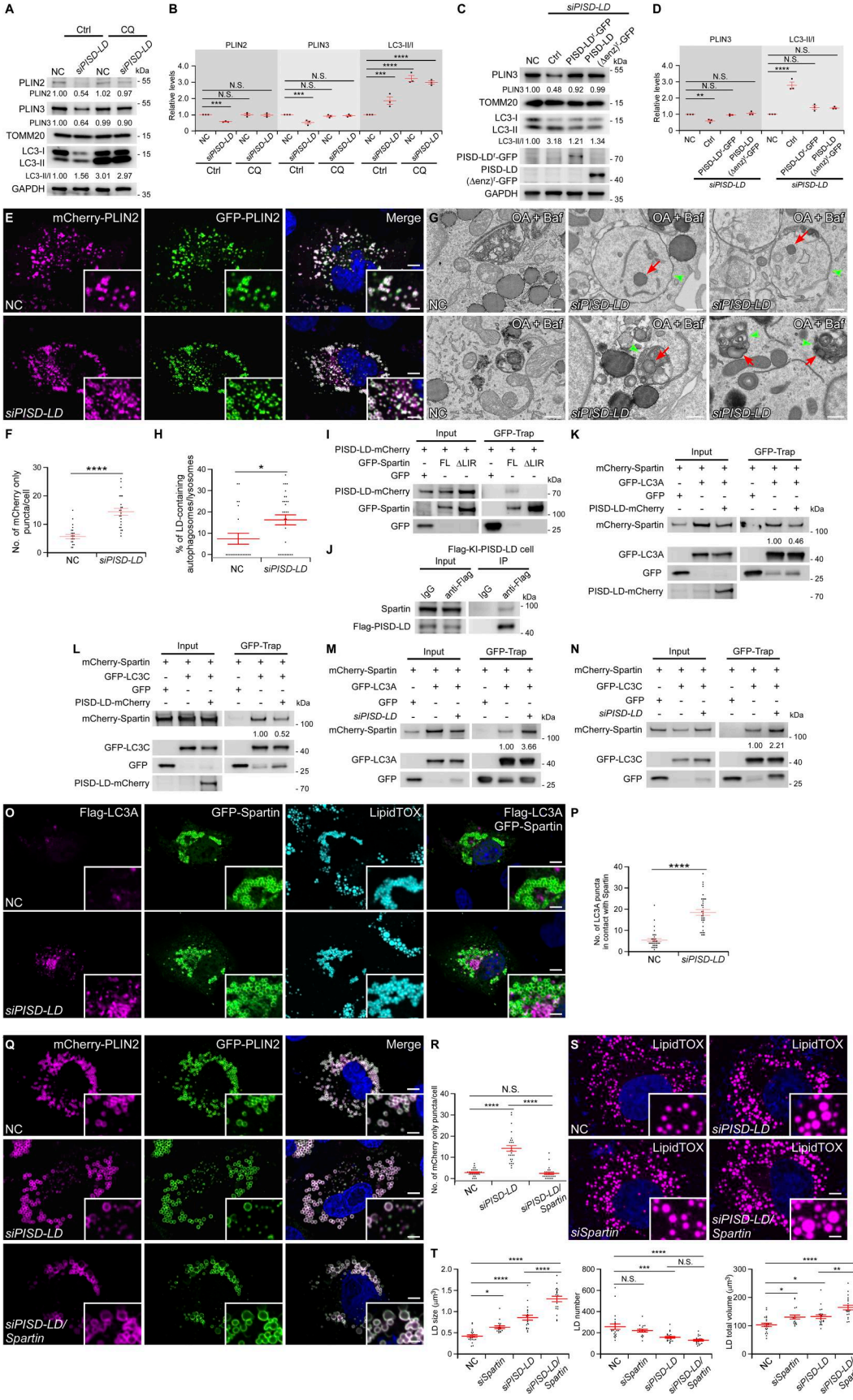

Figure 6. **PISD-LD binds to Spartin and suppresses lipophagy. (A and B)** Immunoblotting of NC and *siPISD-LD* cells with or without CQ under OA stimulation. Blots were probed with anti-PLIN2, anti-PLIN3, anti-TOMM20, anti-LC3B, and anti-GAPDH antibodies (A). Quantifications of PLIN2 levels, PLIN3 levels

(normalized by GAPDH levels), and LC3-II/I ratio are shown as the mean ± SEM (n = 3) (B). NC, negative control siRNA; CQ, chloroquine. ***P < 0.001; ****P < 0.0001; N.S., not significant. **(C and D)** Immunoblotting of NC or *siPISD-LD* COS7 cells overexpressing GFP, RNAi-resistant PISD-LD^r-GFP, or PISD-LD(Δenz)^r-GFP under OA treatment. Blots were probed with anti-PLIN3, anti-TOMM20, anti-LC3B, anti-GFP, and anti-GAPDH antibodies (C). Quantifications of PLIN3 levels (normalized by GAPDH levels) and LC3-II/I ratio are shown as the mean ± SEM (n = 3) (D). NC, negative control siRNA. **P < 0.01; ****P < 0.0001; N.S., not significant. **(E and F)** Confocal images of NC or *siPISD-LD* COS7 cells transfected with mCherry-GFP-PLIN2 under OA stimulation (E). The numbers of mCherry-only puncta per cell are shown as the mean ± SEM (NC, n = 23; *siPISD-LD*, n = 23) (F). NC, negative control siRNA. ****P < 0.0001. Bars: 5 µm; insets, 2 µm. **(G and H)** TEM images show that LDs in autophagosomes/lysosomes are detected in OA-treated *PISD-LD*–deficient cells, but rarely in NC cells, under BafA1 conditions (G). Percentage of LD-containing autophagosomes/lysosomes is shown as the mean ± SEM (NC, n = 22; *siPISD-LD*, n = 30) (H). NC, negative control siRNA. Red arrows indicate LDs in autophagosomes/lysosomes. Green arrowheads indicate autophagosomes/lysosomes. *P < 0.05. Bars, 500 nm. **(I)** In a GFP-Trap assay, PISD-LD-mCherry is immunoprecipitated by FL GFP-Spartin but not GFP-Spartin(ΔLIR). **(J)** Co-IP analysis of the interaction between endogenous Spartin and Flag-PISD-LD in Flag-KI-PISD-LD COS7 cells. Immunoprecipitation was performed using a specific antibody against Flag or a control IgG. **(K and L)** In GFP-Trap assays, levels of mCherry-Spartin immunoprecipitated by GFP-LC3A (K) or GFP-LC3C (L) are reduced by overexpression of PISD-LD-mCherry. Quantifications of Spartin levels (normalized by LC3A or LC3C levels) are shown. **(M and N)** In GFP-Trap assays, levels of mCherry-Spartin immunoprecipitated by GFP-LC3A (M) or GFP-LC3C (N) are increased in *PISD-LD* KD cells. Quantifications of Spartin levels (normalized by LC3A or LC3C levels) are shown. **(O and P)** Confocal images of OA-stimulated NC or *siPISD-LD* COS7 cells expressing Flag-LC3A (magenta) and GFP-Spartin (green). Cells were stained with LipidTOX (LDs; cyan) (O). The numbers of LC3A puncta in contact with Spartin are shown as the mean ± SEM (NC, n = 35; *siPISD-LD*, n = 35) (P). NC, negative control siRNA. ****P < 0.0001. Bars: 5 µm; insets, 2 µm. **(Q and R)** Confocal images of NC, *siPISD-LD*, or *siPISD-LD/Spartin* COS7 cells transfected with mCherry-GFP-PLIN2 under OA treatment (Q). The numbers of mCherry-only puncta per cell are shown as the mean ± SEM (NC, n = 29; *siPISD-LD*, n = 27; *siPISD-LD/Spartin*, n = 30) (R). NC, negative control siRNA. ****P < 0.0001; N.S., not significant. Bars: 5 µm; insets, 2 µm. **(S and T)** 3D projection images of OA-stimulated NC, *siPISD-LD*, *siSpartin*, or *siPISD-LD/Spartin* COS7 cells stained with LipidTOX (LDs; magenta) (S). LD sizes, numbers, and total volumes are shown as the mean ± SEM (NC, n = 22; *siSpartin*, n = 18; *siPISD-LD*, n = 21; *siPISD-LD/Spartin*, n = 20) (T). *P < 0.05; **P < 0.01; ***P < 0.001; ****P < 0.0001; N.S., not significant. Bars: 5 µm; insets, 2 µm. FL, full length. Source data are available for this figure: SourceData F6.

M, localized on LDs and mitochondria, respectively; (2) PISDs further recruit the LTP ATG2A/B to channel FAs from LDs to mitochondria for β-oxidation; (3) meanwhile, lipophagy is inhibited by PISD-LD, which sequesters the lipophagy receptor Spartin; and (4) when LD-mito contacts or mitochondrial functions are impaired, lipophagy occurs to avoid excess accumulation of FAs in LDs (Fig. 7 N).

The molecular mechanism and function of the interaction between mitochondria and LDs are not well understood (Murley and Nunnari, 2016; Veliova et al., 2020). In this study, we uncover that two different isoforms of PISD, one on LDs and the other on mitochondria, act as novel tethers to mediate LD-mito interactions. PISD is well known as the PISD in mitochondria (Calzada et al., 2016; Vance, 2008). Using both overexpression and KD experiments, we reveal the critical role of PISD-LD and PISD-M in tethering LDs and mitochondria. MCSs are generally established by the interaction of proteins localized on the opposing organelles (Elbaz and Schuldiner, 2011; Guillen-Samander and De Camilli, 2023; Helle et al., 2013; Sun et al., 2024; Voeltz et al., 2024). PISD-LD and PISD-M bring LDs and mitochondria together through their interaction with each other. This contradicts previous reports that PISD-M is localized on the IMM (Percy et al., 1983; Zborowski et al., 1983). However, the previous studies used purified OMM and IMM to perform enzymatic activity detection (Percy et al., 1983; Zborowski et al., 1983) and their results could not rule out two possibilities: (1) the biochemical separation of the two membranes might not be clean enough and the IMMs may be contaminated with the outer ones; and (2) PISD localized on the OMMs may not have decarboxylase activity. Using FPP, super-resolution imaging assays, and submitochondrial localization analysis, our results demonstrate that a proportion of PISD localizes to the OMMs, making it a potential candidate as a membrane tether. This is consistent with the previous report that PISD is transported from the OMM to the IMS by the TOM22-TOM70 complex (Horvath et al., 2012). Our submitochondrial localization assays demonstrated 60% protection of endogenous PISD-M in intact mitochondria, which suggests that 40% of PISD-M is localized on the OMM. In contrast, the FPP and super-resolution imaging assays using overexpressed PISD-M-GFP showed more obvious OMM localization of PISD-M. This discrepancy may be due to saturation of the TOM22-TOM70 complex by overexpressed PISD-M, causing inefficient translocation of the protein to the IMM. Similar findings were reported for NADH-cytochrome b5 reductase, one third of which locates on the OMM, while the other two thirds of the molecules pass through the OMM and are transported to the IMM (Hahne et al., 1994). Thus, our data suggest that PISD-M could be a potential candidate as a mitochondrial membrane tether. Based on AlphaFold 2.0 prediction, we identified key aa residues, T49/L54 and L126/T146 on PISD-LD and PISD-M, respectively, which mediate their interaction. Mutation of these sites, but not the enzymatic activity sites, blocks PISD-induced LD-mito contacts, which further supports the importance of physical interaction of PISDs in tethering LDs and mitochondria.

Two roles are proposed for LD-mito contacts: (1) mitochondria provide energy for LD expansion; and (2) LDs provide fuel for mitochondria to maintain cellular homeostasis under conditions such as starvation, which induce energy deficiency. Our data indicate that PISD-mediated LD-mito contacts facilitate the latter, as *siPISD-LD* causes enlarged LDs and impaired FA transfer from LDs to mitochondria. Again, the changed LD size is restored by reintroducing either WT PISD-LD, enzyme-defective PISD-LD, or decarboxylase domain–deleted (Δenz) mutant PISD-LD, but not mutant PISD-LD, which cannot bind PISD-M. Moreover, PISD-LD deficiency does not affect the lipid composition of LDs and mitochondria. Decarboxylase domain–deleted PISD-LD also rescued the FA transfer, FAO, and lipophagy defects in *PISD-LD* KD cells. These results further support the notion that the tethering function rather than the decarboxylase activity of PISD-LD is essential for regulating lipid metabolism. On the other hand, the reduced LD size caused by *PISD-M* KD may be confounded by the role of PISD in generating PE in

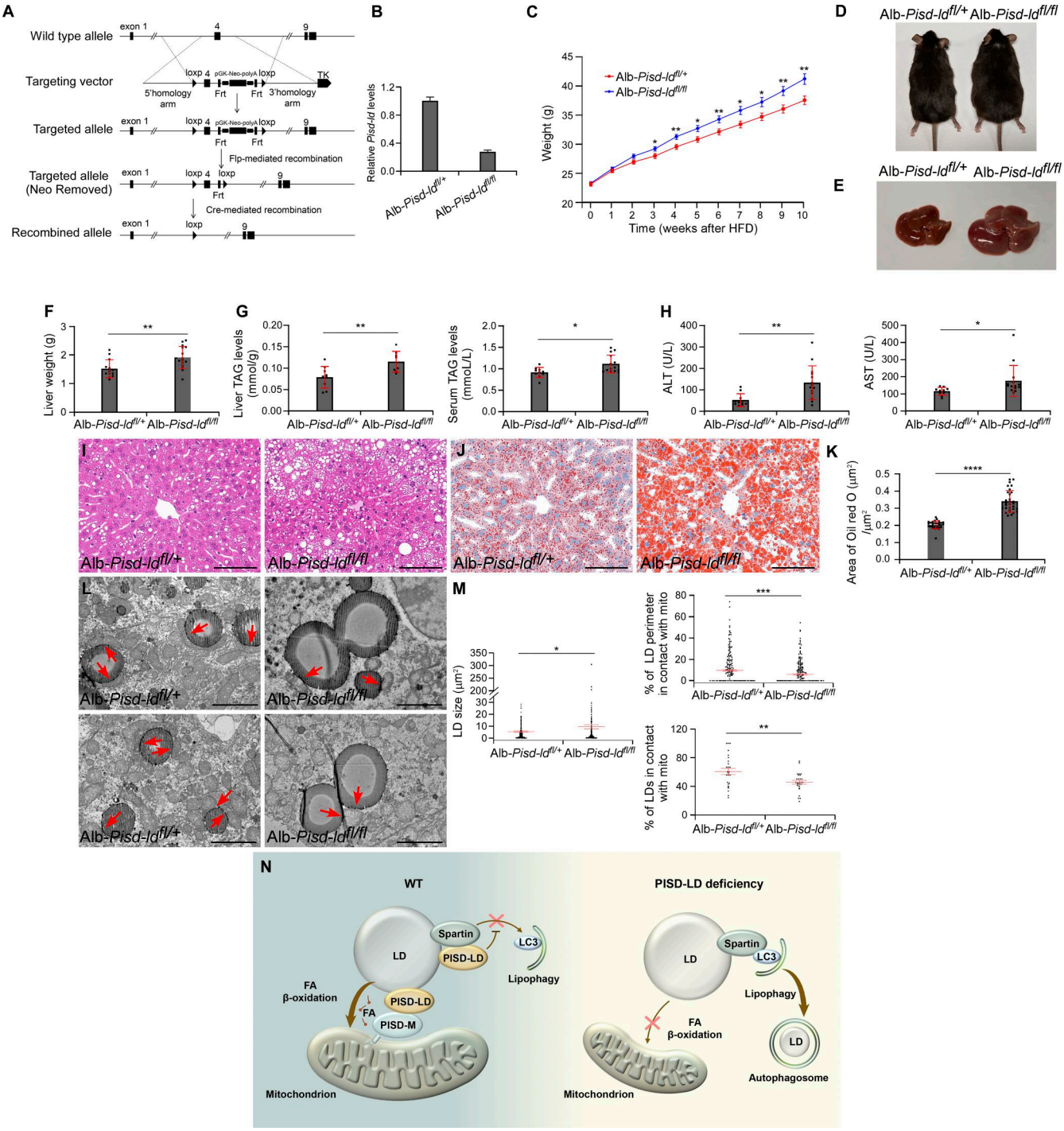

Figure 7. **Liver-specific *Pisd-ld* KO mice exhibit severe fatty liver. (A)** Strategy for targeting *Pisd-ld*. LoxP sites were inserted on either side of the *Pisd-ld*–specific exon 4 to create *Pisd-ld*$^{fl/+}$ mice. Homozygous LoxP-modified mice (*Pisd-ld*$^{fl/fl}$) were then crossed with Alb-Cre mice, which express Cre recombinase under control of the liver-specific Alb promoter. This facilitates liver-specific KO of *Pisd-ld*. **(B)** Relative *Pisd-ld* mRNA levels from livers of Alb-*Pisd-ld*$^{fl/+}$ and Alb-*Pisd-ld*$^{fl/fl}$ mice. *Pisd-ld* mRNA levels were normalized with *Actb* levels (n = 3) and are shown as the mean ± SD. **(C)** Alb-*Pisd-ld*$^{fl/fl}$ mice exhibit increased weight gain compared with Alb-*Pisd-ld*$^{fl/+}$ mice following 10 wk of feeding on a HFD starting at 8 wk of age. Body weights are shown as the mean ± SEM (Alb-*Pisd-ld*$^{fl/+}$ mice, n = 22; Alb-*Pisd-ld*$^{fl/fl}$ mice, n = 21). *P < 0.05; **P < 0.01. **(D)** Representative image showing body sizes of HFD-fed Alb-*Pisd-ld*$^{fl/+}$ and Alb-*Pisd-ld*$^{fl/fl}$ mice. **(E)** Representative image showing livers of HFD-fed Alb-*Pisd-ld*$^{fl/+}$ and Alb-*Pisd-ld*$^{fl/fl}$ mice. **(F)** Liver weights of HFD-fed Alb-*Pisd-ld*$^{fl/+}$ and Alb-*Pisd-ld*$^{fl/fl}$ mice shown as the mean ± SD (Alb-*Pisd-ld*$^{fl/+}$, n = 13; Alb-*Pisd-ld*$^{fl/fl}$, n = 15). **P < 0.01. **(G)** TAG levels in liver and serum from HFD-fed Alb-*Pisd-ld*$^{fl/+}$ and Alb-*Pisd-ld*$^{fl/fl}$ mice. Each point represents an individual mouse. The levels of liver TAG are shown as the mean ± SD (Alb-*Pisd-ld*$^{fl/+}$, n = 9; Alb-*Pisd-ld*$^{fl/fl}$, n = 8). **P < 0.01. The levels of serum TAG are shown as the mean ± SD (Alb-*Pisd-ld*$^{fl/+}$, n = 10; Alb-*Pisd-ld*$^{fl/fl}$, n = 14). *P < 0.05. **(H)** Serum ALT and AST levels from HFD-fed Alb-*Pisd-ld*$^{fl/+}$ and Alb-*Pisd-ld*$^{fl/fl}$ mice. Each point represents an individual mouse. The levels of ALT and AST are shown as the mean ± SD (Alb-*Pisd-ld*$^{fl/+}$, n = 10; Alb-*Pisd-ld*$^{fl/fl}$, n = 14). *P < 0.05; **P < 0.01. **(I)** H&E staining of liver sections from HFD-fed Alb-*Pisd-ld*$^{fl/+}$ and Alb-*Pisd-ld*$^{fl/fl}$ mice. Bars: 100 μm. **(J and K)** Oil Red O staining of liver sections from HFD-fed Alb-*Pisd-ld*$^{fl/+}$ and Alb-*Pisd-ld*$^{fl/fl}$ mice (J). Oil Red O–positive areas are quantified. Data are shown as the mean ± SD

(Alb-*Pisd-ld*$^{fl/+}$, *n* = 29 sections from three mice; Alb-*Pisd-ld*$^{fl/fl}$, *n* = 30 sections from three mice) (K). ****P < 0.0001. Bars: 100 µm. **(L and M)** TEM images of liver tissues from HFD-fed Alb-*Pisd-ld*$^{fl/+}$ and Alb-*Pisd-ld*$^{fl/fl}$ mice (L). Red arrows indicate LD-mito contacts. Graphs show LD size, percentage of LD perimeter in contact with mitochondria per LD, and percentage of LDs in contact with mitochondria per cell. Left graph: LD sizes are shown as the mean ± SEM (Alb-*Pisd-ld*$^{fl/+}$, *n* = 259 from 26 cells; Alb-*Pisd-ld*$^{fl/fl}$, *n* = 285 from 27 cells). Right graphs: percentage of LD perimeter in contact with mitochondria per LD (top) and percentage of LDs in contact with mitochondria per cell (bottom). Data are shown as the mean ± SEM (Alb-*Pisd-ld*$^{fl/+}$, *n* = 259 from 26 cells; Alb-*Pisd-ld*$^{fl/fl}$, *n* = 285 from 27 cells) (M). *P < 0.05; **P < 0.01; ***P < 0.001. Bars: 5 µm. **(N)** Schematic model. Left: in starved WT cells, PISD-LD interacts with PISD-M to tether LDs and mitochondria. PISD-LD and PISD-M further facilitate FA transfer from LDs to mitochondria for FAO. Meanwhile, PISD-LD blocks lipophagy by competing with LC3 for Spartin binding. Right: in starved cells with lowered PISD-LD activity, LD-mito contacts are reduced and Spartin engages with LC3 on autophagosomal membranes, thus promoting lipophagy. LD, lipid droplet; FA, fatty acid; HFD, high-fat diet.

mitochondria and even all over the cell. Accordingly, reintroduction of enzyme-dead PISD-M failed to increase the size of the smaller LDs in *siPISD-M* cells, while expressing tether-defective PISD-M caused bigger LDs, similar to those in *siPISD-LD* cells. Taken together, our data suggest that PISD plays a critical role in reprogramming the cell's energy source by establishing LD-mito contacts.

ATG2s were initially identified as essential autophagy proteins with an unknown mechanism of action (Velikkakath et al., 2012). Multiple studies have recently revealed that ATG2s contain hydrophobic channels that serve as a conduit for the movement of lipid molecules between two vesicles or organelles (Maeda et al., 2019; Osawa et al., 2019; Osawa et al., 2020; Valverde et al., 2019). In addition to mediating expansion of autophagic membranes, ATG2s are also involved in lysosome damage repair through direct lipid transfer (Tan and Finkel, 2022). ATG2A/B are located on LDs, and ATG2A/B deficiency causes enlarged LDs (Bersuker et al., 2018; Mailler et al., 2021; Velikkakath et al., 2012). Here, we demonstrate that ATG2A/B are recruited by PISDs to LD-mito contact sites to transport FAs from LDs to mitochondria, and they are required for efficient mitochondrial FAO, consistent with the previous findings (Mailler et al., 2021). The overexpression of ATG2A, but not its LTD-deficient mutant, partially rescued the enlarged LDs in *PISD-LD* KD cells. Meanwhile, in cells depleted of ATG2s, the overexpression of PISD-LD did not cause a reduction in LD size. These results support the involvement of ATG2s in PISD-mediated lipid transfer.

Another interesting finding of our study is that under starvation conditions, cells facilitate FA transfer from LDs to mitochondria, while inhibiting lipophagy. A previous study demonstrated that starvation induces formation of LDs, which accept FAs from the autophagosome–lysosome pathway and transfer them to mitochondria (Rambold et al., 2015). Blocking lipophagy could ensure efficient FA delivery for mitochondrial FAO and avoid FA recycling back to LDs via autophagy. Here, our data indicate that LD-localized PISD-LD acts as a switch to facilitate FA transfer as we discussed above and simultaneously prevent lipophagy. Recently, the LD surface protein Spartin was uncovered as a lipophagy receptor. It contains an LIR motif for LC3A/C binding (Chung et al., 2023). PISD-LD competes with LC3s to bind Spartin through its LIR motif. Impediment of FA transfer from LDs to mitochondria or disruption of mitochondrial function triggers lipophagy to degrade excess LDs, characterized by reduced levels of LD surface proteins and increased lipophagy flux.

In conclusion, our findings demonstrate the pivotal role of PISD isoforms in linking LDs and mitochondria, and thus elucidate a critical mechanism by which cells coordinate lipid metabolism and energy homeostasis. The interplay between PISD-LD and Spartin balances lipid catabolism through lipophagy with lipid transfer processes. This dual role of PISD-LD not only advances our understanding of intracellular lipid dynamics, but also suggests potential therapeutic targets for metabolic disorders characterized by dysregulated lipid storage and mobilization.

Materials and methods

Plasmids

PISD-LD-GFP and PISD-M-GFP were generated by inserting human PISD-LD and PISD-M, respectively, into pEGFP-N1, as previously described (Kumar et al., 2021). Myc-PISD-LD and Myc-PISD-M were generated by inserting human PISD-LD and PISD-M, respectively, into the pCMV-Myc vector. PISD-LD(Δenz)-GFP was constructed by deleting aa 115–375 from PISD-LD-GFP. PISD-M(Δenz)-GFP was constructed by deleting aa 149–409 from PISD-M-GFP. PISD-LD-BFP and PISD-LD(Δenz)-BFP were generated by replacing the GFP fragment of PISD-LD-GFP and PISD-LD(Δenz)-GFP with BFP. PISD-LD-mCherry and PISD-M-mCherry were generated by replacing the GFP fragment of PISD-LD-GFP and PISD-M-GFP, respectively, with mCherry. GFP-TM-PISD-M was constructed by inserting GFP immediately ahead of the TM domain (aa 64–82). PISD-LD(S344A)-GFP, PISD-LD(T49A/L54A)-GFP, PISD-LD(T49A/L54A)-BFP, PISD-M(S378A)-GFP, PISD-M(L126A/T146A)-mCherry, and Myc-PISD-M(L126A/T146A) were constructed by PCR-based mutagenesis. RNAi-resistant PISD-LD-GFP, PISD-LD (S344A)-GFP, PISD-LD (T49A/L54A)-GFP, PISD-LD-BFP, and PISD-LD(Δenz)-BFP were generated by PCR-based mutagenesis. GFP-ATG2A was constructed by inserting human ATG2A into the pEGFP-C1 vector. GFP-ATG2A(ΔLTD) was generated by deleting aa 1–345 from GFP-ATG2A (Valverde et al., 2019). RNAi-resistant GFP-ATG2A was generated by PCR-based mutagenesis. ATG2B-GFP was constructed by inserting human ATG2B into the pEGFP-N1 vector. PEX3-GFP was generated by inserting human PEX3 into the pEGFP-N1 vector. PEX3-PBD-GFP was generated by inserting the aa 115–148 from human PISD-M into PEX-GFP. BFP-SKL was generated by inserting the peroxisome-targeting sequence SKL into pEGFP-C1, followed by replacing the GFP fragment with BFP. GFP-ATGL was generated by inserting human ATGL into the pEGFP-C1 vector. GFP-Spartin was generated by inserting human Spartin into the pEGFP-C1 vector, and GFP-Spartin(ΔLIR) was generated by deleting aa 193–200 from GFP-Spartin. mCherry-Spartin was generated by replacing the GFP

fragment of GFP-Spartin with mCherry. Flag-LC3A and Flag-LC3C were kind gifts from Dr Yueguang Rong at University of Macau, Macau, P.R. China. GFP-LC3A and GFP-LC3C were constructed by inserting human LC3A and LC3C, respectively, into the pEGFP-C1 vector. mtPA-GFP was a kind gift from Dr Quan Chen at Nankai University, Tianjin, P.R. China. TOMM20-GFP was generated by inserting human TOMM20 into the pEGFP-N1 vector. mCherry-GFP-PLIN2 was constructed by inserting mouse PLIN2 and mCherry into the pEGFP-C1 vector (Schulze et al., 2020). NFAST and CFAST were generated by amplifying the region encoding aa 1–114 or 115–125 from synthesized full-length FAST and then insertion into the pCMV-Flag vector (Tebo and Gautier, 2019). PISD-LD-NFAST and PISD-M-CFAST were generated by inserting full-length PISD-LD and PISD-M, respectively, into the N terminus of the NFAST and CFAST plasmids. CYC1-mCherry, LACTB(1–68)-mCherry, and HSP60-mCherry were constructed by inserting human CYC1, LACTB(1–68), and HSP60, respectively, into mCherry-N1. mCherry-PLIN2 and mCherry-PLIN3 were constructed by inserting mouse PLIN2 and PLIN3, respectively, into mCherry-C1. SNAP-MAVS(510–540) was kindly provided by Dr Hong Zhang, Institute of Biophysics, Chinese Academy of Sciences.

Antibodies

The following primary antibodies were used in this study: rabbit anti-ATG2A (15011; Cell Signaling Technology), rabbit anti-ATG2B (HPA019665; Sigma-Aldrich), rabbit anti-PISD (16401-1-AP; Proteintech), mouse anti-LC3B (M152-3; MBL), rabbit anti-MFN1 (13798-1-AP; Proteintech), rabbit anti-MFN2 (12186-1-AP; Proteintech), rabbit anti-Mitofilin (10179-1-AP; Proteintech), rabbit anti-HSP60 (66041-1-Ig; Proteintech), rabbit anti-SMAC (10434-1-AP; Proteintech), rabbit anti-PLIN3 (10694-1-AP; Proteintech), rabbit anti-PLIN2 (ab108323; Abcam), rabbit anti-TOMM20 (11802-1-AP; Proteintech), rabbit anti-GM130 (11308-1-AP; Proteintech), rabbit anti-EMC1 (A305-604A-M; Thermo Fisher Scientific), rabbit anti-ATG5 (T55766F; Abmart), mouse anti-LAMP1 (555798; BD Biosciences), mouse anti-GFP (11814460001; Roche), rabbit anti-mCherry (GTX59788; GeneTex), mouse anti-Flag (F1804; Sigma-Aldrich), rabbit anti-HA (H6908; Sigma-Aldrich), rabbit anti-Myc (HX1821; Huaxingbio), mouse anti-GAPDH (60004-1-Ig; Proteintech), and mouse anti-ACTB (60008-1-Ig; Proteintech).

The following secondary antibodies were used in this study: goat anti-rabbit IgG(H + L)-HRP (BE0101; EASYBIO), goat anti-mouse IgG(H + L)-HRP (BE0102; EASYBIO), goat anti-mouse rhodamine (TRITC) (115-025-003; Jackson), goat anti-rabbit TRITC (111-025-003; Jackson), goat anti-rabbit fluorescein isothiocyanate (FITC) (111-095-003; Jackson), goat anti-mouse FITC (115-095-003; Jackson), goat anti-rabbit Alexa Fluor 647 (A-21245; Invitrogen), goat anti-mouse Alexa Fluor 647 (A-21236; Invitrogen), goat anti-mouse 6-nm gold particles (806.022; AURION), and goat anti-rabbit 15-nm gold particles (815.011; AURION).

Cell lines

COS7 cells used in this study were obtained from the ATCC. Cells were grown at 37°C with 5% CO_2 in DMEM (C11995500BT; Thermo Fisher Scientific) supplemented with 10% fetal bovine serum (FBS, 10099-141; Thermo Fisher Scientific) and 1% penicillin/streptomycin. For OA treatment, cells were cultured with 150 μM OA (O7501; Sigma-Aldrich) for 6 h. For starvation, cells were incubated in EBSS (24010043; Gibco). To inhibit autophagy, cells were treated with 50 μM CQ (C6628; Sigma-Aldrich) for 6 h. To visualize SNAP-MAVS(510–540), cells were incubated with 60 nM SNAP-Cell 647-SiR (S9102S; New England Biolabs) for 1 h at 37°C. To inhibit lysosomal degradation, cells were treated with 20 nM BafA1 (54645; Cell Signaling Technology) for 24 h.

Generation and analysis of mice with liver-specific KO of *Pisd-ld*

Pisd-ld$^{fl/+}$ transgenic mice (in which the *Pisd-ld*-specific exon 4 is flanked by LoxP sites) on a C57BL/6J background were generated by Shanghai Model Organisms. Liver-specific *Pisd-ld* KO mice were generated by crossing *Pisd-ld*$^{fl/fl}$ mice with Alb-Cre mice (#003574; Jackson Laboratory) to ultimately achieve hepatocyte-specific deletion (Alb-*Pisd-ld*$^{fl/fl}$). The Alb-*Pisd-ld*$^{fl/+}$ littermates were accordingly assigned as the control group. The following primers were used for genotyping:

Pisd-ld-Fw: 5′-GCCCTGCTTCTAGGACACTG-3′
Pisd-ld-Rv: 5′-CAAGTGTCCCTAGGCTACGC-3′
Alb-cre-Wild type-Fw: 5′-TGCAAACATCACATGCACAC-3′
Alb-cre-Mutant-Fw: 5′-GAAGCAGAAGCTTAGGAAGATGG-3′
Alb-cre-Common: 5′-TTGGCCCCTTACCATAACTG-3′.

The *Pisd-ld* KO efficiency in livers of KO mice was confirmed through sequencing and RT-PCR analysis. The following primers were used:

Genomic *Pisd-ld*-Fw: 5′-GGGCTGCTGCTGTACTTAGA-3′
Genomic *Pisd-ld*-Rv: 5′-AGTTTCAACAGTCCTTCCACACT-3′
Actb-RT-Fw: 5′-GGTGGGAATGGGTCAGAAGG-3′
Actb-RT-Rv: 5′-TGAGCAGCACAGGGTGCTC-3′
Pisd-ld-RT-Fw: 5′-ATGGAGGCCCATGAGCAGG-3′
Pisd-ld-RT-Rv: 5′-AGTGCAAGCCACATACGGG-3′
Pisd-m-RT-Fw: 5′-CTTCGTGGAGGTGTGCTGT-3′
Pisd-m-RT-Rv: 5′-ACCTGTTGCCAACAGGATGG-3′.

Mice were maintained under standard housing conditions, with ambient temperature stabilized at 24°C and a 12-h light/dark cycle, to ensure welfare and experimental consistency. Body weight was monitored weekly. The role of PISD-LD in fatty liver was investigated by feeding the mice on a high-fat diet. Male mice were fed with a 60 kcal% high-fat diet (D12492; Research Diets) for 10 wk from 8 wk of age to induce lipid accumulation in the livers. Following 10 wk on a high-fat diet, tissues and blood were harvested to assess liver weight, liver TAG, and other serum biomarkers.

Liver histology

Following fixation in 4% paraformaldehyde, liver tissues were embedded, sectioned, and stained with H&E and Oil Red O by Wuhan Servicebio Technology.

TAG and liver function tests

For serum collection, blood samples were clotted at room temperature for 30 min and centrifuged at 3,000 rpm for 10 min.

The supernatant serum was stored at −80°C. Serum TAG and liver function markers (AST and ALT) were measured by the Laboratory Animal Center, Southern University of Science and Technology. Liver TAG was assessed using a commercial kit (S0219S; Beyotime) according to the manufacturer's protocol.

Generation of the PISD-HA/Flag stable cell line using the piggyBac transposon system

To generate stable cell lines using the piggyBac transposon system, human *PISD-M* cDNA with a C-terminal 3 × Flag tag and *PISD-LD* cDNA with a C-terminal 3 × HA tag were cloned into the piggyBac dual promoter vector. COS7 cells were transfected with the piggyBac dual promoter plasmid (carrying the two tagged genes) and the piggyBac transposase expression plasmid in a ratio of 3:1. After 48 h of transfection, cells were selected in DMEM containing 10% FBS and 3 μg/ml puromycin for an additional 48 h. Following selection, positively transfected cells were subjected to single-cell cloning by limiting dilution in 96-well plates. After 4 wk, the monoclonal cell lines were screened by sequencing and RT-PCR to confirm the correct insertion and appropriate expression level. Successfully constructed cells were verified by immunoblotting using anti-Flag and anti-HA antibodies.

FA esterification and TAG lipolysis assay

COS7 cells were transfected with siRNAs as indicated. To assess FA esterification, at 72 h after transfection, cells were incubated with medium containing 150 μM OA supplemented with 0.5 μCi/ml ^{3}H-labeled OA (NET289005MC; PerkinElmer). Cells were harvested at 0 and 6 h.

To evaluate TAG lipolysis, cells were treated for 16 h with 150 μM OA supplemented with 0.5 μCi/ml ^{3}H-labeled OA. The medium was then replaced with OA-free medium, and cells were collected at 0 and 6 h.

For lipid analysis, cells were lysed and then subjected to lipid extraction. TAG was separated by thin-layer chromatography. Then, the TAG spots were collected and mixed with scintillation fluid (OptiPhase HiSafe 3; 1200.437; Revvity) to measure radioactive TAG using a liquid scintillation counter (300SL; Hidex).

Quantitative RT-PCR

COS7 cells were transfected with siRNAs as indicated. 72 h after transfection, RNA was isolated with TRIzol (15596026; Invitrogen) according to the manufacturer's instructions. cDNA was reverse-transcribed using SuperRT cDNA Synthesis Kit (CW0741M; CWBIO). The cDNA was analyzed using quantitative PCR with 2*TSINGKE Master qPCR Mix (TSE201; TSINGKE) on an Applied Biosystems QuantStudio 1 (Thermo Fisher Scientific). The primers for quantitative PCR assays in this study were as follows:

F-*Chlorocebus sabaeus PISD-LD*, 5′-TGTCAGTCAGAGGCGCGG-3′;

R-*Chlorocebus sabaeus PISD-LD*, 5′-TTACGGGCCTCCATCCCA-3′;

F-*Chlorocebus sabaeus PISD-M*, 5′-TACAGCCCTTGTGGAAGC TG-3′;

R-*Chlorocebus sabaeus PISD-M*, 5′-AGTGACCAGCAAGTTTGG GT-3′;

F-*Chlorocebus sabaeus Spartin*, 5′-TACGCACCAGGCTGGAAA TT-3′;

R-*Chlorocebus sabaeus Spartin*, 5′-CCTGCACTTGGAGTTGAG GT-3′;

F-*Chlorocebus sabaeus CPT1A*, 5′-GCCTATTTTGGACGGGGG AA-3′;

R-*Chlorocebus sabaeus CPT1A*, 5′-CTCCGCGTTGATGCCTAT CT-3′;

F-*Chlorocebus sabaeus ACTB*, 5′-AGACCTGTACGCCAACAC AG-3′;

R-*Chlorocebus sabaeus ACTB*, 5′-ACTCCTGCTTGCTGATCCAC-3′;

F-PISD-HA/Flag stable cell-*PISD-LD-HA*, 5′-GGCCCCCAAGGA CTTCAATT-3′;

R-PISD-HA/Flag stable cell-*PISD-LD-HA*, 5′-GGATAGCCC GCATAGTCAGG-3′;

F-PISD-HA/Flag stable cell-*PISD-M-Flag*, 5′-GGCCCCCAA GGACTTCAATT-3′;

R-PISD-HA/Flag stable cell-*PISD-M-Flag*, 5′-AGTCTCCGTCGT GGTCCTTA-3′.

Transfection and RNAi

Plasmid transfections were performed in Opti-MEM (31985070; Thermo Fisher Scientific) with the Neofect DNA transfection reagent (TF20121201; Neofect). For siRNA transfections, cells were transfected with Lipofectamine RNAiMAX (13778150; Invitrogen) in Opti-MEM. 72 h later, cells were collected later for further analysis. Oligonucleotides for siRNAs used in this study were as follows:

NC, 5′-UUCUCCGAACGUGUCACGUTT-3′;

Chlorocebus sabaeus PISD-LD, 5′-CCUUGACCGUCCUCUACU ATT-3′;

Chlorocebus sabaeus PISD-M, 5′-GAUUGGAGAUUCCACCCA ATT-3′;

Chlorocebus sabaeus ATG5, 5′-GAAAGAAGCUGAUGCUUU ATT-3′;

Chlorocebus sabaeus Spartin, 5′-GGCAAAGAAGAAAGAUAA ATT-3′;

Chlorocebus sabaeus PISD, 5′-GCUUCGUGACGCACACCAATT-3′;

Chlorocebus sabaeus CPT1A, 5′-GCGUGAUGACAACAAUGU ATT-3′;

Chlorocebus sabaeus ATG2A, 5′-GCAUUCCCAGUUGUUGGA GUUCCUATT-3′;

Chlorocebus sabaeus ATG2B, 5′-AGGUCUCUCUUGUCUGGC AUCUUUATT-3′.

Immunostaining

Cells plated on coverslips (C015001; Matsunami) were fixed with 4% paraformaldehyde (E672002; Sangon Biotech) for 30 min and then permeabilized with 0.1% Triton in PBS for 20 min at room temperature. Following this, cells were blocked using 1% BSA in PBS for 1 h at room temperature and subsequently incubated overnight at 4°C with primary antibodies specific to the target proteins. Cells were then washed three times with PBS (140 mM NaCl, 2.7 mM KCl, 10 mM Na_2HPO_4, 1.8 mM KH_2PO_4) and then incubated with fluorescently labeled secondary antibodies for 1 h at room temperature. LDs were stained with LipidTOX Green

(H34475; Thermo Fisher Scientific) or LipidTOX Red (H34476; Thermo Fisher Scientific). Finally, coverslips were mounted using an antifade solution (without DAPI, ZLI-9556; with DAPI, ZLI-9557; OriGene) and the cells were imaged at room temperature using a confocal microscope (LSM 980 Meta plus Zeiss Axiovert zoom, Zeiss) equipped with a 63×/1.40 oil-immersion objective lens (Plan-Apochromat, Zeiss) and a point detector (GaAsP PMT, Zeiss). The imaging was performed using Zeiss ZEN software (blue edition).

Co-IP and immunoblotting

For co-IP assays, cells were transfected with the indicated plasmids for 24–48 h or siRNAs for 72 h. Subsequently, cells were lysed with a lysis buffer containing 20 mM HEPES (pH 7.5), 150 mM NaCl, 1 mM EDTA, and 0.1% Triton X-100 supplemented with a protease inhibitor cocktail (11836170001; Roche). Cell homogenates were incubated on ice for 30 min and then centrifuged at 13,000 rpm for 10 min at 4°C. The supernatants were transferred to new tubes and incubated with GFP-Trap (KTSM1334; Shenzhen KT Life Technology) or mCherry-Trap (KTSM1334; Shenzhen KT Life Technology) agarose beads at 4°C for 1 h. The bound proteins were eluted with SDS sample buffer and further analyzed by immunoblotting.

For immunoblotting, cells were lysed using a lysis buffer composed of 20 mM HEPES (pH 7.5), 150 mM NaCl, 1 mM EDTA, 0.1% Triton X-100, and a protease inhibitor cocktail. The lysates were incubated on ice for 30 min. Following incubation, the homogenates were centrifuged at 13,000 rpm for 10 min at 4°C. The supernatants were collected and mixed with SDS sample buffer, then subjected to SDS-PAGE. Proteins were transferred onto hydrophobic PVDF membranes with a 0.45-µm pore size (IPVH00010, Millipore). Specific primary and secondary antibodies were used to detect the protein signals, which were visualized using the 5200SF imaging system (5200SF; Tanon).

Transmission electron microscopy

COS7 cells with the indicated treatments were fixed with 2.5% glutaraldehyde in PBS at 4°C overnight. After washing with PBS twice and with distilled water once, cells were postfixed with 1% OsO_4 and 1.5% $K_3Fe(CN)_6$ for 90 min at room temperature. After washing with water, samples were stained with ice-cold 2% aqueous uranyl acetate for 1 h at room temperature. Then, samples were gradually dehydrated with increasing concentrations of ethanol and embedded in epoxy EMBED-812 resin. Ultrathin sections were stained with uranyl acetate and lead citrate. In Fig. 1 H; Fig. S3 P; Fig. S4, D and L; Fig. 6 G; and Fig. 7 L, to increase the signal of LDs, OTO staining was applied. Briefly, cells were first fixed in 1% OsO4 and 1.5% $K_3Fe(CN)_6$ for 1 h at room temperature. After fixation, the cells were washed with distilled water and then placed in a 1% thiocarbohydrazide solution for 30 min at room temperature. Following this, the cells were washed again with distilled water and incubated with 1% OsO_4 for an additional 30 min at room temperature. After washing with water, samples were stained with ice-cold 2% aqueous uranyl acetate for 1 h at room temperature. Finally, the cells underwent graded dehydration and embedding. Images were captured under a 120 kV electron microscope (Tecnai Spirit, FEI) at 100 kV at room temperature with a CCD camera (MoradaG3, EMSIS) using RADIUS (EMSIS) software.

Focused ion beam scanning electron microscopy

For FIB-SEM imaging, OA-treated COS7 cells were transfected with GFP or PISD-LD-GFP. GFP-positive cells were sorted using a BD FACSAria SORP flow cytometer (BD Biosciences) and then immediately fixed with 2.5% glutaraldehyde in PBS at 4°C overnight. The samples were postfixed with 1% osmium tetroxide and 1.5% potassium hexacyanoferrate(III), followed by 1% thiocarbohydrazide and 1% osmium tetroxide. The samples were then stained with 2% aqueous uranyl acetate and 0.66% lead aspartate, dehydrated through a graded ethanol series (30%, 50%, 70%, 80%, 90%, 95%, and 100%) and 100% acetone, then embedded in SPI-Pon 812 resin (SPI Supplies). The cell samples were imaged volumetrically in 3D using FIB-SEM (Helios G4 UC; Thermo Fisher Scientific). The milling and imaging processes were sequentially repeated, and a long series of images (250) was acquired through a fully automated procedure. The image resolution on the xy plane was ∼5 nm per pixel. The resolution on the z axis was 10 nm, which corresponded to the thickness of the material layer removed by FIB. The final image was captured at a pixel size of 4,069 × 3,536, providing a field of view of ∼20 × 18 µm, equivalent to a magnification of 5,000 ×. Amira software (Amira 2020.3; Thermo Fisher Scientific) was used for automatic alignment, image denoising, and signal normalization across slices.

Immuno-electron microscopy

COS7 cells were seeded into a high-pressure freezer carrier (W131310; Science Services) and frozen with a high-pressure freezer (EM ICE High Pressure Freezer, Leica). After high-pressure freezing, samples were freeze-substituted in acetone containing 0.25% glutaraldehyde and 0.1% uranyl acetate at −80°C for 24–48 h in a freeze-substitution device (EM AFS2; Leica) and warmed to −45°C. After freeze substitution, the samples were washed three times with 100% acetone for 30 min at −45°C. The samples were infiltrated sequentially in 33%, 66%, and 100% Lowicryl HM20 resin diluted with acetone at −45°C, each for 12 h. After that, the samples were embedded in 100% Lowicryl HM20 at −45°C overnight. Finally, the HM20 polymerization was completed under ultraviolet illumination at −45°C for 48 h. After polymerization, the sample blocks were cut into 70-nm ultrathin sections and preincubated in 2% BSA for 30 min at room temperature, followed by incubation with the primary antibodies for 3 h at room temperature. After three washes with 1% BSA, secondary antibodies conjugated with gold particles were applied for 1 h at room temperature. Then, the sections were washed three times with 1% BSA. The grids were treated with 3% uranyl acetate for 2 min and washed three times with ddH_2O, once with 0.25% lead citrate for 2 min, then three times with ddH_2O. Images were collected with an electron microscope (Talos 120C; Thermo Fisher Scientific) operating at 120 kV.

Fluorescent FA pulse-chase assay of BODIPY-C12 (Red-C12)/BODIPY-palmitate

COS7 cells transfected with the indicated siRNAs were incubated in EBSS containing 1 µM BODIPY 558/568-C12 (D3835; Thermo

Fisher Scientific) or BODIPY-palmitate (HY-168375; MCE) for 2 h for uptake. Cells were washed three times with PBS, then chased in complete medium or EBSS for 5 h. Subsequent immunostaining with anti-TOMM20 was performed, and LDs were stained with LipidTOX.

FAO assay

The FAO assay was performed using the Seahorse XF Cell Mito Stress Test kit (103015-100; Agilent). Firstly, OA-treated COS7 cells transfected with the indicated siRNAs and plasmids were plated in an XFe96 Cell Culture Microplate (101085-004; Agilent) in culture medium. The subsequent steps were performed as previously described (Wang et al., 2021). Briefly, 24 h prior to the assay, the culture medium was replaced with substrate-limited medium (DMEM containing 0.5 mM glucose, 1 mM GlutaMAX, 0.5 mM carnitine, and 1% FBS). Then, cells were washed twice with FAO assay medium (containing 5 mM HEPES, pH 7.4, 111 mM NaCl, 4.7 mM KCl, 1.25 mM $CaCl_2$, 2 mM $MgSO_4$, 1.2 mM NaH_2PO_4, 2.5 mM glucose, and 0.5 mM carnitine) and incubated with 180 µl/well FAO assay medium in a non-CO_2 incubator for 30 min at 37°C. After preloading with test compounds (2.5 µM oligomycin, 2 µM FCCP, 0.5 µM rotenone, and antimycin A), the Cell Mito Stress Test was run with XFe96 Analyzer (Agilent) according to the analyzer's instructions. The total protein content in each well was quantified using BCA Protein Assay Kit (23225; Pierce) according to the manufacturer's instructions. The oxygen consumption rate (OCR) of each sample was normalized with protein content in each well.

The data analysis was conducted as follows:

Basal OCR in mitochondria = basal OCR - nonmitochondrial OCR; ATP-linked OCR = basal OCR - proton leak-linked OCR; maximal OCR in mitochondria = maximal OCR - nonmitochondrial OCR.

Flow cytometry

For the analysis of FA uptake, COS7 cells were transfected with the indicated plasmids for 24–48 h or siRNAs for 72 h. Then, the cells were incubated in EBSS containing 1 µM BODIPY 558/568 C12 for 2 h to facilitate uptake. After multiple washes with PBS, the cells were collected and analyzed using a BD FACSCanto SORP flow cytometer (BD Biosciences). Cells were analyzed for Red-C12 signal intensity and distribution using FlowJo 10.8.1.

split-Fluorescence-Activating and Absorption-Shifting Tag

To visualize the location of the interaction between PISD-LD and PISD-M, COS7 cells were plated on 35-mm glass-bottom cell culture dishes, and cotransfected with PISD-M-CFAST and PISD-LD-NFAST for 24 h. Control experiments included transfections with NFAST paired with PISD-M-CFAST and CFAST paired with PISD-LD-NFAST. SNAP-MAVS(510–540) was also transfected with the FAST plasmids to serve as a mitochondrial marker. Following transfection, the cells were treated with 150 µM OA for 6 h. Subsequently, the cells were stained with LipidTOX Red to label LDs and SNAP-Cell 647-SiR to label the SNAP-tagged mitochondrial marker for 1 h. Before imaging, 2 µM HMBR (S34223, Shanghai Yuanye Biotechnology), which fluoresces instantly upon noncovalent binding to FAST (Bottone et al., 2023), was added to the prepared cells. Images were captured at room temperature using ZEN Blue software on a confocal microscope (LSM 980; Zeiss) with a 63 × /1.40 oil-immersion objective lens.

mtPA-GFP–based mitochondrial dynamic assay

COS7 cells were plated on 35-mm glass-bottom cell culture dishes. Cells were transfected with NC or *siPISD-LD* for 72 h and a mtPA-GFP plasmid for 24 h. After prestaining with 500 nM MitoTracker (M22426; Invitrogen) for 30 min, cells were loaded to a laser scanning confocal microscope (LSM 980; Zeiss). Live-cell imaging was performed with the 63 × /1.40 oil-immersion objective lens using the 405-nm laser for mtPA-GFP photoactivation, 488 nm for GFP, and 639 nm for MitoTracker Deep Red.

FPP assay

COS7 cells were plated on 35-mm glass-bottom cell culture dishes (706001; NEST) and transfected with the indicated plasmids. After washing three times with KHM buffer (125 mM potassium acetate, 25 mM HEPES, pH 7.2, 2.5 mM magnesium acetate), cells were treated with 160 µM digitonin for 5 min at room temperature. Then, 50 µg/ml pK (P2308; Sigma-Aldrich) was added, and live-cell images were captured at room temperature using ZEN Blue software on a confocal microscope (LSM 980; Zeiss) with a 63 × /1.40 oil-immersion objective lens.

Super-resolution imaging

COS7 cells were plated on 35-mm dishes with 20-mm glass-bottom dishes (D35-20-1-N; Cellvis) and transfected with the indicated plasmids. Images were captured using a multi-SIM imaging system (NanoInsights-Tech Co., Ltd.) equipped with a 100 × 1.49NA oil objective (Nikon CFI SR HP Apo) and a Photometrics Kinetix camera. The SIM images were taken using single-slice mode with 50-mW laser power and 30-ms exposure time. Images were reconstructed using SIM Imaging Analyser software (NanoInsights-Tech), and then analyzed with ImageJ (v.2.1.4.7, NIH). During image acquisition, cells were placed in a humidified chamber maintained at 37°C in the presence of 5% CO_2.

Isolation of LDs

COS7 cells were grown in 15-cm dishes in the presence of 150 µM OA for 24 h. LDs were isolated using an LD isolation kit (MET5001; Cell Biolabs) following the manufacturer's instructions. The purified LDs were subsequently used for lipidomics, proteomics, and immunoblotting analyses.

Isolation of mitochondria

OA-treated COS7 cells grown in 15-cm dishes were harvested to collect cell pellets. Mitochondria were purified as previously described (Cao et al., 2023). Briefly, cell pellets were resuspended in homogenization buffer (20 mM HEPES/KOH pH 7.4, 220 mM mannitol, 70 mM sucrose, 1 mM EDTA, 0.5% BSA) containing 1 mM PMSF and a protease inhibitor cocktail, and incubated on ice for 20 min. Using a Dounce homogenizer with a tight pestle, cells were then homogenized by performing 20–30 strokes on ice. The homogenates were centrifuged at 3,200 *g* for

5 min at 4°C, and this step was repeated at least three times. The supernatants were then centrifuged at 18,000 *g* for 10 min at 4°C to pellet the mitochondria. The mitochondrial pellets were washed twice with homogenization buffer without 0.5% BSA and protease inhibitors. The isolated mitochondria were used for further lipidomics and immunoblotting analyses.

Submitochondrial localization analysis

Submitochondrial localization was performed as previously described (Cao et al., 2023). Briefly, six equal mitochondrial pellets were prepared from 10–15 15-cm dishes. The samples were divided into three groups: Intact, Swollen, and Triton. Two samples in each group were resuspended in basic homogenization buffer (20 mM HEPES/KOH, pH 7.4, 220 mM mannitol, 70 mM sucrose, 1 mM EDTA), hypotonic swelling buffer (10 mM HEPES/KOH, pH 7.4, 1 mM EDTA), and basic homogenization buffer containing 0.5% Triton X-100, and incubated on ice for 20 min. One sample from each group was treated with pK (50 µg/ml) for 20 min on ice, while the other one served as an untreated control. Mitochondrial proteins were precipitated by 30% trichloroacetic acid on ice for 10 min, followed by centrifugation at 18,000*g* for 10 min at 4°C. The pellets were washed with 100% ethanol, dissolved in SDS loading buffer, and denatured at 98°C for 5–10 min. The protein samples were then used for immunoblotting analysis.

Lipidomics

Lipids were extracted from approximately one million cells using a modified version of Bligh and Dyer's method as described previously (Miao et al., 2022). Briefly, cells were homogenized in 750 µl of chloroform: methanol: Milli-Q H_2O (3:6:1) (vol/vol/vol). The homogenate was then incubated at 1500 rpm for 1 h at 4°C. At the end of the incubation, 350 µl of deionized water and 250 µl of chloroform were added to induce phase separation. The samples were then centrifuged, and the lower organic phase containing lipids was extracted into a clean tube. Lipid extraction was repeated once by adding 450 µl of chloroform to the remaining cells in the aqueous phase, and the lipid extracts were pooled into a single tube and dried in the SpeedVac under OH mode. Samples were stored at −80°C until further analysis. Upper aqueous phases and cell pellets were dried in a SpeedVac under H_2O mode. The total protein content was determined from the dried pellet using Pierce BCA Protein Assay Kit according to the manufacturer's protocol.

Lipidomics analyses were conducted at LipidALL Technologies using a Shimadzu Nexera 20AD-HPLC coupled with Sciex QTRAP 6500 PLUS as reported previously (Lam et al., 2021). Separation of individual classes of polar lipids by normal-phase HPLC was carried out using a TUP-HB silica column (i.d., 150 × 2.1 mm, 3 µm) with the following conditions: mobile phase A (chloroform:methanol:ammonium hydroxide, 89.5:10:0.5) and mobile phase B (chloroform:methanol:ammonium hydroxide: water, 55:39:0.5:5.5). MRM transitions were set up for comparative analysis of various polar lipids. Individual lipid species were quantified by referencing to spiked internal standards. d9-PC32:0(16:0/16:0), d9-PC36:1p(18:0p/18:1), d7-PE33:1(15:0/18:1), d9-PE36:1p(18:0p/18:1), d31-PS(d31-16:0/18:1), d7-PA33:1(15:0/18:1), d7-PG33:1(15:0/18:1), d7-PI33:1(15:0/18:1), C17-SL, d5-CL72:8(18:2)4, C14-BMP, d7-LPE18:1, C17-LPI, C17-LPA, and C17-LPS were obtained from Avanti Polar Lipids. GM3-d18:1/18:0-d3 was purchased from Matreya LLC. Free FAs were quantitated using d31-16:0 (Sigma-Aldrich) and d8-20:4 (Cayman Chemicals).

Glycerol lipids including diacylglycerols (DAGs) and TAGs were quantified using a modified version of reverse-phase HPLC/MRM (Shui et al., 2010). Separation of neutral lipids was achieved on a Phenomenex Kinetex C18 column (i.d. 4.6 × 100 mm, 2.6 µm) using an isocratic mobile phase containing chloroform:methanol:0.1 M ammonium acetate 100:100:4 (vol/vol/vol) at a flow rate of 300 µl for 10 min. Levels of short-, medium-, and long-chain TAGs were calculated by referencing to respective spiked internal standards of TAG(14:0)3-d5, TAG(16:0)3-d5, and TAG(18:0)3-d5 obtained from CDN isotopes. DAGs were quantified using d5-DAG17:0/17:0 and d5-DAG18:1/18:1 as internal standards (Avanti Polar Lipids).

Proteomics

200 µl of protein lysis buffer (8 M urea, protease inhibitor) was added to each sample. After full lysis, the samples were physically crushed and sonicated for 3 min, then centrifuged at 15,000 *g* for 10 min. The protein concentration of each sample was determined using BCA Protein Assay Kit.

DTT was added to the lysate to achieve a final concentration of 10 mM, and the mixture was incubated at 56°C for 1 h. The lysate was cooled to room temperature, then IAA was added to achieve a final concentration of 55 mM, and the mixture was incubated in the dark for 45 min. Next, an appropriate amount of protein was taken from each sample and digested using the published filter-aided sample preparation protocol (Wiśniewski et al., 2009). The following day, the samples were applied to ultrafiltration devices, which were centrifuged at 13,000 *g* and room temperature for 10 min. The liquid was collected in a new Eppendorf tube, and the samples were vacuum-dried.

Solvent A for liquid chromatography was composed of 0.1% formic acid in water, while solvent B contained 80% acetonitrile and 0.1% formic acid in water. Lyophilized peptides were dissolved in 0.1% formic acid in water and then centrifuged for 15 min at 17,000 *g*. The resulting supernatant was injected into a C18 analytical column (75 µm × 20 cm) using an EASY-nLC 1200 HPLC (Thermo Fisher Scientific) at a max pressure of 500 bar with 12 µl solvent A. Peptides were eluted from the analytical column at a flow rate of 300 nl/min with a gradient to 6% B at 0 min, 30% B at 42 min, 42% B at 51 min, and finally 95% B at 56–60 min. The eluted peptide was sprayed at a voltage of 2.3 kV and analyzed by a Thermo Fisher Scientific Orbitrap Q Exactive HF mass spectrometer coupled with a Nanospray Flex ion source. The ion transfer tube was set at 320°C (Wang et al., 2020). The mass spectrometry (MS) scan resolution was 120,000, the scanning range was 398–900 m/z, and the maximum injection time was set to 80 ms. The MS/MS scan resolution was 30,000, with 32 scanning windows, and with first mass for MS at 200 m/z. The collision energy was 28%, and the maximum injection time was set to auto.

Raw DIA data were searched against a preferred database (*Chlorocebus sabaeus*, green monkey) using Spectronaut 19

(Biognosys). The digestion enzyme was Trypsin/P, and the max missed cleavage was set at 2. Methionine oxidation and acetylation of the protein N terminus were set as variable modifications. FDR was controlled to 1% at both protein and peptide levels. A minimum of one peptide per protein was allowed for protein identification. The other parameters were set as default (Wang et al., 2020). The *Chlorocebus sabaeus* database used was downloaded from UniProt.

Statistical analysis

Co-IP and immunoblotting results were obtained from a minimum of three independent experiments. Protein band signal intensities from immunoblotting were analyzed with ImageJ. For FPP data analysis, the intensity at the pre-pK point was normalized to 100%, and the intensity immediately after bleaching was set to 0% using ImageJ software. For analysis of FA transfer in fluorescent FA pulse-chase assays, colocalization of BODIPY 558/568 C12 with LDs or mitochondria was analyzed using the Just Another Colocalization Plugin in ImageJ. Colocalization data are shown as overlap coefficient.

The contact areas between LDs and mitochondria in z-stack fluorescence images of cells under various treatments were quantified using Imaris (v8.3, Bitplane). The intensity-based colocalization (coloc) function in Imaris was used to build the colocalization channel for analysis. By adjusting the intensity threshold, the rendered surfaces optimally represented the mitochondria, LDs, and colocalization channels. The ratio of the contact surface area to the total surface area of mitochondria or LDs was calculated to quantify the degree of interaction.

The contacts between LDs and mitochondria in TEM images of cells under various treatments were measured and quantified using ImageJ. The percentage of LDs in contact with mitochondria was calculated as (number of LDs in contact with mitochondria/total number of LDs) × 100. The percentage of LD perimeter in contact with mitochondria was calculated as (contact length of individual LD/perimeter of the LD) × 100. The percentage of mitochondria in contact with LDs was calculated as (number of mitochondria in contact with LDs/total number of mitochondria) × 100. The percentage of mitochondrial perimeter in contact with LDs was calculated as (contact length of individual mitochondrion/perimeter of the mitochondrion) × 100.

LD masses were quantified by importing z-stack fluorescence images into Imaris software. Utilizing the spot rendering function in Imaris, a three-dimensional reconstruction of the LDs was performed. Fine adjustments were made to the parameters for spot diameter, quality, and intensity to ensure that nearly all LDs were included in the rendering outcomes. The quantity and volume of the LDs were analyzed automatically by Imaris, with the data subsequently exported for statistical assessment.

For proteomics and lipidomics analysis, MS intensities were first converted to relative densities by normalizing each protein's abundance to the total intensity within its row. Log2 transformation and Z-score normalization were subsequently applied to enhance comparability by centering each protein's distribution around zero and scaling it to unit variance. Hierarchical clustering was then performed, and a heat map was generated to visualize protein or lipid abundance similarity.

Sample sizes were determined based on preliminary experiments using Cohen's d. Cell samples were allocated randomly into experimental groups. Cells with signs of senescence (e.g., enlarged or flattened morphology) or apoptosis (e.g., fragmented nuclei) were excluded from further analysis. Statistical parameters, including the number of samples (*n*), standard deviation, or standard error of the mean, are provided in the figure legends. Data were presumed to follow a normal distribution without formal testing. A two-tailed *t* test was used for comparisons between two groups. One-way ANOVA was used to assess statistical significance. For comparison of percentages between control and treated cells, the chi-square test was used to test significance. A P value < 0.05 was considered significant.

Online supplemental material

Fig. S1 demonstrates that distinct PISD isoforms mediate physical contact sites between LDs and mitochondria. Fig. S2 shows that a portion of PISD-M specifically targets the mitochondrial outer membrane. Fig. S3 confirms that the silencing of *PISD-LD* does not alter the lipid composition of either LDs or mitochondria. Fig. S4 reveals that PISDs bind the LTPs ATG2A/B to facilitate FA transport. Fig. S5 reveals that the activation of lipophagy triggered by a deficiency in PISD-LD is mediated by the lipophagy receptor Spartin. Video 1 provides a three-dimensional FIB-SEM reconstruction of MCSs between mitochondria and LDs in control cells expressing GFP. Video 2 utilizes FIB-SEM to illustrate the significant expansion of contact sites at the LD–mitochondria interface upon the overexpression of PISD-LD-GFP.

Data availability

All data are available in the main text or the supplemental materials. Further reasonable requests should be directed to and will be fulfilled by the lead contact, Yan G. Zhao (zhaoyan@sustech.edu.cn).

Acknowledgments

We are grateful to Dr. Isabel Hanson for editing work. We would like to acknowledge the technical support from SUSTech Core Research Facilities. All radioactivity experiments were performed at the radioactive isotope laboratory (Institute of Biophysics, CAS), with guidance from H. J. Zhang and Y Zhao in handling radioactive materials.

This work was supported by the National Key R&D Program of China (2025YFA0923000 to Y.G. Zhao), the Shenzhen Medical Research Fund (B2502010, E250200110, E250200112 to Y.G. Zhao), Fundamental and Interdisciplinary Disciplines Breakthrough Plan of the Ministry of Education of China (JYB2025XDXM505 to Y.G. Zhao), the National Key R&D Program of China (2021YFA1300800 to Y.G. Zhao), the Shenzhen Science and Technology Program (JCYJ20240813100300001 to Y.G. Zhao), the Guangdong Innovative and Entrepreneurial Research Team Program (2021ZT09Y104 to Y.G. Zhao), the Shenzhen Talent Program (KQTD20210811090115021 to Y.G. Zhao), Shenzhen-Hong Kong Institute of Brain Science-Shenzhen Fundamental

Research Institutions (2024SHIBS0002 to Y.G. Zhao), the Research Grants Council of Hong Kong (14106622, 14110923, 14114924, and AoE/M-402/25-N to X. Zhuang) and SUSTech Distinguished Young Scientist Team Program to Y.G. Zhao.

Author contributions: Hanbing Xue: investigation, methodology, validation, visualization, and writing—original draft, review, and editing. Xingwen Hu: data curation, formal analysis, investigation, methodology, validation, visualization, and writing—original draft. Zhenni Yang: data curation, formal analysis, investigation, validation, and visualization. Yiqing Cao: formal analysis. Qi Zhu: validation. Hongyu Zhao: investigation. Xiaoli Ma: investigation. Tianxin Lei: formal analysis. Dian Zhuang: investigation and validation. Jing Zheng: methodology. Siqi Guo: software. Xiaochuan Fu: resources and supervision. Ka Kit Chung: resources. Pingsheng Liu: investigation and methodology. Xiaohong Zhuang: investigation and supervision. Zhengyu Liang: formal analysis. Sicong He: data curation and formal analysis. Hui Jiang: methodology. Yan G. Zhao: conceptualization, data curation, formal analysis, funding acquisition, investigation, methodology, project administration, resources, supervision, visualization, and writing—original draft, review, and editing.

Disclosures: The authors declare no competing interests exist.

Submitted: 18 May 2026
Revised: 5 June 2026
Accepted: 8 June 2026

References

Ben M'barek, K., D. Ajjaji, A. Chorlay, S. Vanni, L. Foret, and A.R. Thiam. 2017. ER membrane phospholipids and surface tension control cellular lipid droplet formation. *Dev. Cell*. 41:591–604.e7. https://doi.org/10.1016/j.devcel.2017.05.012

Bersuker, K., C.W.H. Peterson, M. To, S.J. Sahl, V. Savikhin, E.A. Grossman, D.K. Nomura, and J.A. Olzmann. 2018. A proximity labeling strategy provides insights into the composition and dynamics of lipid droplet proteomes. *Dev. Cell*. 44:97–112.e7. https://doi.org/10.1016/j.devcel.2017.11.020

Bottone, S., O. Joliot, Z.V. Cakil, L. El Hajji, L.-M. Rakotoarison, G. Boncompain, F. Perez, and A. Gautier. 2023. A fluorogenic chemically induced dimerization technology for controlling, imaging and sensing protein proximity. *Nat. Methods*. 20:1553–1562. https://doi.org/10.1038/s41592-023-01988-8

Boutant, M., S.S. Kulkarni, M. Joffraud, J. Ratajczak, M. Valera-Alberni, R. Combe, A. Zorzano, and C. Canto. 2017. Mfn2 is critical for brown adipose tissue thermogenic function. *EMBO J.* 36:1543–1558. https://doi.org/10.15252/embj.201694914

Brown, T.A., A.N. Tkachuk, G. Shtengel, B.G. Kopek, D.F. Bogenhagen, H.F. Hess, and D.A. Clayton. 2011. Superresolution fluorescence imaging of mitochondrial nucleoids reveals their spatial range, limits, and membrane interaction. *Mol. Cell Biol.* 31:4994–5010. https://doi.org/10.1128/MCB.05694-11

Calzada, E., O. Onguka, and S.M. Claypool. 2016. Phosphatidylethanolamine metabolism in health and disease. *Int. Rev. Cell Mol Biol*. 321:29–88. https://doi.org/10.1016/bs.ircmb.2015.10.001

Cao, Y., J. Zheng, H. Wan, Y. Sun, S. Fu, S. Liu, B. He, G. Cai, Y. Cao, H. Huang, et al. 2023. A mitochondrial SCF-FBXL4 ubiquitin E3 ligase complex degrades BNIP3 and NIX to restrain mitophagy and prevent mitochondrial disease. *EMBO J.* 42:e113033. https://doi.org/10.15252/embj.2022113033

Chen, L., Y. Liu, J. Zhang, T. Song, J. Wu, and Z. Ren. 2025. AMPK regulates ARF1 localization to membrane contact sites to facilitate fatty acid transfer between lipid droplets and mitochondria. *Cell Death Dis.* 16:623. https://doi.org/10.1038/s41419-025-07957-7

Choi, H., Y. Liao, Y. Yoon, J. Grimm, N. Wang, L. Lavis, R. Singer, and J. Lippincott-Schwartz. 2026. Secretome translation shaped by lysosomes and lunapark-marked ER junctions. *Nature*. 649:227–236. https://doi.org/10.1038/s41586-025-09718-0

Chung, J., J. Park, Z.W. Lai, T.J. Lambert, R.C. Richards, J. Zhang, T.C. Walther, and R.V. Farese Jr. 2023. The troyer syndrome protein spartin mediates selective autophagy of lipid droplets. *Nat. Cell Biol.* 25:1101–1110. https://doi.org/10.1038/s41556-023-01178-w

Cui, L., and P. Liu. 2020. Two types of contact between lipid droplets and mitochondria. *Front. Cell Dev. Biol.* 8:618322. https://doi.org/10.3389/fcell.2020.618322

Dakal, T.C., F. Xiao, C. Bhusal, P. Sabapathy, R. Segal, J. Chen, and X. Bai. 2025. Lipids dysregulation in diseases: Core concepts, targets and treatment strategies. *Lipids Health Dis.* 24:61. https://doi.org/10.1186/s12944-024-02425-1

Das, D., M. Sharma, D. Gahlot, S. Nia, C. Gain, M. Mecklenburg, Z. Zhou, M. Bourdenx, L. Thukral, N. Martinez-Lopez, and R. Singh. 2024. VPS4A is the selective receptor for lipophagy in mice and humans. *Mol. Cell*. 84:4436–4453.e8. https://doi.org/10.1016/j.molcel.2024.10.022

Elbaz, Y., and M. Schuldiner. 2011. Staying in touch: The molecular era of organelle contact sites. *Trends Biochem. Sci.* 36:616–623. https://doi.org/10.1016/j.tibs.2011.08.004

Farese, R.V., Jr., and T.C. Walther. 2023. Glycerolipid synthesis and lipid droplet formation in the endoplasmic reticulum. *Cold Spring Harb. Perspect. Biol.* 15:a041246. https://doi.org/10.1101/cshperspect.a041246

Freyre, C.A.C., P.C. Rauher, C.S. Ejsing, and R.W. Klemm. 2019. MIGA2 Links Mitochondria, the ER, and Lipid Droplets and Promotes De Novo Lipogenesis in Adipocytes. *Mol. Cell*. 76:811–825.e14. https://doi.org/10.1016/j.molcel.2019.09.011

Gao, M., X. Huang, B. Song, and H. Yang. 2019. The biogenesis of lipid droplets: Lipids take center stage. *Prog. Lipid Res.* 75:100989. https://doi.org/10.1016/j.plipres.2019.100989

Grimm, J., B. English, H. Choi, A. Muthusamy, B. Mehl, P. Dong, T. Brown, J. Lippincott-Schwartz, Z. Liu, T. Lionnet, and L. Lavis. 2016. Bright photoactivatable fluorophores for single-molecule imaging. *Nat. Methods*. 13:985–988. https://doi.org/10.1038/nmeth.4034

Guillen-Samander, A., and P. De Camilli. 2023. Endoplasmic reticulum membrane contact sites, lipid transport, and neurodegeneration. *Cold Spring Harb. Perspect. Biol.* 15:a041257. https://doi.org/10.1101/cshperspect.a041257

Hacker, C., T.A. Schrader, and M. Schrader. 2023. Ultrastructural analysis and quantification of peroxisome-organelle contacts. *Methods Mol. Biol.* 2643:105–122. https://doi.org/10.1007/978-1-0716-3048-8_8

Hahne, K., V. Haucke, L. Ramage, and G. Schatz. 1994. Incomplete arrest in the outer membrane sorts NADH-cytochrome b5 reductase to two different submitochondrial compartments. *Cell*. 79:829–839. https://doi.org/10.1016/0092-8674(94)90072-8

Helle, S.C., G. Kanfer, K. Kolar, A. Lang, A.H. Michel, and B. Kornmann. 2013. Organization and function of membrane contact sites. *Biochim. Biophys. Acta*. 1833:2526–2541. https://doi.org/10.1016/j.bbamcr.2013.01.028

Horvath, S.E., L. Bottinger, F.N. Vogtle, N. Wiedemann, C. Meisinger, T. Becker, and G. Daum. 2012. Processing and topology of the yeast mitochondrial phosphatidylserine decarboxylase 1. *J. Biol. Chem.* 287:36744–36755. https://doi.org/10.1074/jbc.M112.398107

Kim, P.K., R.T. Mullen, U. Schumann, and J. Lippincott-Schwartz. 2006. The origin and maintenance of mammalian peroxisomes involves a de novo PEX16-dependent pathway from the ER. *J. Cell Biol.* 173:521–532. https://doi.org/10.1083/jcb.200601036

Kumar, S., C. Chitraju, R.V. Farese Jr., T.C. Walther, and C.G. Burd. 2021. Conditional targeting of phosphatidylserine decarboxylase to lipid droplets. *Biol. Open*. 10:bio058516. https://doi.org/10.1242/bio.058516

Lam, J., P. Katti, M. Biete, M. Mungai, S. AshShareef, K. Neikirk, E.G. Lopez, Z. Vue, T.A. Christensen, H.K. Beasley, et al. 2021a. A universal approach to analyzing transmission electron microscopy with ImageJ. *Cells*. 10:2177. https://doi.org/10.3390/cells10092177

Lam, S.M., C. Zhang, Z. Wang, Z. Ni, S. Zhang, S. Yang, X. Huang, L. Mo, J. Li, B. Lee, et al. 2021b. A multi-omics investigation of the composition and function of extracellular vesicles along the temporal trajectory of COVID-19. *Nat. Metab.* 3:909–922. https://doi.org/10.1038/s42255-021-00425-4

Lee, D.-H., J. Ahn, Y. Jang, T. Ha, and C. Jung. 2019. Oleic acid-induced defective autolysosome shows impaired lipid degradation. *Biochem. Biophysical Res. Commun.* 513:553–559. https://doi.org/10.1016/j.bbrc.2019.04.040

Maeda, S., C. Otomo, and T. Otomo. 2019. The autophagic membrane tether ATG2A transfers lipids between membranes. *Elife*. 8:e45777. https://doi.org/10.7554/eLife.45777

Mailler, E., C.M. Guardia, X. Bai, M. Jarnik, C.D. Williamson, Y. Li, N. Maio, A. Golden, and J.S. Bonifacino. 2021. The autophagy protein ATG9A

enables lipid mobilization from lipid droplets. *Nat. Commun.* 12:6750. https://doi.org/10.1038/s41467-021-26999-x

Mauthe, M., I. Orhon, C. Rocchi, X. Zhou, M. Luhr, K.J. Hijlkema, R.P. Coppes, N. Engedal, M. Mari, and F. Reggiori. 2018. Chloroquine inhibits autophagic flux by decreasing autophagosome-lysosome fusion. *Autophagy*. 14:1435–1455. https://doi.org/10.1080/15548627.2018.1474314

Miao, H., B. Li, Z. Wang, J. Mu, Y. Tian, B. Jiang, S. Zhang, X. Gong, G. Shui, and S.M. Lam. 2022. Lipidome atlas of the developing heart uncovers dynamic membrane lipid attributes underlying cardiac structural and metabolic maturation. *Research*. 2022:0006. https://doi.org/10.34133/research.0006

Molina, A.J., and O.S. Shirihai. 2009. Monitoring mitochondrial dynamics with photoactivatable [corrected] green fluorescent protein. *Methods Enzymol.* 457:289–304.

Murley, A., and J. Nunnari. 2016. The emerging network of mitochondria-organelle contacts. *Mol. Cell*. 61:648–653. https://doi.org/10.1016/j.molcel.2016.01.031

Nguyen, T.B., S.M. Louie, J.R. Daniele, Q. Tran, A. Dillin, R. Zoncu, D.K. Nomura, and J.A. Olzmann. 2017. DGAT1-Dependent lipid droplet biogenesis protects mitochondrial function during starvation-induced autophagy. *Dev. Cell*. 42:9–21.e5. https://doi.org/10.1016/j.devcel.2017.06.003

Olzmann, J.A., and P. Carvalho. 2019. Dynamics and functions of lipid droplets. *Nat. Rev. Mol. Cell Biol.* 20:137–155. https://doi.org/10.1038/s41580-018-0085-z

Onguka, O., E. Calzada, O.B. Ogunbona, and S.M. Claypool. 2015. Phosphatidylserine decarboxylase 1 autocatalysis and function does not require a mitochondrial-specific factor. *J. Biol. Chem.* 290:12744–12752. https://doi.org/10.1074/jbc.m115.641118

Osawa, T., Y. Ishii, and N.N. Noda. 2020. Human ATG2B possesses a lipid transfer activity which is accelerated by negatively charged lipids and WIPI4. *Genes Cells*. 25:65–70. https://doi.org/10.1111/gtc.12733

Osawa, T., T. Kotani, T. Kawaoka, E. Hirata, K. Suzuki, H. Nakatogawa, Y. Ohsumi, and N.N. Noda. 2019. Atg2 mediates direct lipid transfer between membranes for autophagosome formation. *Nat. Struct. Mol. Biol.* 26:281–288. https://doi.org/10.1038/s41594-019-0203-4

Ouyang, Q., Q. Chen, S. Ke, L. Ding, X. Yang, P. Rong, W. Feng, Y. Cao, Q. Wang, M. Li, et al. 2023. Rab8a as a mitochondrial receptor for lipid droplets in skeletal muscle. *Dev. Cell*. 58:289–305.e6. https://doi.org/10.1016/j.devcel.2023.01.007

Percy, A.K., J.F. Moore, M.A. Carson, and C.J. Waechter. 1983. Characterization of brain phosphatidylserine decarboxylase: Localization in the mitochondrial inner membrane. *Arch. Biochem. Biophys.* 223:484–494. https://doi.org/10.1016/0003-9861(83)90613-6

Peter, V.G., M. Quinodoz, J. Pinto-Basto, S.B. Sousa, S.A. Di Gioia, G. Soares, G. Ferraz Leal, E.D. Silva, R.P. Gobert, N. Miyake, et al. 2019. The liberfarb syndrome, a multisystem disorder affecting eye, ear, bone, and brain development, is caused by a founder pathogenic variant in the *PISD* gene. *Genet. Med.* 21:2734–2743. https://doi.org/10.1038/s41436-019-0595-x

Polianskyte, Z., N. Peitsaro, A. Dapkunas, J. Liobikas, R. Soliymani, M. Lalowski, O. Speer, J. Seitsonen, S. Butcher, G.M. Cereghetti, et al. 2009. LACTB is a filament-forming protein localized in mitochondria. *Proc. Natl. Acad. Sci. USA*. 106:18960–18965. https://doi.org/10.1073/pnas.0906734106

Pu, M., W. Zheng, H. Zhang, W. Wan, C. Peng, X. Chen, X. Liu, Z. Xu, T. Zhou, Q. Sun, et al. 2023. ORP8 acts as a lipophagy receptor to mediate lipid droplet turnover. *Protein Cell*. 14:653–667. https://doi.org/10.1093/procel/pwac063

Rambold, A.S., S. Cohen, and J. Lippincott-Schwartz. 2015. Fatty acid trafficking in starved cells: Regulation by lipid droplet lipolysis, autophagy, and mitochondrial fusion dynamics. *Dev. Cell*. 32:678–692. https://doi.org/10.1016/j.devcel.2015.01.029

Schulze, R.J., E.W. Krueger, S.G. Weller, K.M. Johnson, C.A. Casey, M.B. Schott, and M.A. McNiven. 2020. Direct lysosome-based autophagy of lipid droplets in hepatocytes. *Proc. Natl. Acad. Sci. USA*. 117:32443–32452. https://doi.org/10.1073/pnas.2011442117

Shui, G., X.L. Guan, C.P. Low, G.H. Chua, J.S.Y. Goh, H. Yang, and M.R. Wenk. 2010. Toward one step analysis of cellular lipidomes using liquid chromatography coupled with mass spectrometry: Application to *Saccharomyces cerevisiae* and *Schizosaccharomyces pombe* lipidomics. *Mol. Biosyst.* 6:1008–1017. https://doi.org/10.1039/b913353d

Singh, R., and A.M. Cuervo. 2012. Lipophagy: Connecting autophagy and lipid metabolism. *Int. J. Cell Biol.* 2012:282041. https://doi.org/10.1155/2012/282041

Singh, R., S. Kaushik, Y. Wang, Y. Xiang, I. Novak, M. Komatsu, K. Tanaka, A.M. Cuervo, and M.J. Czaja. 2009. Autophagy regulates lipid metabolism. *Nature*. 458:1131–1135. https://doi.org/10.1038/nature07976

St Germain, M., R. Iraji, and M. Bakovic. 2022. Phosphatidylethanolamine homeostasis under conditions of impaired CDP-ethanolamine pathway or phosphatidylserine decarboxylation. *Front. Nutr.* 9:1094273. https://doi.org/10.3389/fnut.2022.1094273

Sun, S., G. Zhao, M. Jia, Q. Jiang, S. Li, H. Wang, W. Li, Y. Wang, X. Bian, Y.G. Zhao, et al. 2024. Stay in touch with the endoplasmic reticulum. *Sci. China Life Sci.* 67:230–257. https://doi.org/10.1007/s11427-023-2443-9

Talari, N., U. Mattam, N. Meher, A. Paripati, K. Mahadev, T. Krishnamoorthy, and N. Sepuri. 2023. Lipid-droplet associated mitochondria promote fatty-acid oxidation through a distinct bioenergetic pattern in male Wistar rats. *Nat. Commun.* 14:766. https://doi.org/10.1038/s41467-023-36432-0

Tan, J.X., and T. Finkel. 2022. A phosphoinositide signalling pathway mediates rapid lysosomal repair. *Nature*. 609:815–821. https://doi.org/10.1038/s41586-022-05164-4

Tebo, A.G., and A. Gautier. 2019. A split fluorescent reporter with rapid and reversible complementation. *Nat. Commun.* 10:2822. https://doi.org/10.1038/s41467-019-10855-0

Valm, A.M., S. Cohen, W.R. Legant, J. Melunis, U. Hershberg, E. Wait, A.R. Cohen, M.W. Davidson, E. Betzig, and J. Lippincott-Schwartz. 2017. Applying systems-level spectral imaging and analysis to reveal the organelle interactome. *Nature*. 546:162–167. https://doi.org/10.1038/nature22369

Valverde, D.P., S. Yu, V. Boggavarapu, N. Kumar, J.A. Lees, T. Walz, K.M. Reinisch, and T.J. Melia. 2019. ATG2 transports lipids to promote autophagosome biogenesis. *J. Cell Biol.* 218:1787–1798. https://doi.org/10.1083/jcb.201811139

Vance, J.E. 2008. Phosphatidylserine and phosphatidylethanolamine in mammalian cells: Two metabolically related aminophospholipids. *J. Lipid Res.* 49:1377–1387. https://doi.org/10.1194/jlr.R700020-JLR200

Velikkakath, A.K., T. Nishimura, E. Oita, N. Ishihara, and N. Mizushima. 2012. Mammalian Atg2 proteins are essential for autophagosome formation and important for regulation of size and distribution of lipid droplets. *Mol Biol Cell*. 23:896–909. https://doi.org/10.1091/mbc.E11-09-0785

Veliova, M., A. Petcherski, M. Liesa, and O.S. Shirihai. 2020. The biology of lipid droplet-bound mitochondria. *Semin Cell Dev Biol*. 108:55–64. https://doi.org/10.1016/j.semcdb.2020.04.013

Voeltz, G.K., E.M. Sawyer, G. Hajnoczky, and W.A. Prinz. 2024. Making the connection: How membrane contact sites have changed our view of organelle biology. *Cell*. 187:257–270. https://doi.org/10.1016/j.cell.2023.11.040

Wan, N., Z. Hong, M. Parson, J. Korfhage, J. Burke, T. Melia, and K. Reinisch. 2024. Spartin-mediated lipid transfer facilitates lipid droplet turnover. *Proc. Natl. Acad. Sci. USA*. 121:e2314093121. https://doi.org/10.1073/pnas.2314093121

Wang, G., Y. Wang, L. Zhang, Q. Cai, Y. Lin, L. Lin, and X. Lin. 2020. Proteomics analysis reveals the effect of *Aeromonas hydrophila* sirtuin *CobB* on biological functions. *J. Proteomics*. 225:103848. https://doi.org/10.1016/j.jprot.2020.103848

Wang, H., U. Sreenivasan, H. Hu, A. Saladino, B.M. Polster, L.M. Lund, D.W. Gong, W.C. Stanley, and C. Sztalryd. 2011. Perilipin 5, a lipid droplet-associated protein, provides physical and metabolic linkage to mitochondria. *J. Lipid Res.* 52:2159–2168. https://doi.org/10.1194/jlr.M017939

Wang, J., N. Fang, J. Xiong, Y. Du, Y. Cao, and W.K. Ji. 2021. An ESCRT-dependent step in fatty acid transfer from lipid droplets to mitochondria through VPS13D-TSG101 interactions. *Nat. Commun.* 12:1252. https://doi.org/10.1038/s41467-021-21525-5

Wiśniewski, J.R., A. Zougman, N. Nagaraj, and M. Mann. 2009. Universal sample preparation method for proteome analysis. *Nat. Methods*. 6:359–U360. https://doi.org/10.1038/nmeth.1322

Yang, H., A. Galea, V. Sytnyk, and M. Crossley. 2012. Controlling the size of lipid droplets: Lipid and protein factors. *Curr Opin Cell Biol*. 24:509–516. https://doi.org/10.1016/j.ceb.2012.05.012

Yoon, H., J.L. Shaw, M.C. Haigis, and A. Greka. 2021. Lipid metabolism in sickness and in health: Emerging regulators of lipotoxicity. *Mol. Cell*. 81:3708–3730. https://doi.org/10.1016/j.molcel.2021.08.027

Zadoorian, A., X. Du, and H. Yang. 2023. Lipid droplet biogenesis and functions in health and disease. *Nat. Rev. Endocrinol.* 19:443–459. https://doi.org/10.1038/s41574-023-00845-0

Zborowski, J., A. Dygas, and L. Wojtczak. 1983. Phosphatidylserine decarboxylase is located on the external side of the inner mitochondrial membrane. *FEBS Lett.* 157:179–182. https://doi.org/10.1016/0014-5793(83)81141-7

Zechner, R., F. Madeo, and D. Kratky. 2017. Cytosolic lipolysis and lipophagy: Two sides of the same coin. *Nat. Rev. Mol. Cell Biol.* 18:671–684. https://doi.org/10.1038/nrm.2017.76

Zhao, T., C.M. Goedhart, P.N. Sam, R. Sabouny, S. Lingrell, A.J. Cornish, R.E. Lamont, F.P. Bernier, D. Sinasac, J.S. Parboosingh, et al. 2019. *PISD* is a mitochondrial disease gene causing skeletal dysplasia, cataracts, and white matter changes. *Life Sci. Alliance*. 2:e201900353. https://doi.org/10.26508/lsa.201900353

JCB

Supplemental material

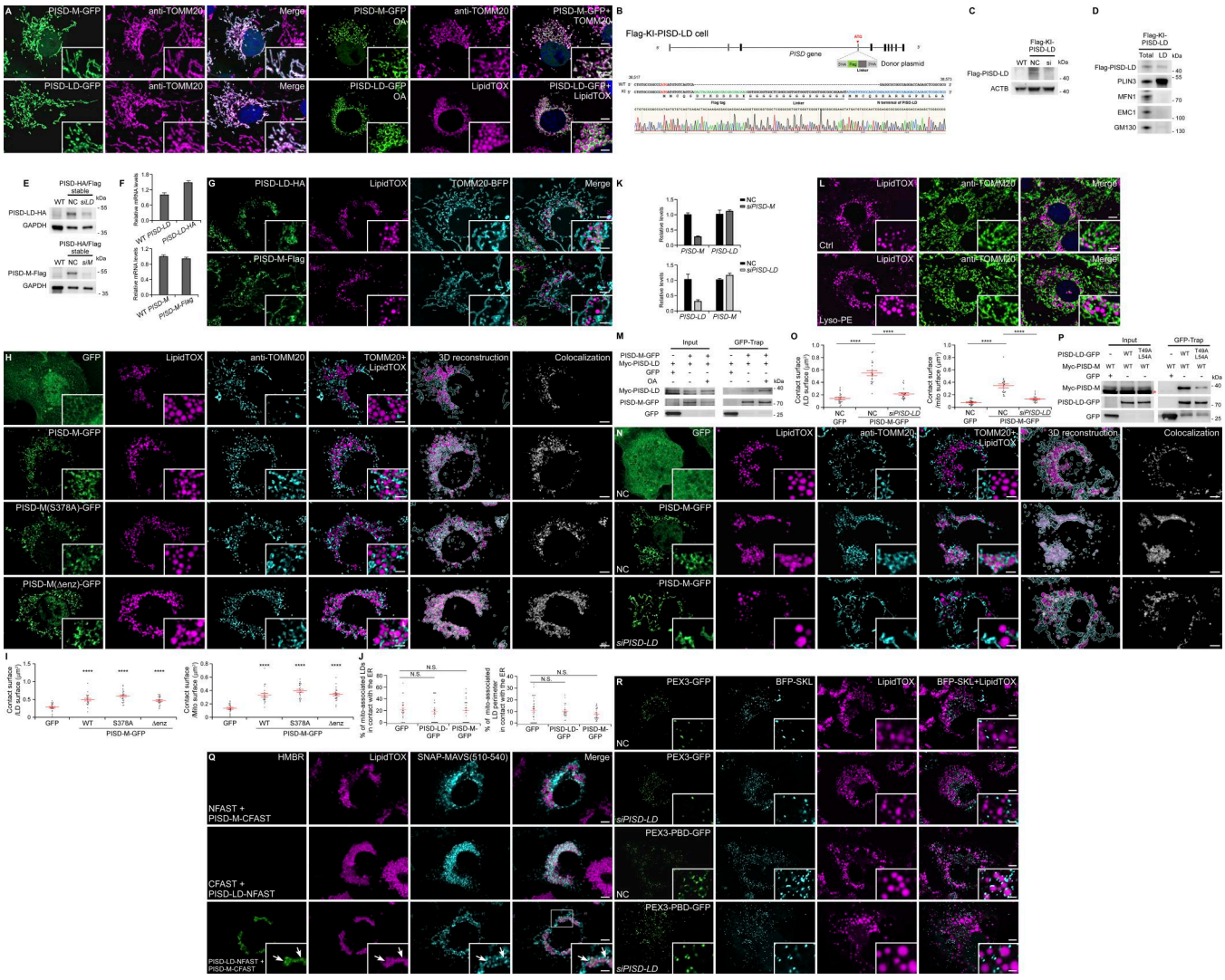

Figure S1. **PISD isoforms mediate LD-mito contacts, related to Figs. 1 and 2. (A)** Confocal images of COS7 cells expressing PISD-M-GFP or PISD-LD-GFP (green), with or without OA treatment. Cells were stained with anti-TOMM20 antibody (mitochondria; magenta) or LipidTOX (LDs; magenta). Bars: 5 µm; insets, 2 µm. **(B)** Strategy for generating Flag-KI-PISD-LD cells and validation by sequencing. **(C)** Immunoblotting of WT cells and NC or *siPISD-LD* Flag-KI-PISD-LD cells. Blots were probed with anti-Flag and anti-ACTB antibodies. The specific signal detected by the anti-Flag antibody in Flag-KI-PISD-LD cells is diminished following *siPISD-LD* treatment. WT, wild type. NC, negative control siRNA; si, *siPISD-LD*. **(D)** Immunoblotting of the LD fraction, isolated by flotation from Flag-KI-PISD-LD cells, shows the localization of Flag-PISD-LD to LDs. Blots were probed with anti-Flag, anti-PLIN3 (LDs), anti-MFN1 (mitochondria), anti-EMC1 (ER), and anti-GM130 (Golgi) antibodies. **(E)** Immunoblotting of WT cells (no siRNA treatment) and PISD-HA/Flag stable cells treated with NC siRNA or *siPISD-LD* (*siLD*, top) and NC siRNA or *siPISD-M* (*siM*, bottom). Blots were probed with anti-HA or anti-Flag and anti-GAPDH antibodies. The specific signal detected by the anti-HA or anti-Flag antibody in PISD-HA/Flag stable cells is diminished following *siPISD-LD* or *siPISD-M* treatment, respectively. WT, wild type. NC, negative control siRNA. **(F)** Relative *PISD-LD-HA* and *PISD-M-Flag* mRNA levels and endogenous *PISD-LD* and *PISD-M* mRNA levels in PISD-HA/Flag stable cells. Quantitative data normalized by *ACTB* levels are presented as the mean ± SD (n = 4). **(G)** Confocal images of PISD-LD-HA (green) or PISD-M-Flag (green) in PISD-HA/Flag stable cells that were transfected with TOMM20-BFP (cyan) following OA treatment. Cells were immunostained with anti-HA antibody or anti-Flag antibody and stained with LipidTOX (LDs; magenta). Bars: 5 µm; insets: 2 µm. **(H and I)** Single focal plane images of OA-treated COS7 cells overexpressing GFP, PISD-M-GFP, PISD-M(S378A)-GFP, or PISD-M(Δenz)-GFP (green) and stained with LipidTOX (LDs; magenta) and anti-TOMM20 antibody (mitochondria; cyan) (H). Additionally, 3D reconstructions and contact surfaces of the LipidTOX and TOMM20 channels (white) are shown (H). Graphs show contact surface areas, normalized by LD and mitochondrial surface areas. Each point represents an individual cell. Data are shown as the mean ± SEM (GFP, n = 22; PISD-M-GFP, n = 20; PISD-M(S378A)-GFP, n = 22; PISD-M(Δenz)-GFP, n = 23) (I). Compared with GFP-expressing cells: ****P < 0.0001. Bars: 5 µm; insets, 2 µm. **(J)** Statistical analysis of ER-LD-mito contacts from TEM images of COS7 cells overexpressing GFP, PISD-LD-GFP, or PISD-M-GFP under OA treatment. Left graph: percentage of mitochondrion-associated LDs in contact with the ER per cell. Each point represents an individual cell. Data are shown as the mean ± SEM (GFP, n = 24; PISD-LD-GFP, n = 28; PISD-M-GFP, n = 26). Right graph: percentage of mitochondrion-associated LD perimeter in contact with the ER. Each point represents a mitochondrion-associated LD. Data are shown as the mean ± SEM (GFP, n = 37; PISD-LD-GFP, n = 23; PISD-M-GFP, n = 29). N.S., not significant. **(K)** Relative *PISD-M* and *PISD-LD* transcription levels in NC, *siPISD-M*, and *siPISD-LD* cells. Quantitative data normalized by *ACTB* levels are presented as the mean ± SD (n = 3). **(L)** Confocal images of OA-treated COS7 cells with or without addition of Lyso-PE. Cells were stained with LipidTOX (LDs; magenta) and anti-TOMM20 antibody (mitochondria; green). Ctrl, control. Bars: 5 µm; insets, 2 µm. **(M)** In a GFP-Trap assay, Myc-PISD-LD is immunoprecipitated by PISD-M-GFP. The amount of immunoprecipitated protein increases with OA treatment. **(N and O)** Single focal plane images of OA-stimulated NC or *siPISD-LD* COS7 cells overexpressing PISD-M-GFP (green) and stained with LipidTOX (LDs; magenta) and anti-TOMM20 antibody (mitochondria; cyan) (N). Additionally, 3D

reconstructions and contact surfaces of the LipidTOX and TOMM20 channels (white) are shown (N). Graphs show contact surface areas, normalized by LD and mitochondrial surface areas. Each point represents an individual cell. Data are shown as the mean ± SEM (NC & GFP, *n* = 22; NC & PISD-M-GFP, *n* = 20; *siPISD-LD* & PISD-M-GFP, *n* = 21) (O). NC, negative control siRNA. ****P < 0.0001. Bars: 5 µm; insets, 2 µm. **(P)** In a GFP-Trap assay, the levels of Myc-PISD-M immunoprecipitated by PISD-LD (T49A/L54A)-GFP are dramatically reduced compared with those precipitated by WT PISD-LD-GFP. The asterisk indicates nonspecific bands. WT, wild type. **(Q)** Confocal images of OA-treated COS7 cells expressing NFAST and PISD-M-CFAST (top), CFAST and PISD-LD-NFAST (middle), and PISD-LD-NFAST and PISD-M-CFAST (bottom, green) alongside SNAP-MAVS(510–540). Cells were stained with LipidTOX (LDs; magenta) and SNAP-Cell 647-SiR (mitochondria; cyan). Arrows indicate the HMBR signal at LD-mito contact sites. The boxed area is enlarged in the inset. Bars: 5 µm; insets, 2 µm. **(R)** Confocal images of OA-stimulated NC and *siPISD-LD* COS7 cells transfected with PEX3-GFP or PEX3-PBD-GFP (green) and BFP-SKL (cyan) under OA stimulation. Cells were stained with LipidTOX (LDs; magenta). NC, negative control siRNA. PBD, PISD-LD–binding domain. Bars: 5 µm; insets, 1 µm. Source data are available for this figure: SourceData FS1.

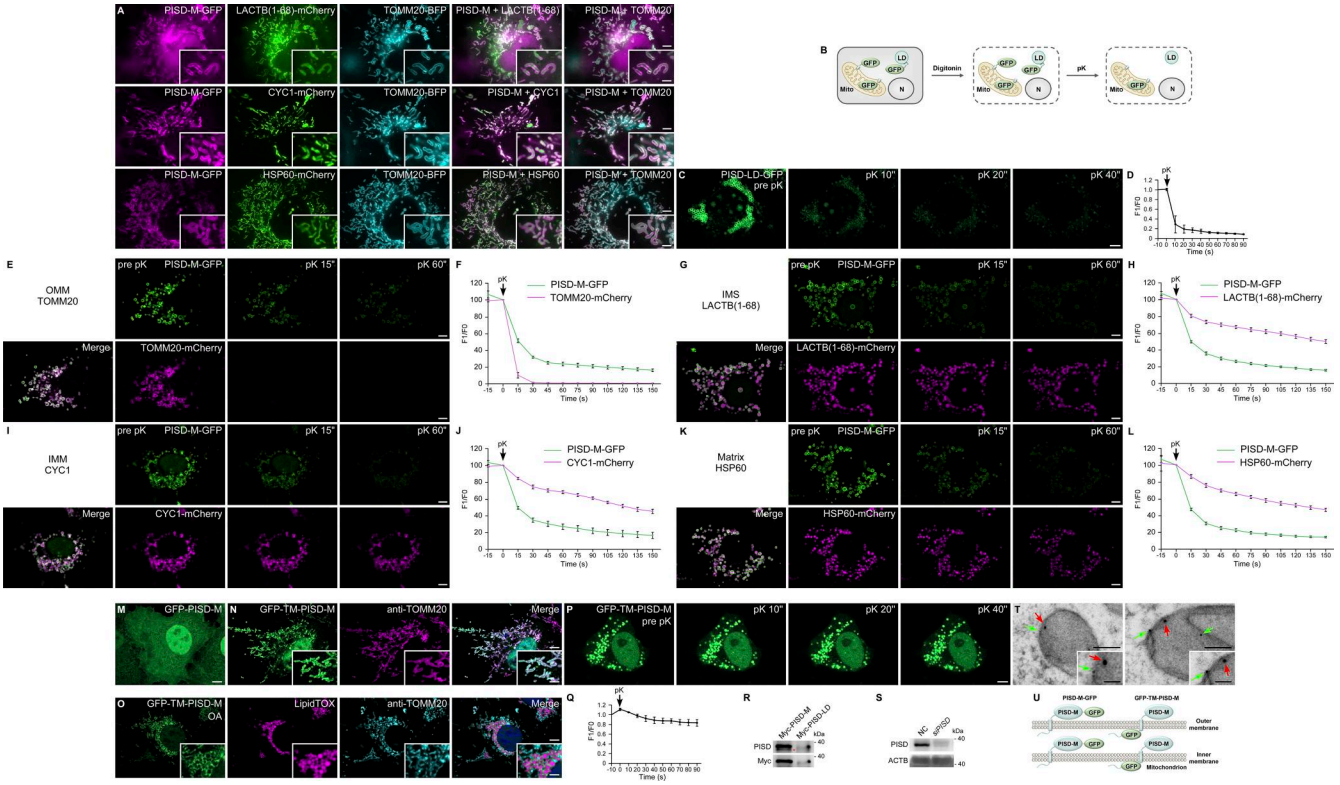

Figure S2. **Portion of PISD-M localizes to the outer membrane of mitochondria, related to Fig. 2. (A)** Super-resolution images of COS7 cells expressing PISD-M-GFP (magenta), TOMM20-BFP (OMM; cyan), and either CYC1-mCherry (IMM; green), LACTB(1–68)-mCherry (IMS; green), or HSP60-mCherry (mitochondrial matrix; green). Bars: 5 µm; insets, 2 µm. **(B)** Schematic illustration of the FPP assay. N, nucleus; LD, lipid droplet; Mito, mitochondrion; pK, proteinase K. **(C and D)** In FPP assays, time-lapse images show that PISD-LD-GFP signals immediately disappear upon pK addition in digitonin-permeabilized COS7 cells with OA treatment (C). Quantitative data are shown as the mean ± SEM (n = 3) (D). Bar: 5 µm. **(E and F)** In FPP assays, time-lapse images show that PISD-M-GFP signals immediately decrease, with some signals persisting, while TOMM20-mCherry signals completely disappear upon pK addition in digitonin-permeabilized COS7 cells treated with OA (E). Quantitative data are shown as the mean ± SEM (n = 3) (F). Bars: 5 µm. **(G and H)** In FPP assays, time-lapse images show that PISD-M-GFP signals immediately decrease, with some signals persisting, upon pK addition in digitonin-permeabilized COS7 cells treated with OA, while LACTB(1–68)-mCherry signals remain stable (G). Quantitative data are shown as the mean ± SEM (n = 3) (H). Bars: 5 µm. **(I and J)** In FPP assays, time-lapse images show that PISD-M-GFP signals immediately decrease, with some signals persisting, upon pK addition in digitonin-permeabilized COS7 cells treated with OA, while CYC1-mCherry signals remain stable (I). Quantitative data are shown as the mean ± SEM (n = 3) (J). Bars: 5 µm. **(K and L)** In FPP assays, time-lapse images show that PISD-M-GFP signals immediately decrease, with some signals persisting, upon pK addition in digitonin-permeabilized COS7 cells treated with OA, while HSP60-mCherry signals remain stable (K). Quantitative data are shown as the mean ± SEM (n = 3) (L). Bars: 5 µm. **(M)** Confocal images of COS7 cells expressing GFP-PISD-M (green). Bars: 5 µm. **(N)** Confocal images of COS7 cells expressing GFP-TM-PISD-M (green). Cells were stained with anti-TOMM20 antibody (mitochondria; magenta). Bars: 5 µm; insets, 2 µm. **(O)** Confocal images of COS7 cells expressing GFP-TM-PISD-M (green) with OA treatment. Cells were stained with anti-TOMM20 antibody (mitochondria; cyan) and LipidTOX (LDs; magenta). Bars: 5 µm; insets, 2 µm. **(P and Q)** In FPP assays, time-lapse images show that GFP-TM-PISD-M signals persist after pK addition in digitonin-permeabilized COS7 cells (P). Quantitative data are shown as the mean ± SEM (n = 3) (Q). Bars: 5 µm. **(R)** Immunoblotting shows that PISD antibody detects both Myc-PISD-M and Myc-PISD-LD. The asterisk indicates the endogenous PISD band. **(S)** Immunoblotting shows that the signal detected by PISD antibody is diminished in *siPISD*-treated cells. **(T)** Immuno-EM images show that PISD-M-Flag signals are detected on both OMM and IMM. PISD-HA/Flag stable cells were subjected to HPF fixation. Sections were immunolabeled with anti-Flag and anti-Mitofilin antibodies, followed by gold particle labeling. Green arrows indicate Flag signals (6 nm), while red arrows indicate Mitofilin signals (15 nm). Bars: 200 nm; insets: 50 nm. **(U)** Schematic showing the topology of PISD-M fusion proteins at the OMM and IMM. Immuno-EM, immuno-electron microscopy; HPF, high-pressure freezing. Source data are available for this figure: SourceData FS2.

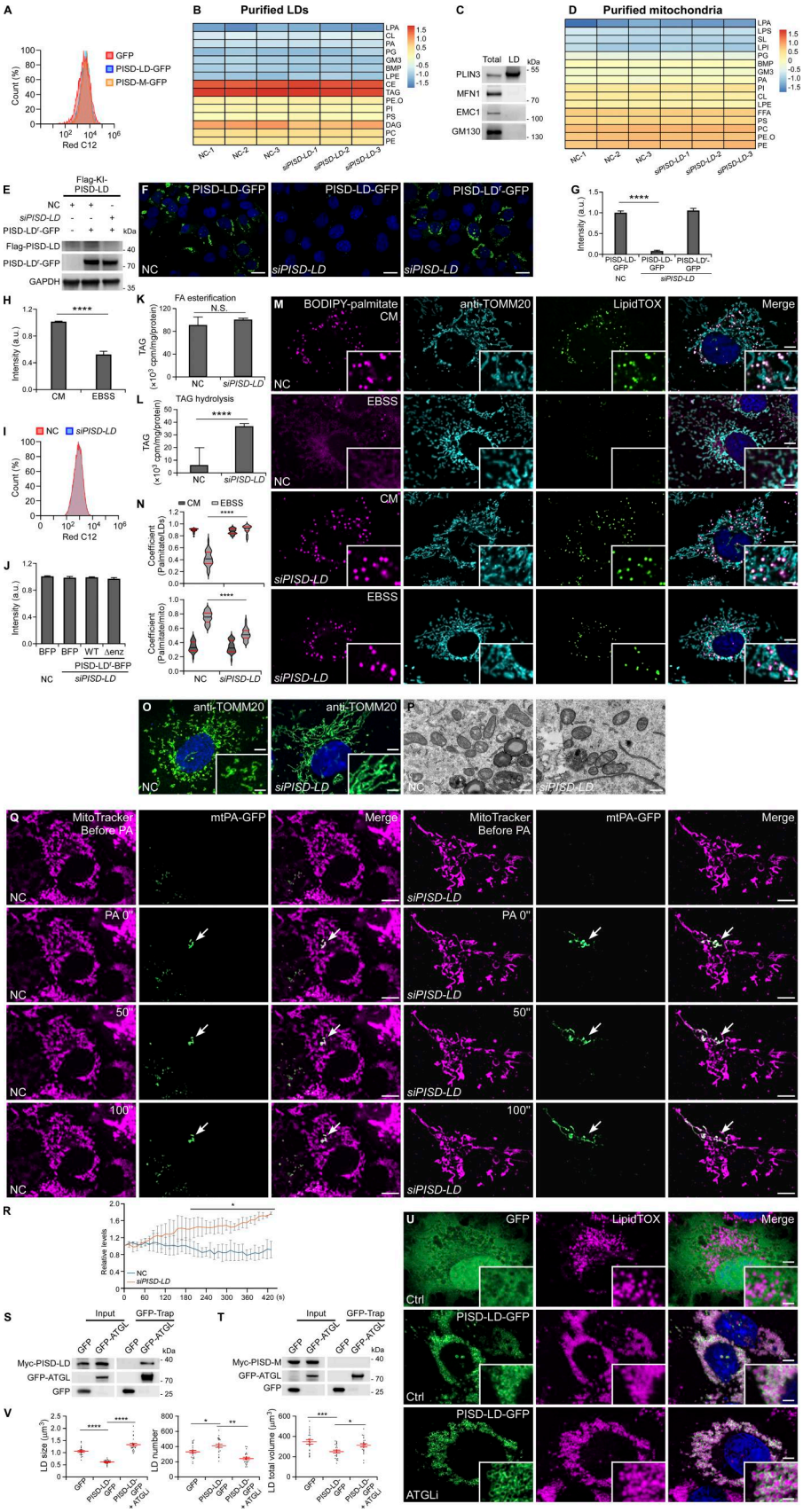

Figure S3. ***siPISD-LD* does not affect lipid composition of LDs and mitochondria, related to Figs. 3 and 4. (A)** Representative flow cytometry histograms for Red-C12 in COS7 cells overexpressing GFP (red), PISD-LD-GFP (blue), or PISD-M-GFP (orange). **(B)** Lipidomics analysis was conducted to identify changes in

lipid levels in LDs isolated from NC and *siPISD-LD* COS7 cells. The experiment was performed with three biological replicates (n = 3). Replicates 1–3 are indicated on the x axis. The heat map illustrates the levels of the 15 identified lipids. **(C)** Immunoblotting of the LD fraction isolated by flotation from COS7 cells. Blots were probed with anti-PLIN3 (LDs), anti-MFN1 (mitochondria), anti-EMC1 (ER), and anti-GM130 (Golgi) antibodies. **(D)** Lipidomics analysis was conducted to identify changes in lipid levels in mitochondria isolated from NC and *siPISD-LD* COS7 cells. The experiment was performed with three biological replicates (n = 3). Replicates 1–3 are indicated on the x axis. The heat map illustrates the levels of the 16 identified lipids. **(E)** Immunoblotting shows that the level of RNAi-resistant PISD-LD-GFP remains unaffected in *siPISD-LD*–treated Flag-KI-PISD-LD cells, while the level of endogenous Flag-PISD-LD is diminished upon *siPISD-LD*. Blots were probed with anti-Flag, anti-GFP, and anti-GAPDH antibodies. **(F and G)** Confocal images of NC and *siPISD-LD* COS7 cells overexpressing PISD-LD-GFP or RNAi-resistant PISD-LD-GFP (green) (F). The GFP fluorescence intensity is shown as the mean ± SEM (NC & PISD-LD-GFP, n = 30; *siPISD-LD* & PISD-LD-GFP, n = 30; *siPISD-LD* & PISD-LD^r-GFP, n = 30) (G). NC, negative control siRNA. ****P < 0.0001. Bars: 20 µm. **(H)** Fluorescence intensity of Red-C12 in COS7 cells under fed (CM) or starvation (EBSS 5 h) conditions (CM, n = 30; EBSS, n = 37). ****P < 0.0001. **(I)** Representative flow cytometry histograms for Red-C12 in NC (red) or *siPISD-LD* (blue) COS7 cells (after uptake for 2 h). **(J)** Fluorescence intensity of Red-C12 in NC and *siPISD-LD* COS7 cells overexpressing BFP, RNAi-resistant PISD-LD-BFP, or PISD-LD(Δenz)-BFP (after uptake for 2 h). Quantitative data are shown as the mean ± SEM (NC & BFP, n = 30; *siPISD-LD* & BFP, n = 31; *siPISD-LD* & PISD-LD^r-BFP; n = 26; *siPISD-LD* & PISD-LD(Δenz)^r-BFP, n = 27). **(K)** FA esterification in NC and *siPISD-LD* COS7 cells. Cells were incubated with medium containing 150 µM OA supplemented with 0.5 µCi/ml ^{3}H-labeled OA and then harvested at 0 and 6 h. Synthesized TAG was separated using thin-layer chromatography and collected from the membrane. The radioactivity of TAG, indicative of esterified FA, was quantified using a scintillation counter. Data are shown as the mean ± SEM (NC, n = 4; *siPISD-LD*, n = 4). N.S., not significant. **(L)** TAG hydrolysis in NC and *siPISD-LD* COS7 cells. Cells were treated for 16 h with 150 µM OA supplemented with 0.5 µCi/ml ^{3}H-labeled OA. The medium was then replaced with OA-free medium, and cells were collected at 0 and 6 h. The lipolysis rate was determined by measuring the decrease in radioactivity within the TAG fraction. Data are shown as the mean ± SEM (NC, n = 4; *siPISD-LD*, n = 4). ****P < 0.0001. **(M and N)** Confocal images of NC and *siPISD-LD* COS7 cells loaded with BODIPY-palmitate (magenta) and stained with LipidTOX (LDs; green) and anti-TOMM20 antibody (mitochondria; cyan) under fed (CM) or starvation (EBSS) conditions (M). Overlap coefficients of BODIPY-palmitate with LDs or mitochondria are shown as violin plots with the black line indicating the median and the red lines indicating the interquartile range (NC in CM, n = 29; NC in EBSS, n = 30; *siPISD-LD* in CM, n = 30; *siPISD-LD* in EBSS, n = 30) (N). NC, negative control siRNA. ****P < 0.0001. Bars: 5 µm; insets, 2 µm. **(O)** Confocal images of OA-stimulated NC or *siPISD-LD* COS7 cells stained with anti-TOMM20 antibody (green). NC, negative control siRNA. Bars: 5 µm; insets, 2 µm. **(P)** TEM images of NC or *siPISD-LD* COS7 cells with OA stimulation. NC, negative control siRNA. Bars: 500 nm. **(Q and R)** Time-lapse images of NC or *siPISD-LD* COS7 cells transfected with mtPA-GFP (green) and stained with MitoTracker (mitochondria; magenta). Cells were stimulated with a 405-nm laser. NC, negative control siRNA; PA, photoactivatable. Arrows indicate photoactivated mtPA-GFP on mitochondria (Q). Quantification of the area of mtPA-GFP signal is shown as the mean ± SEM (n = 3) (R). *P < 0.05. Bars, 5 µm. **(S and T)** In GFP-Trap assays, Myc-PISD-LD (S), but not Myc-PISD-M (T), is immunoprecipitated by GFP-ATGL. **(U and V)** 3D projection images of OA-stimulated COS7 cells overexpressing GFP, PISD-LD-GFP (green) with or without ATGLi treatment. Cells were stained with LipidTOX (LDs; magenta) (U). LD sizes, numbers, and total volumes are shown as the mean ± SEM (GFP, n = 22; PISD-LD-GFP, n = 22; PISD-LD-GFP + ATGLi, n = 24) (V). ATGLi, Atglistatin. *P < 0.05; **P < 0.01; ***P < 0.001; ****P < 0.0001. Bars: 5 µm; insets, 2 µm. CM, complete medium. Source data are available for this figure: SourceData FS3.

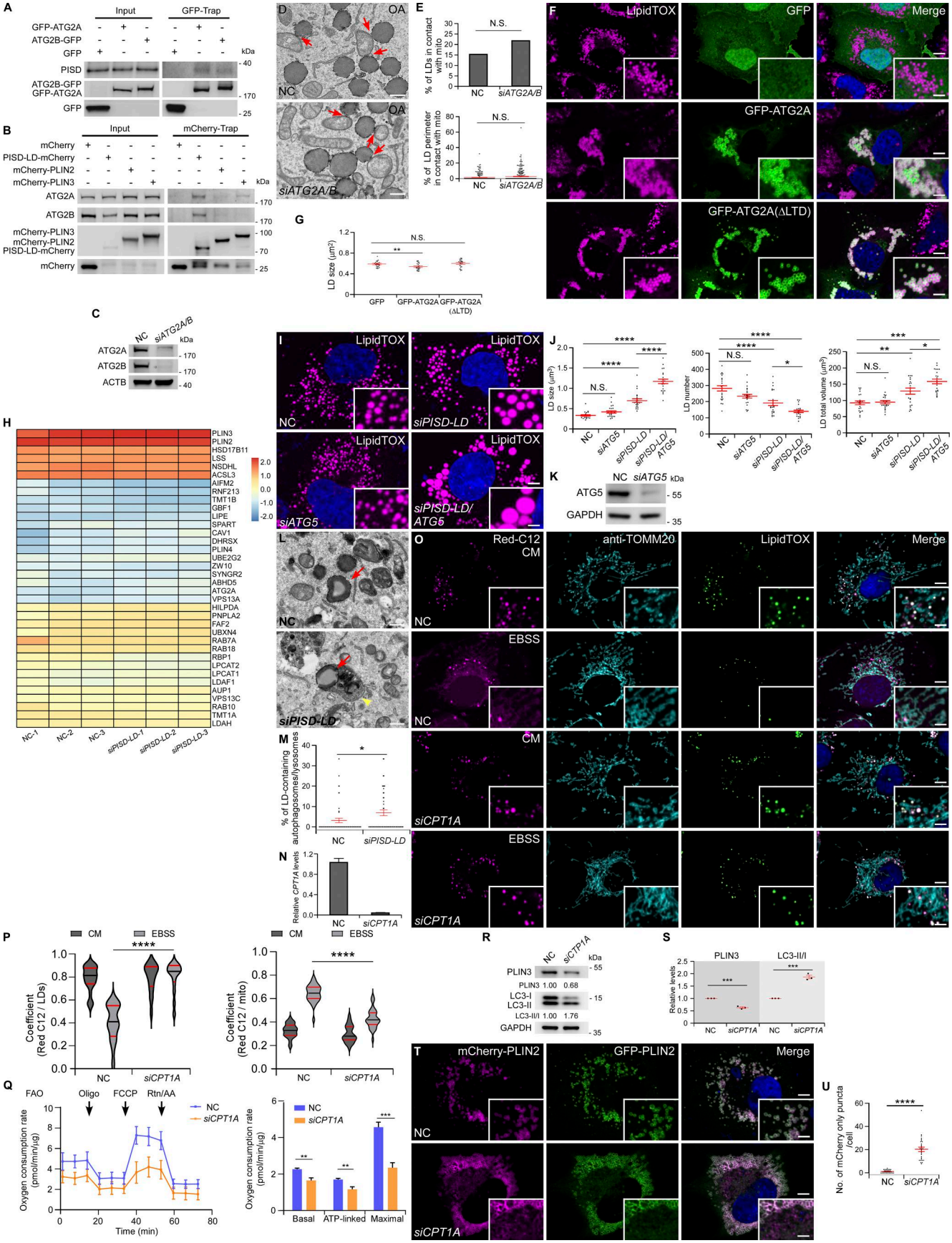

Figure S4. **PISDs recruit ATG2A/B to facilitate FA transport, related to Fig. 5. (A)** In a GFP-Trap assay, endogenous PISD is immunoprecipitated by GFP-ATG2A and ATG2B-GFP. **(B)** In a mCherry-Trap assay, endogenous ATG2A and ATG2B are immunoprecipitated by PISD-LD-mCherry but not mCherry-PLIN2 or mCherry-PLIN3. **(C)** Immunoblotting with anti-ATG2A, anti-ATG2B, and anti-ACTB antibodies shows the KD efficiency of *siATG2A/B*. NC, negative control siRNA. **(D and E)** TEM images of LD-mito contacts in OA-treated COS7 cells with KD of ATG2A and ATG2B (*siATG2A/B*) (D). Top graph: percentage of LDs in contact with mitochondria per cell, shown as the mean ± SEM (NC, *n* = 259 LDs from 15 cells; *siATG2A/B*, *n* = 297 LDs from 15 cells). Bottom graph: percentage of LD perimeter in contact with mitochondria per LD, shown as the mean ± SEM (NC, *n* = 259 LDs from 15 cells; *siATG2A/B*, *n* = 297 LDs from 15 cells) (E). NC, negative control siRNA. Red arrows indicate LD-mito contacts. N.S., not significant. Bars: 500 nm. **(F and G)** Confocal images of COS7 cells overexpressing GFP, GFP-ATG2A, or GFP-ATG2A(ΔLTD) (green) under OA stimulation. LDs were stained with LipidTOX (magenta) (F). LD sizes are shown as the mean ± SEM (GFP, *n* = 25; GFP-ATG2A, *n* = 25; GFP-ATG2A(ΔLTD), *n* = 25) (G). **P < 0.01; N.S., not significant. Bars: 5 µm; insets, 2 µm. **(H)** Levels of LD-localized proteins in NC or *siPISD-LD* COS7 cells were assessed using proteomics analysis. Replicates 1–3 are indicated on the x axis. The heat map illustrates the levels of the 36 identified proteins. **(I and J)** 3D projection images of NC, *siPISD-LD*, *siATG5*, or *siPISD-LD/ATG5* COS7 cells under OA stimulation. LDs were stained with LipidTOX (magenta) (I). LD sizes, numbers, and total volumes are shown as the mean ± SEM (NC, *n* = 22; *siATG5*, *n* = 23; *siPISD-LD*, *n* = 22; *siPISD-LD/ATG5*, *n* = 22) (J). NC, negative control siRNA. *P < 0.05; **P < 0.01; ***P < 0.001; ****P < 0.0001; N.S., not significant. Bars: 5 µm; insets, 2 µm. **(K)** Immunoblotting with anti-ATG5 and anti-GAPDH antibodies shows the KD efficiency of *siATG5*. NC, negative control siRNA. **(L and M)** TEM images show that LDs in autophagosomes/lysosomes are detected in OA-treated PISD-LD–deficient cells (L). Percentage of LD-containing autophagosomes/lysosomes, shown as the mean ± SEM (NC, *n* = 49; *siPISD-LD*, *n* = 49) (M). NC, negative control siRNA. Red arrows indicate LDs. The yellow arrowhead indicates an autolysosome/lysosome. *P < 0.05. Bars: 500 nm. **(N)** Relative *CPT1A* transcription levels in NC and *siCPT1A* cells. Quantitative data normalized by *ACTB* levels are presented as the mean ± SD (*n* = 3). NC, negative control siRNA. **(O and P)** Confocal images of NC and *siCPT1A* COS7 cells loaded with Red-C12 and stained with LipidTOX (LDs; green) and anti-TOMM20 antibody (mitochondria; cyan) under fed (CM) or starved (EBSS) conditions (O). Overlap coefficients of Red-C12 with LDs or mitochondria are shown as violin plots with the solid black line indicating the median and the red dotted lines indicating the interquartile range (NC in CM, *n* = 30; NC in EBSS, *n* = 32; si*CPT1A* in CM, *n* = 30; si*CPT1A* in EBSS, *n* = 31) (P). ****P < 0.0001. Bars: 5 µm; insets, 2 µm. **(Q)** Seahorse FAO assays show oxidation of endogenous FAs in NC cells (blue) and *siCPT1A* cells (orange). Quantitative data of basal OCR, ATP-linked OCR, and maximal OCR in mitochondria are shown as means ± SD (*n* = 3). NC, negative control siRNA; Oligo, oligomycin; FCCP, carbonyl cyanide-p-trifluoromethoxyphenylhydrazone; Rtn, rotenone; AA, antimycin A. **P < 0.01; ***P < 0.001. **(R and S)** Immunoblotting of NC and *siCPT1A* cells. Blots were probed with anti-PLIN3, anti-LC3B, and anti-GAPDH antibodies (R). Quantifications of PLIN3 levels (normalized by GAPDH levels) and LC3-II/I ratio are shown as the mean ± SEM (*n* = 3) (S). NC, negative control siRNA. ***P < 0.001. **(T and U)** Confocal images of OA-stimulated NC and *siCPT1A* cells transfected with mCherry-GFP-PLIN2 (T). Numbers of mCherry-only puncta per cell are shown as the mean ± SEM (NC, *n* = 29; *siCPT1A*, *n* = 28) (U). NC, negative control siRNA. ****P < 0.0001. Bars: 5 µm; insets, 2 µm. Source data are available for this figure: SourceData FS4.

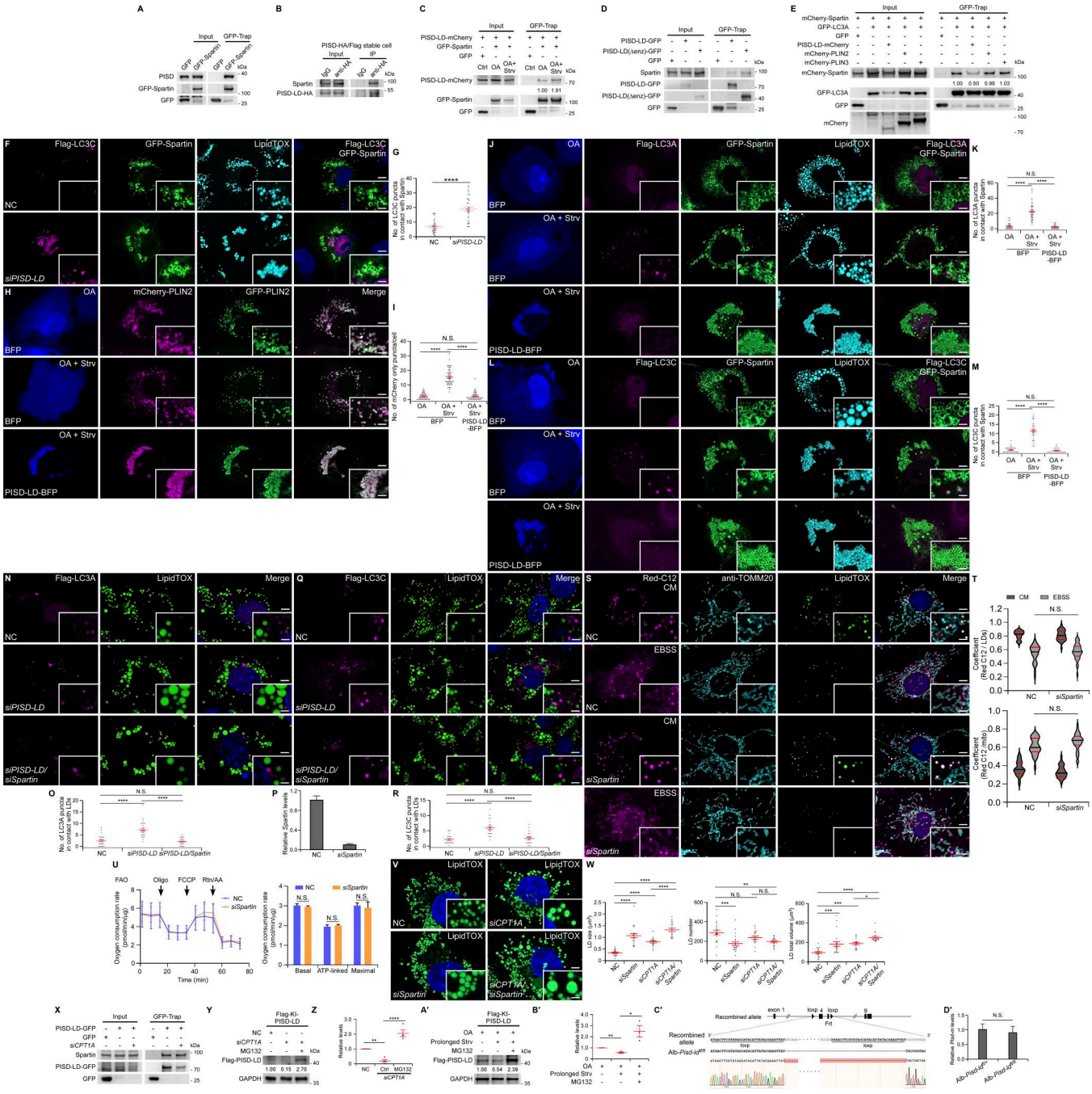

Figure S5. **Lipophagy induced by PISD-LD deficiency is mediated by Spartin, related to Figs. 6 and 7. (A)** In a GFP-Trap assay, endogenous PISD is immunoprecipitated by GFP-Spartin. **(B)** Co-IP analysis of the interaction between PISD-LD-HA and endogenous Spartin in PISD-HA/Flag stable cells. Immunoprecipitation was performed using a specific antibody against HA or a control IgG. **(C)** In a GFP-Trap assay, PISD-LD-mCherry is immunoprecipitated by GFP-Spartin. The amount of immunoprecipitated protein increases under starvation (Strv) conditions. Quantifications of PISD-LD-mCherry levels (normalized by GFP-Spartin levels) are shown. **(D)** In a GFP-Trap assay, the levels of endogenous Spartin immunoprecipitated by PISD-LD(Δenz)-GFP are comparable to those of WT PISD-LD-GFP. **(E)** In GFP-Trap assays, levels of mCherry-Spartin immunoprecipitated by GFP-LC3A are reduced by overexpression of PISD-LD-mCherry but not mCherry-PLIN2 and mCherry-PLIN3. Quantifications of mCherry-Spartin levels (normalized by GFP-LC3A levels) are shown. **(F and G)** Confocal images of NC or *siPISD-LD* COS7 cells transfected with Flag-LC3C (magenta) and GFP-Spartin (green) under OA stimulation. LDs were stained with LipidTOX (LDs; cyan) (F). Numbers of LC3C puncta in contact with Spartin are shown as the mean ± SEM (NC, *n* = 35; *siPISD-LD*, *n* = 35) (G). NC, negative control siRNA. ****P < 0.0001. Bars: 5 µm; insets, 2 µm. **(H and I)** Confocal images of COS7 cells overexpressing BFP or PISD-LD-BFP (blue) and transfected with mCherry-GFP-PLIN2. Cells were exposed to OA stimulation without or with starvation (Strv) treatment (H). The numbers of mCherry-only puncta per cell are shown as the mean ± SEM (OA & BFP, *n* = 49; OA + Strv & BFP, *n* = 48; OA + Strv & PISD-LD-BFP, *n* = 51) (I). NC, negative control siRNA. ****P < 0.0001; N.S., not significant. Bars: 5 µm; insets, 2 µm. **(J and K)** Confocal images of COS7 cells overexpressing BFP or PISD-LD-BFP (blue) and transfected with Flag-LC3A (magenta) and GFP-Spartin (green). Cells were exposed to OA stimulation without or with starvation (Strv) treatment. LDs were stained with LipidTOX (LDs; cyan) (J). Numbers of LC3A puncta in contact with Spartin are shown as the mean ± SEM (OA & BFP, *n* = 37; OA + Strv & BFP, *n* = 47; OA + Strv & PISD-LD-BFP, *n* = 39) (K). NC, negative control siRNA. N.S., not significant. ****P < 0.0001. Bars: 5 µm; insets, 2 µm. **(L and M)** Confocal images of COS7 cells overexpressing

BFP or PISD-LD-BFP (blue) and transfected with Flag-LC3C (magenta) and GFP-Spartin (green). Cells were exposed to OA stimulation without or with starvation (Strv) treatment. LDs were stained with LipidTOX (LDs; cyan) (L). Numbers of LC3C puncta in contact with Spartin are shown as the mean ± SEM (OA & BFP, *n* = 38; OA + Strv & BFP, *n* = 34; OA + Strv & PISD-LD-BFP, *n* = 32) (M). NC, negative control siRNA. N.S., not significant. ****P < 0.0001. Bars: 5 µm; insets, 2 µm. **(N and O)** Confocal images of NC, *siPISD-LD*, or *siPISD-LD/Spartin* COS7 cells transfected with Flag-LC3A (magenta) under OA stimulation. Cells were stained with LipidTOX (LDs; green) (N). Numbers of LC3A puncta in contact with LDs are shown as the mean ± SEM (NC, *n* = 31; *siPISD-LD*, *n* = 28; *siPISD-LD/Spartin*, *n* = 27) (O). NC, negative control siRNA. ****P < 0.0001; N.S., not significant. Bars: 5 µm; insets, 2 µm. **(P)** Relative *Spartin* transcription levels show the KD efficiency of *siSpartin*. Quantitative data normalized by *ACTB* levels are presented as the mean ± SEM (*n* = 3). **(Q and R)** Confocal images of NC, *siPISD-LD*, or *siPISD-LD/Spartin* COS7 cells transfected with Flag-LC3C (magenta) under OA stimulation. Cells were stained with LipidTOX (LDs; green) (Q). Numbers of LC3C puncta in contact with LDs are shown as the mean ± SEM (NC, *n* = 22; *siPISD-LD*, *n* = 23; *siPISD-LD/Spartin*, *n* = 21) (R). NC, negative control siRNA. ****P < 0.0001; N.S., not significant. Bars: 5 µm; insets, 2 µm. **(S and T)** Confocal images of NC and *siSpartin* COS7 cells loaded with Red-C12 (magenta) and stained with LipidTOX (LDs; green) and anti-TOMM20 antibody (mitochondria; cyan) under fed (CM) or starvation (EBSS) conditions (S). Overlap coefficients of Red-C12 with LDs or mitochondria are shown as violin plots with the black line indicating the median and red lines indicating the interquartile range (NC in CM, *n* = 30; NC in EBSS, *n* = 33; *siSpartin* in CM, *n* = 35; *siSpartin* in EBSS, *n* = 34) (T). NC, negative control siRNA. N.S., not significant. Bars: 5 µm; insets, 2 µm. **(U)** Seahorse FAO assays show oxidation of endogenous FAs in NC cells (blue) and *siSpartin* cells (orange). Quantitative data of basal OCR, ATP-linked OCR, and maximal OCR in mitochondria are shown as means ± SD (*n* = 5). NC, negative control siRNA; Oligo, oligomycin; FCCP, carbonyl cyanide-p-trifluoromethoxyphenylhydrazone; Rtn, rotenone; AA, antimycin A. N.S., not significant. **(V and W)** 3D projection images of NC, *siSpartin*, *siCPT1A*, or *siSpartin/CPT1A* COS7 cells under OA stimulation. LDs were stained with LipidTOX (green) (V). LD sizes, numbers, and total volumes are shown as the mean ± SEM (NC, *n* = 21; *siSpartin*, *n* = 21; *siCPT1A*, *n* = 17; *siSpartin/CPT1A*, *n* = 18) (W). NC, negative control siRNA. *P < 0.05; **P < 0.01; ***P < 0.001; ****P < 0.0001; N.S., not significant. Bars: 5 µm; insets, 2 µm. **(X)** In GFP-Trap assays, levels of endogenous Spartin immunoprecipitated by PISD-LD-GFP are increased in *siCPT1A* cells compared with NC cells. NC, negative control siRNA. The asterisk indicates nonspecific bands. **(Y and Z)** Immunoblotting of NC- and *siCPT1A*-treated Flag-KI-PISD-LD cells with or without MG132 treatment under OA stimulation. Blots were probed with anti-Flag and anti-GAPDH antibodies. NC, negative control siRNA (Y). Quantifications of Flag levels (normalized by GAPDH levels) are shown as the mean ± SEM (*n* = 4) (Z). **P < 0.01; ****P < 0.0001. **(A′ and B′)** Immunoblotting of Flag-KI-PISD-LD cells with OA, OA plus starvation for 24 h (prolonged Strv), and OA plus starvation for 24 h with MG132 treatment. Blots were probed with anti-Flag and anti-GAPDH antibodies (A′). Quantifications of Flag levels (normalized by GAPDH levels) are shown as the mean ± SEM (*n* = 3) (B′). *P <0.05; **P < 0.001. **(C′)** Sequencing of genomic DNA extracted from livers of Alb-*Pisd-ld*$^{fl/fl}$ mice. **(D′)** Relative *Pisd-m* mRNA levels from livers of Alb-*Pisd-ld*$^{fl/+}$ and Alb-*Pisd-ld*$^{fl/fl}$ mice. *Pisd-m* mRNA levels were normalized with *Actb* levels (*n* = 3) and are shown as the mean ± SD. N.S., not significant. CM, complete medium. Source data are available for this figure: SourceData FS5.

Video 1. **Reconstruction, using FIB-SEM, of MCSs between LDs and mitochondria in GFP-overexpressing cells.** Segmentation and reconstruction from raw serial section electron microscopy volumes are shown. Mitochondrial membranes are colored green, LD membranes are colored magenta, and contact sites are colored blue.

Video 2. **Reconstruction, using FIB-SEM, of MCSs between LDs and mitochondria in PISD-LD-GFP–overexpressing cells.** Segmentation and reconstruction from raw serial section electron microscopy volumes are shown. Mitochondrial membranes are colored green, LD membranes are colored magenta, and contact sites are colored blue.